

AD-A278 885



SRL 04-F-1994

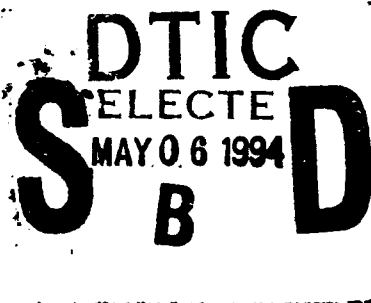


**ADVANCED INDUCTION ACCELERATOR DESIGNS FOR
GROUND BASED AND SPACE BASED FELs**

Principal Investigator:

Dr. Daniel Birx

SCIENCE RESEARCH LABORATORY, INC.
15 Ward Street
Somerville, MA 02143



April 30, 1994

PHASE II FINAL TECHNICAL REPORT

Period for May 1, 1990 to April 30, 1994

Contract Number N00014-90-C-0099

APPROVED FOR PUBLIC RELEASE; DISTRIBUTION UNLIMITED

94-13596

Prepared for
OFFICE OF NAVAL RESEARCH
800 North Quincy Street
Arlington, VA 22217-5000

"The views and conclusions contained in this document are those of the authors and should not be interpreted as representing the official policies, either expressed or implied, of the Ballistic Missile Defense Organization or the U.S. Government."

DTIC QUALITY INSPECTED 1

94 5 05 080

TABLE OF CONTENTS

<u>Section</u>	<u>Page</u>
EXECUTIVE SUMMARY	1
1 OVERVIEW OF THE LONG TERM EXPERIMENTAL PROGRAM	1-1
1.1 The MIT ECH Development Program	1-3
2 THE SNOMAD-IV 0.5 MeV INJECTOR	2-1
3 SNOMAD-IVB, 1.0 MeV INDUCTION ACCELERATOR MODULE	3-1

Accession For	
NTIS GRA&I	<input checked="" type="checkbox"/>
DTIC TAB	<input type="checkbox"/>
Unannounced	<input type="checkbox"/>
Justification	
By _____	
Distribution/ _____	
Availability Codes	
Dist	Avail and/or Special
A-1	

LIST OF ILLUSTRATIONS

<u>Figure</u>		<u>Page</u>
1.1	SNOMAD-II Installation at MIT	1-2
1.2	An Induction Linac Driven Free Electron Laser for ECH Heating	1-6
2.1	SNOMAD-IV 0.5 MeV Electron injector module	2-2
2.2	Electrical Schematic of SNOMAD-IV solid-state driver	2-4
2.3	SNOMAD-IV accelerator cell	2-7
2.4	Coupling coefficient, K, versus ferrite core inner radius for beam currents from 1 to 5 kA.	2-12
2.5	Required ferrite core volume, $\nu_{ferrite}$, versus accelerating gap voltage for $r_i = 0.015, 0.10, 0.15, 0.20, 0.24, 0.30$ meters.	2-13
2.6	Assembly drawing SNOMAD-IV input commutator arms, first compression stage and step-up transformer.	2-14
2.7	Assembly drawing of SNOMAD-IV second compression stage, PFN and output stage.	2-16
2.8	Drawing of SNOMAD-IV 0.5 MeV injector accelerator cell assembly.	2-20
2.9	Preliminary assembly drawing of cathode extraction optics and vacuum pumping port.	2-22
2.10	SNOMAD-IV Enclosure, elevation	2-24
2.11	SNOMAD-IV Enclosure, plan view	2-25
2.12	Photograph of SNOMAD-IV injector and pulse power supply	2-26
2.13	The 500 kV induction accelerator and x-ray target (inside the blue lead box) assembly in the experiment vault.	2-27
2.14	Voltage measurement using capacitive divider looking at the cathode stalk.	2-28
2.15	Current measured 76 cm downstream, by integrating the dB/dt signal from a single turn pickup loop.	2-29

LIST OF ILLUSTRATIONS CONTINUED

<u>Figure</u>		<u>Page</u>
3.1	Photograph of 1.5 MeV Accelerator Installation at SRL	3-2
3.2	SNOMAD-IVB Driver	3-3
3.3	SNOMAD-IVB Input Section	3-7
3.4	SNOMAD-IVB Driver Output Section	3-8
3.5	SNOMAD-IVB Driver	3-9
3.6	SNOMAD-IVB Accelerator Cell	3-10
3.7	SNOMAD-IVB Accelerator Cells	3-11
3.8	SNOMAD-IVB Main Body Enclosure	3-13
3.9	SNOMAD-IVB Base Plate Enclosure	3-14
3.10	SNOMAD-IVB Lid Enclosure	3-15
3.11	Photograph of Completed SNOMAD-IVB, 1.0 MeV Accelerator Module	3-16
3.12	Photograph of SNOMAD-IVB 1.0 MeV Accelerator Module in Box with Lid Removed	3-17
3.13	Photograph of SNOMAD-IVB; 1.0 MeV accelerator module before installation in box	3-18
3.14	SNOMAD-IVB Accelerator Potential – Input Level = 800 Volts	3-19
3.15	SNOMAD-IVB Accelerator Potential – Input Level = 950 Volts	3-20
3.16	Charge Module	3-22
3.17	SRL-2650B Control Module Logic Circuit	3-25
3.18	Control Module	3-26

EXECUTIVE SUMMARY

The primary goal of this program was to improve the performance of induction accelerators with particular regards to their being used to drive Free Electron Lasers (FELs). It is hoped that FELs operating at visible wavelengths might someday be used to beam power from earth to extraterrestrial locations. One application of this technology might be strategic theater defense, but this power source might be used to propel vehicles or supplement solar energized systems. Our path toward achieving this goal was directed first toward optimization of the nonlinear magnetic material used in induction accelerator construction and secondly at the overall design in terms of cost, size and efficiency.

We began this research effort with an in depth study into the properties of various nonlinear magnetic materials (e.g. various ferrite compositions, Metglas (an amorphous tape composed of steel and glass), and more conventional magnetic materials such as 50/50 Ni-Fe tapes). With the data on nonlinear magnetic materials, so important to the optimization of efficiency, in hand, we envisioned a new induction accelerator design where all of the components were packaged together in one container. This induction accelerator module would combine an all-solid-state, nonlinear magnetic driver and the induction accelerator cells all in one convenient package. Each accelerator module (denoted SNOMAD-IVB) would produce 1.0 MeV of acceleration with the exception of the SNOMAD-IV injector module which would produce 0.5 MeV of acceleration for an electron beam current up to 1000 amperes. An arbitrary number of modules could be stacked end to end producing any desired electron beam energy.

Following the initial basic research phase of this program we began construction on the 0.5 MeV SNOMAD-IV injector. The SNOMAD-IV was extensively tested for about 1 year before the design and construction of the first SNOMAD-IVB, 1.0 MeV accelerator modules commenced. When the SNOMAD-IVB accelerator module was completed it was installed in a shielded pit which was then only occupied by the lonely SNOMAD-IV injector. The completed 1.5 MeV accelerator has since been operated on a regular basis and is used as an electron source for a variety of experiments.

In the remainder of this report we will describe the SNOMAD-IV 0.5 MeV injector module, and the SNOMAD-IVB 1.0 MeV accelerator module.

SECTION 1

OVERVIEW OF THE LONG TERM EXPERIMENTAL PROGRAM

In this section we discuss the long term objectives of this program as well as providing a quick review of the ongoing experimental activity. SRL has been working closely with the MIT Plasma Fusion Center throughout this effort. This relationship promises to provide MIT with an FEL facility that would be used to demonstrate the feasibility of ECH heating in advanced Tokamaks. In return SRL receives valuable operating data which directly applies to the design of a visible wavelength FEL.

Under this agreement, MIT would supply a shielded location for the accelerator as well as graduate students who would operate and support the installation. The graduate students would complete their experimental training by conducting research projects on the accelerator that could be applied directly to their doctoral theses. SRL would supply the accelerator and possibly the FEL.

This collaborative project began with the installation of the SNOMAD-II accelerator (Fig. 1.1) at MIT. SNOMAD-II was an all-solid-state, 1.0 MeV, induction accelerator which served as the breadboard for SNOMAD-IV. SNOMAD-II is still operational at MIT and is presently being used as the electron source for a successful 17 GHz CARM experiment. A CARM (Cyclotron Auto-Resonant Maser) is very similar to an FEL but the presence of an axial magnetic field greatly augments the electron-photon interaction and provides greatly enhanced gain per unit length. SNOMAD-II has been a valuable research tool and operates on a daily basis, but in order to perform a full scale FEL experiment that would demonstrate high average power outputs at wavelengths nearer those of the visible required a bigger accelerator.

SRL and MIT planned a new installation in the same building which would address DoE fusion applications as well as providing SRL with a proof-of-principle experiment that would be

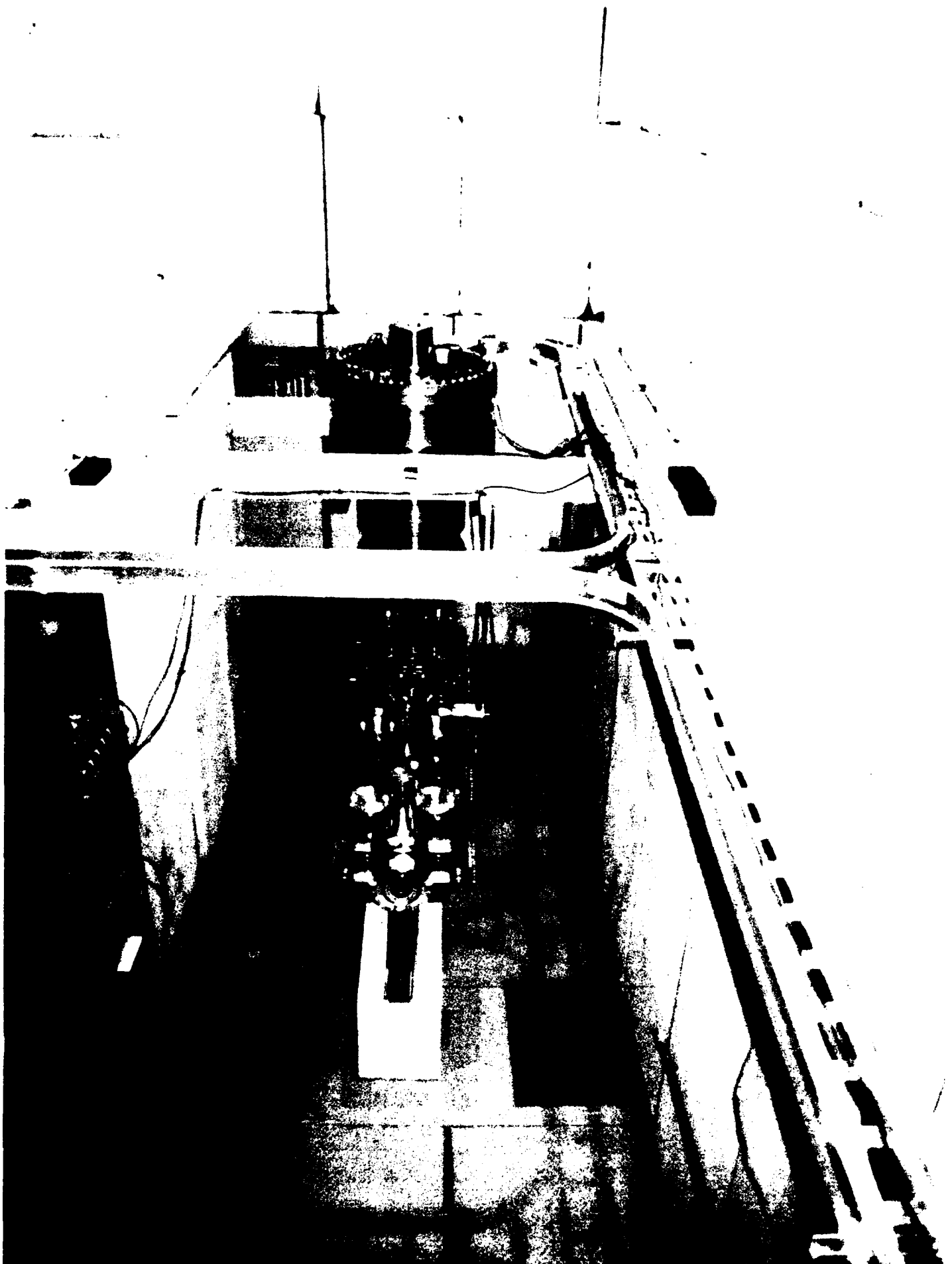


Figure 1.1: SNOMAD-II Installation at MIT

directly applicable to a high power, optical FEL. We continue with a description of this plan.

1.1 The MIT ECH Development Program

Among the various auxiliary heating methods for tokamak plasmas, electron cyclotron heating (ECH) offers many advantages and is currently favored as the primary heating technique for future tokamak devices (CIT and ITER). These advantages include: 1) controlled localization of power deposition through choice of radiation frequency; 2) ease of access through vacuum vessel ports; 3) precise control of launching; 4) minimal interaction with plasma edge and vacuum vessel; 5) potential to control disruptions; 6) ability to provide cw current drive. The Department of Energy has been engaged in the development of high power, high frequency microwave devices for several years. Research in gyrotrons, FELs, and most recently cyclotron auto resonance masers (CARMs) is presently being pursued by the DOE ECH Technology Development Program. A recent Panel XXI report⁽¹⁾ presented to the Magnetic Fusion Advisory Committee (MFAC) recommends continued DOE support for the development of high power ECH sources.

Next generation Tokamaks will operate with a central magnetic field of up to 10 Tesla, requiring 280 GHz for fundamental heating and 560 GHz for second harmonic. A total of 10 MW of auxiliary heating for several seconds will be required. The ideal ECH source will be capable of generating this power in 0.5-5.0 MW modules, and be frequency tunable over a sufficient range to provide profile heating control and operation over a range of tokamak magnetic fields. A recent ECH technology review report⁽²⁾ recommends that the source be step tunable by 30% and dynamically tunable by 5-10% on a time scale of tens of milliseconds. Tunable FELs and CARMs are being developed to satisfy there performance requirements. The CARM is an attractive alternative to the FEL because of its lower e-beam energy requirement and overall simplicity of design. However, little experimental data is available on the performance of CARMs in this frequency and power range.

The success of ECH will require reliable and economical radiation sources at the appropriate

frequencies and power levels. High power FELs and CARMs suitable for ECH applications rely on accelerator facilities to provide high energy (1-10 MeV), high average power (2-10 MW), electron beams. Consequently, the development of economical FELs and CARMs for ECH will require low cost, high efficiency accelerator technology. The induction linac is unique in its ability to accelerate high peak currents (> 1000 amps) to several MeV with a high repetition rate (> 1000 Hz); delivering electron beams with multi-megawatt power levels to an FEL wiggler or CARM resonator. However, the complexity and cost of induction linac facilities has, thus far, restricted the development of millimeter wave sources based on this technology to the national laboratories. Recent advances by Science Research Laboratory (SRL) in the design and development of SCR commutated magnetic pulse compression power systems and compact accelerator cells has significantly reduced the cost and improved the reliability of high repetition rate induction linacs.

This report has described the development of a high repetition rate induction linear accelerator optimized for driving ECH sources. The objective of the research program has been to develop a low cost and highly reliable accelerator suitable for driving high frequency (> 250 GHz), high average power (> 1 MW) radiation sources. In the future these advanced induction accelerator modules will be installed in the high power microwave laboratory at the MIT Plasma Fusion Center where it will be available for millimeter wave source development.

The induction linac offers the promise of generating very high average power electron beams of sufficient brightness to drive millimeter wave radiation sources. The present generation of induction linacs have been operated with peak currents of 1-10 kA, 50 nsec pulse lengths and beam energies of up to 50 MeV. These accelerators are powered by thyatron commutated magnetic pulse compression circuits, and are designed to operate at up to 5 kHz pulse repetition rate. Continuous pulse rates of 10 pps have been demonstrated and initial demonstration experiments of high repetition operation are planned for 1990.⁽³⁾ Reliable high repetition rate operation will be required to satisfy the demands of ECH sources.

The development of a reliable high repetition rate thyatron pulse compression driver poses a difficult challenge and constitutes a significant fraction of the cost and size of present generation induction linear accelerator.

All-solid-state SCR commutated magnetic pulse compression circuits offer significantly higher repetition rate operation, improved reliability and a significant reduction in cost and size over thyatron-based designs. High repetition rate operation of an accelerator has recently been demonstrated using this technology.⁽⁴⁾

A block diagram for the future planned accelerator installation at MIT is provided in Fig. 1.2. Operating costs and the fabrication of both the low power, 280 GHz local oscillator and the FEL will be the responsibility of DoE/MIT.

References

- 1) J. Leiss, D. Baldwin, L. Berry, N. Luhmann, T. Marshall, D. Montgomery, R. Parker, R. Prater, P. Sprangle, K. Thomassen, J. Watson, H. Weitzner, Electron Cyclotron Heating Requirements for the Fusion Program, Panel XXI Report to Magnetic Fusion Advisory Committee, December 6, 1988.
- 2) T. Marshall, J. Lebacqz, T. Godlove, Electron Cyclotron Heating Technology Review, U.S. DoE, Office of Energy Research, Office of Fusion Energy, Division of Development and Technology, May 1987.
- 3) K. Thomassen, Lawrence Livermore National Laboratory, Livermore, CA, LLL-PROP-00202, 1986.
- 4) R.E. Klinkowstein, D. Bix, A Low Cost Induction Linac for High Power Electron Cyclotron Heating Millimeter Wave Sources, Bul. Am. Phys. Soc., 34, 1987 (1989).

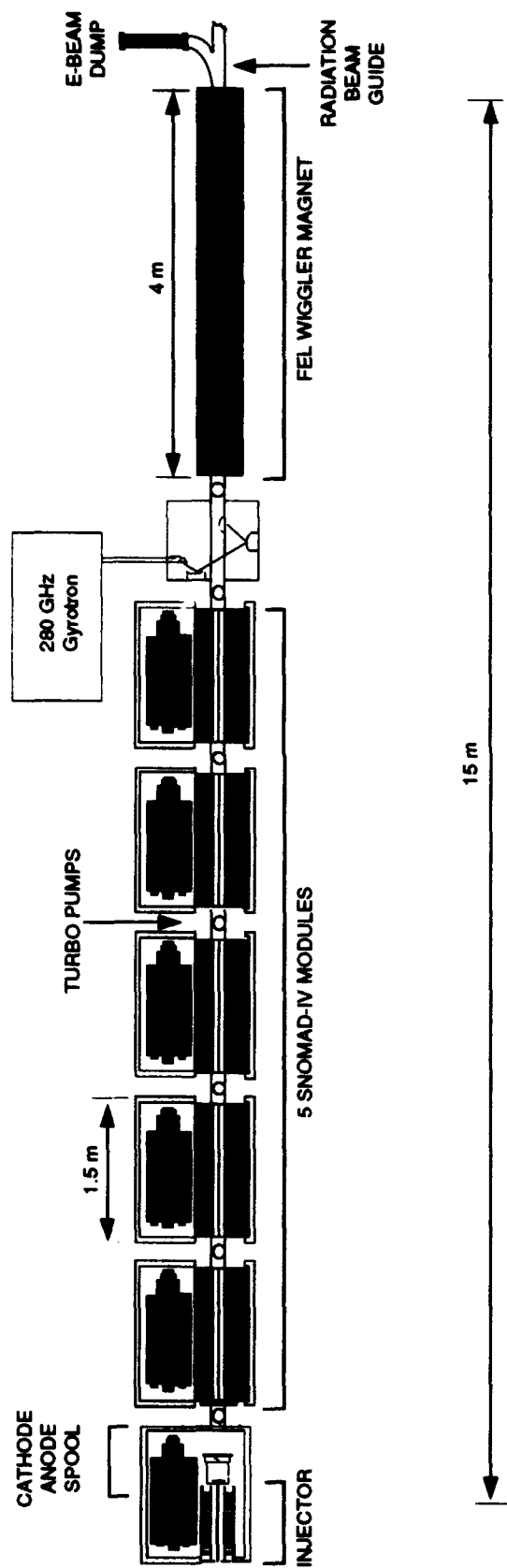


Figure 1.2: An Induction Linac Driven Free Electron Laser for ECH Heating

SECTION 2

THE SNOMAD-IV 0.5 MeV INJECTOR

The SNOMAD-IV induction linear accelerator injector is a self contained 0.5 MeV accelerator module driven by an all solid state nonlinear magnetic pulse compressor. Ten induction cells, each driven at 50 kV, produce a total accelerating voltage of 0.5 MeV. A schematic of this accelerator indicating its physical size and layout is shown in Fig. 2.1. Table 2.1 summarizes the performance specifications of SNOMAD-IV.

The use of solid state devices to replace thyratrons or spark gaps in existing pulse power designs is key to the development of reliable, high average power induction linear accelerators. When combined with the technology of nonlinear magnetic compression circuits, SCR commutated drivers provide operating capabilities at pulse repetition rates and lifetimes greatly exceeding those of thyatron designs. The SNOMAD-IV driver is capable of delivering up to 50 Joules per pulse at a rate of up to 5 kHz (cw), to an induction cell load. A circuit diagram of SNOMAD-IV is shown in Fig. 2.2. Commercially available SCRs are utilized in the command resonant charge and intermediate storage power supply. Thyatron switches have been completely eliminated permitting significantly higher repetition rate operation and a reduction in cost and size.

The input is split into multiple arms, each completely isolated from the other, allowing each SCR to perform individually. Isolation between arms is provided by the saturable inductors in series with each SCR. The commutator arms deliver a 55 Joule energy pulse into the first stage energy storage capacitors, C_1 . C_1 is charged to 1 kV in 10 μ sec. The charging time has been chosen so as not to exceed the dI/dt capabilities of commercially available SCRs. Low loss, aluminized polypropylene capacitors are utilized in the first energy storage stage, C_1 . These capacitors are coupled via a low inductance bussing network to a metglass saturable inductor,

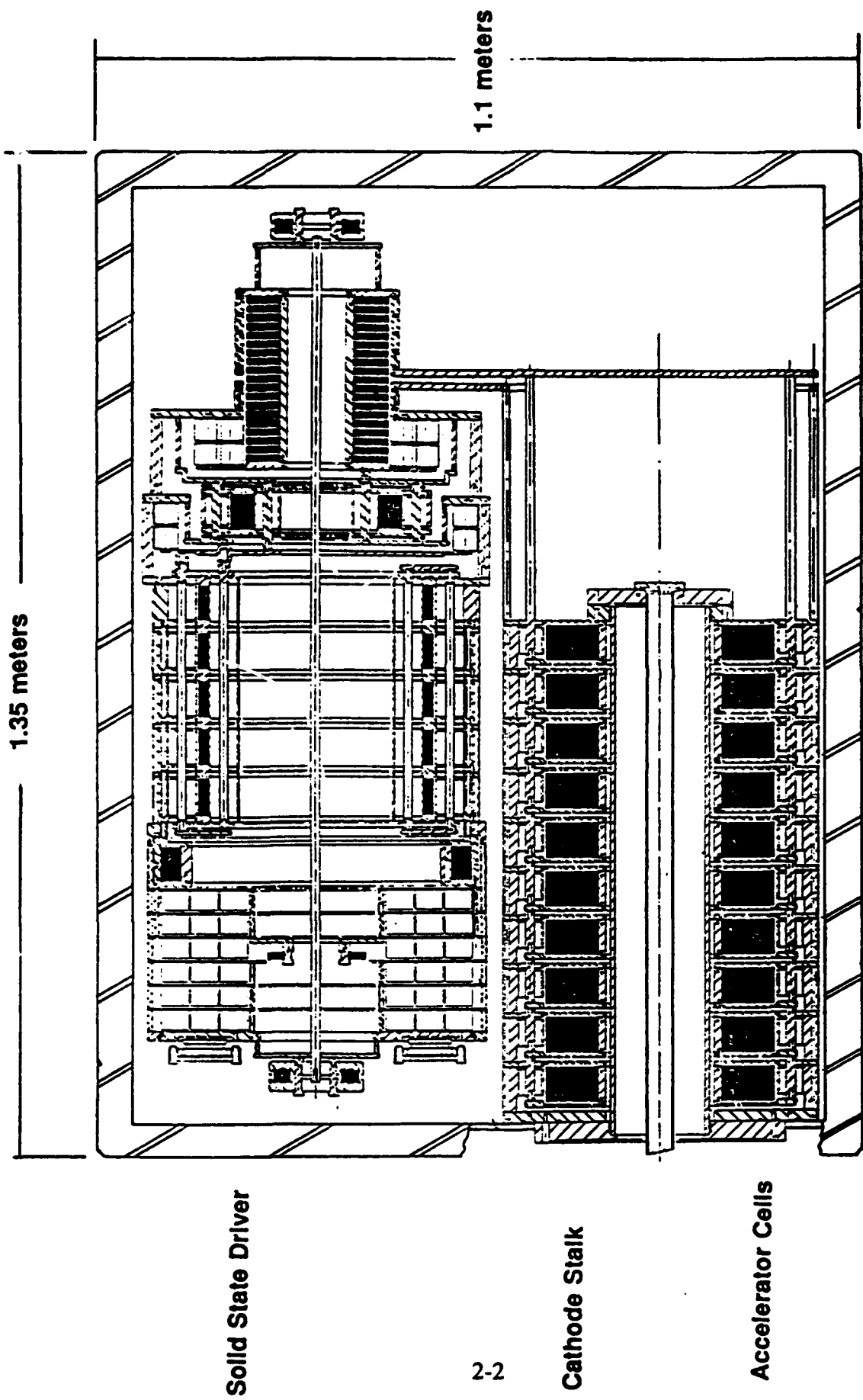


Figure 2.1: SNOMAD-IV 0.5 MeV Electron injector module

Table 2.1: Design Parameters of the SRL Prototype Injector

Accelerator Parameters

Beam Energy	0.5 MeV
Beam Current	600 amp
Pulse Length	50 nsec
Pulse Repetition Rate	5 kHz
Single Pulse Energy	30 joules
Voltage per Cell	125 kV
Accelerating Gradient	0.5 MeV/meter
Pipe Radius	6.35 cm
Gap Field Stress	150 kV/cm
Cathode	3.5" ϕ Dispenser

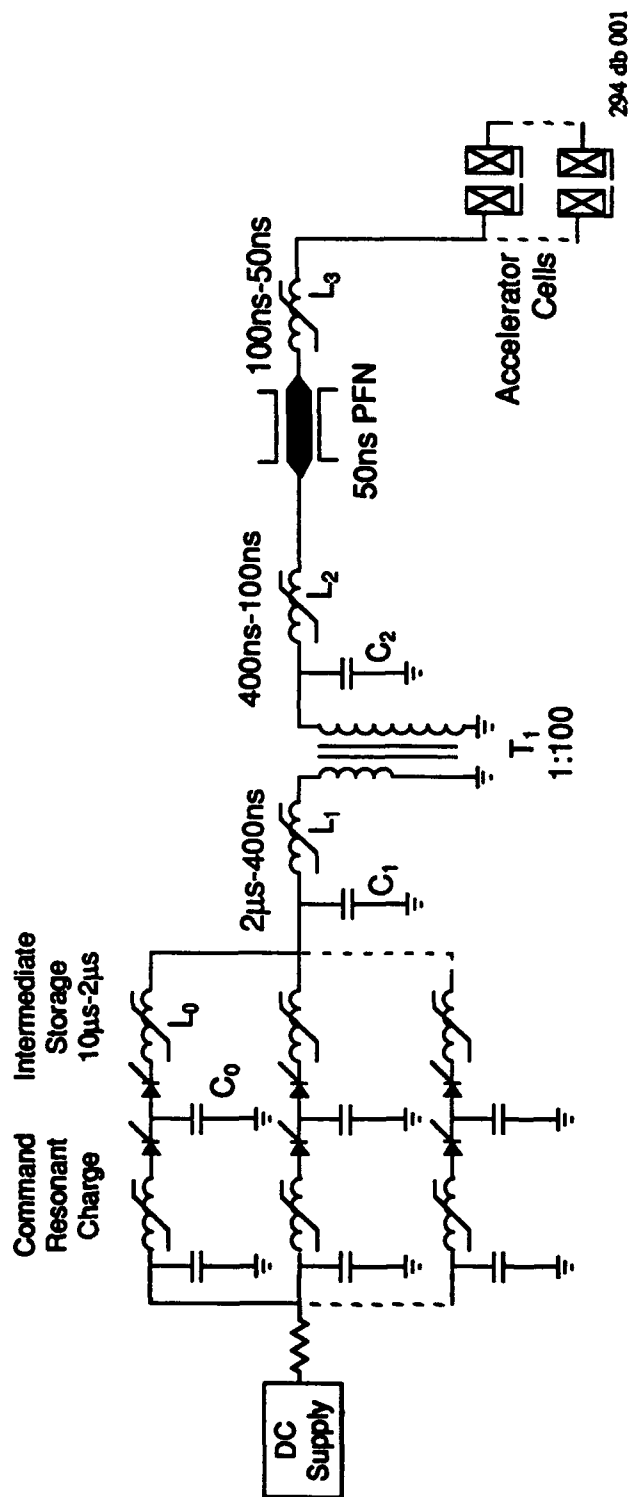


Figure 2.2: An electrical schematic of the SNOMAD-IV solid state driver

L_1 . L_1 is designed so that saturation occurs following the termination of the 2 μ sec charging pulse. Once saturated, the energy stored in C_1 is discharged into the primary of a 1:100 step-up pulse transformer, T_1 , in 400 ns thereby achieving a temporal compression of 5. This results in a corresponding increase in the peak power level.

The secondary of T_1 charges a bank of strontium titanate capacitors, C_2 , to 100,000 volts. T_1 and the second stage compression inductor, L_2 , both utilize metglas cores. Metglas is a silicon-iron alloy, developed by Allied Chemical Co, with a resistivity that is three times higher than most ferro-magnetic materials. L_2 has a charging time of 400 ns and a discharge time of 100 ns. This is the last stage in the compression chain where metglas can be employed. A saturation time of less than one microsecond results in excessive losses due to eddy currents. The second stage inductor, L_2 feeds a 50 ns pulse forming network (PFN) to 100 kV in 100 ns. Input coupling to the PFN is accomplished at its electrical midpoint which allows for charging twice as fast as could be accomplished by coupling to either end. However, if the charging time becomes too short with respect to the output pulse length, remnants of the charging waveform can appear on the output pulse as voltage fluctuations. The output inductor stage, L_3 , is a ZnNi ferrite saturable inductor which delivers the 50 kV pulse to the output transmission line. L_3 has been carefully designed to take advantage of the high dielectric constant ($\epsilon_r \approx 12$) of the ferrite. This single turn compression stage operates to some extent as a shock line. Once saturated, the ferrite forms the medium for a transmission line with an impedance close to that of the PFN.

Special care has been taken in the design of SNOMAD-IV to minimize the saturated inductance of the compression reactors L_1 , L_2 and the transformer windings of T_1 . The ferrite core volume, required to obtain a given temporal compression, τ_c , in a nonlinear magnetic pulse compression stage is proportional to the square of the saturated inductance.

$$V_{ferrite} = \tau_c^2 E \frac{\mu_0 \pi^2}{4 B_{sat}^2 P_f^2}$$

where B_{sat} is the available flux swing of the ferrite, P_f is the packing factor and E is the single pulse energy. The packing factor is defined as the ratio of the ideal toroidal inductance to the

actual device inductance including stray inductance. It is essential to minimize the core volume if efficient operation is to be achieved since the energy lost in the compression reactor scales linearly with the core volume.

The SNOMAD-IV accelerator cell design is shown in Fig. 2.3. This design has been optimized for accelerating beam currents of 1 kA or less with pulse durations of 50 to 100 nsec. Each cell utilizes a metglas core measuring 6.75 inches I.D. by 12.75 inches O.D. by 2.0 inches in length. The cells are fed by a common bus which supplies 50 kV of drive from the SNOMA driver. Several innovative features have been incorporated into the mechanical design of the accelerator cell assembly to simplify the construction and lower its cost. In the injector accelerator cells, a quartz tube separates the evacuated beam pipe from the freon or oil filled accelerator gap and core region of the cell. In conventional accelerator cell designs, the gap and core winding are placed in the high vacuum region shared by the beam. This requires that these materials have ultra-high vacuum compatibility and that the electric field strengths be maintained below the vacuum break-down limit. Isolating these materials from the vacuum permits less expensive materials to be utilized and allows an insulating dielectric liquid to fill the high field gap region. The induction cells used in the 1 MeV accelerating modules will use more conventional ceramic alumina rings to provide the vacuum interface in the accelerator gap region.

An induction cell is a high impedance transmission line transformer filled with ferrimagnetic or ferromagnetic materials with the electron beam forming the single turn secondary winding. The e-beam gains energy equal to the drive voltage as it passes through each cell and appears as a resistive load in parallel with the accelerator cell impedance.

If the accelerator is to be efficient, the losses in the accelerator core must be negligible in comparison to the energy coupled into the electron beam. This requires that the characteristic impedance of the transmission line, Z_{line} , which forms the cell must be large compared to the impedance of the beam, $Z_{beam} = V_{line}/I_{beam}$. Typically, vacuum filled accelerator cell has a characteristic line impedance, Z_{line} , of less than 100 ohms.

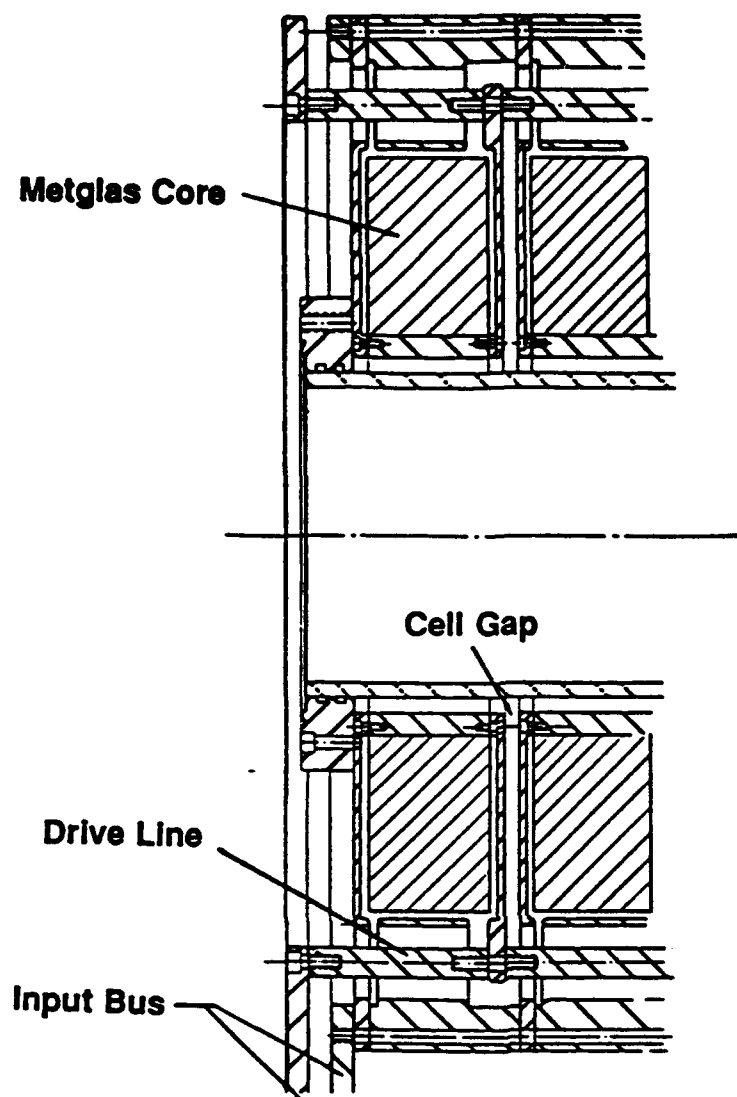


Figure 2.3: SNOMAD-IV accelerator cell

The impedance of an accelerator cell can be increased significantly by one of two methods: by filling the cell with a high permeability, low permittivity material, $(\mu_r/\epsilon_r)^{1/2} > 1$ or operating the cell as a resonant transmission line. The disadvantage of resonant structures is that the cavity is never resonant with a single mode. Wake fields produced by the electron beam can feed energy into spatially antisymmetric modes which can steer the beam electrons off axis. This sets an upper limit to the total charge which can be accelerated during an rf cavity decay time.

An induction cell is a non-resonant transmission line and, if properly designed, stores neither the drive fields nor the beam wake fields. This dramatically increases the practical operating e-beam current of the induction cell over that of the rf resonant cavity. However, it also constrains the minimum efficient operating current. Induction linacs which provide short pulses (≤ 50 ns), are usually filled with ferrimagnetic material (ferrite) to increase the impedance of the cell; for long pulses ($50 \text{ nsec} \leq \tau_p \leq 1 \text{ } \mu\text{sec}$) ferromagnetic materials such as Si-Fe, metglas, or superpermalloy are employed. Most high frequency ferrites have dielectric constants of order $\epsilon_r \simeq 10$ and permeabilities of order $\mu_r \simeq 1000$. With ferrite as a medium, the characteristic transmission line impedance is increased over the vacuum value by a factor of $(\mu_r/\epsilon_r)^{1/2} = 10$, yielding an effective shunt impedance as high as several hundred ohms. The use of ferrite also shortens the required physical length of the transmission line since the group velocity, $v_g = c/(\mu_r\epsilon_r)^{1/2}$, in a ferrite filled transmission line is decreased by 100 fold.

The design of an induction accelerator cell is governed by the basic operating principles discussed above. The length (h) of the ferrite loaded transmission line is determined by the pulse length and the electrical characteristics of the ferrite.

$$2h \geq \tau_p \frac{c}{\sqrt{\epsilon_r \mu_r}} \approx \frac{\tau_p c}{100} \quad (1)$$

In practice, the best performance is achieved by setting $h = \tau_p c/100$, thereby setting the line length equal to a single transit time rather than a round trip time. The reason is that ferrite properties are field dependent and the minimum ferrite volume is achieved by designing for a single transit time. However, the additional size and cost of achieving this improvement in

performance may not be required. Making h longer than a transit time has no benefit since the additional ferrite will not be used during the pulse.

The radial dimensions of the ferrite $(r_o - r_i) = \Delta R$ is set by the drive voltage and the maximum flux swing available in the ferrite. The ferrite must not be permitted to saturate as the wave generated by the drive pulse is transmitted down the line. The magnetic flux density, B , in the ferrite is related to the drive voltage, V_{cell} , and cross sectional area of the ferrite, A , by the following relationship

$$V_{cell} = \oint \mathbf{E} \cdot d\mathbf{l} = -\frac{d}{dt} \int_A \mathbf{B} \cdot d\mathbf{A}$$

$|\mathbf{B}|$ must be maintained below the saturation flux density, B_{sat} , of the ferrite. Thus, the minimum size of the ferrite which fills the accelerator cell must then satisfy the relationship

$$V_{cell} < B_{sat} v_g r_i \ln \left(\frac{r_o}{r_i} \right) \quad (2)$$

Typically, $B_{sat} \simeq 0.6 \text{ Wb/m}^2$.

The beam pipe radius, R_{pipe} , is determined by three competing requirements: reducing growth of the beam break-up instability; designing for high shunt impedance; and designing for minimum cost and weight of the accelerator cell.

The beam break-up (BBU) instability arises from the excitation of azimuthally asymmetric cavity modes in the accelerator cell. These modes are characterized by asymmetric longitudinal electric fields and transverse magnetic field on axis which cause sweeping of the electron beam tail. This instability sets the minimum pipe radius and is therefore critical in determining the cost of the accelerator cells. The radial displacement of the beam, ξ , resulting from the beam break up instability depends on the pipe radius, R_{pipe} , gap width, w , total accelerating voltage, V_{acc} , beam current, I_{beam} , gap electric field, E_g , and focusing magnetic field, B .

$$\xi \propto \exp(I_{beam} w \Psi V_{acc} / B E_g R_{pipe}^2)$$

The quantity Ψ depends on the beam interaction with the TM_{1n0} beam break-up modes of the accelerator cell. The beam interaction with the cell must be minimized by reducing the beam

coupling to the cell and lowering the Q of the cavity. This is accomplished by insuring that the beam induced fields are coupled out of the cell via the accelerator gap and damped in the ferrite. If a ceramic interface is used its angle is also chosen so that all TM modes excited by the beam will pass through the ceramic into the ferrite. To preserve beam quality and insure good transmission of the beam through the accelerator, an overall amplification of beam displacement due to BBU of less than five must be maintained.⁽⁷⁾

In theory it should be possible to offset the effects of a small beam pipe diameter by arbitrarily increasing the focusing magnetic field. In practice, however, as the focusing field is increased to suppress beam break-up, the number of betatron wavelengths in the accelerator increases. This leads to cork screwing and increased beam break-up excitation. Tuning becomes more complicated as the radial position of the beam becomes a rapidly oscillating function of time.

The operating current, total accelerator voltage, and pulse length of an induction linac are usually restricted by the requirements of the microwave generation device. However, the accelerator cell gap voltage remains an unspecified parameter. The accelerator gradient is linearly proportional to the gap voltage and, therefore, designing for a high gap voltage yields the shortest accelerator. However, the accelerator weight and cost increases rapidly with increasing acceleration gradient. The coupling coefficient (defined as the fraction of electrical pulse energy deposited in the beam) is independent of the gradient and therefore the only penalty paid for reducing the accelerating gradient is an increase in overall length of the accelerator. Additionally, for constant BBU growth the accelerator weight and cost increase exponentially with $I_{beam}^{1/2}$. These design considerations are discussed in detail below.

The coupling coefficient, K , for an induction accelerator cell is found by computing the shunt impedance, $Z_{shunt} = Z_{line}$, of the ferrite filled transmission line and the load imposed by the e-beam, Z_{beam} ,

$$K = \frac{Z_{shunt}}{Z_{beam} + Z_{shunt}}$$

where

$$Z_{shunt} = \frac{1}{2\pi} \sqrt{\frac{\mu}{\epsilon}} \ln \left(\frac{r_o}{r_i} \right)$$

$$Z_{beam} = \frac{V_{cell}}{I_{beam}}$$

Under the assumption that the cell gap voltage is related to the minimum ferrite radius by Eq. (2), the shunt impedance and coupling coefficient can be written,

$$Z_{shunt} = \frac{1}{2\pi} \mu \frac{V_{cell}}{B_{sat} r_i}$$

$$K = \frac{1}{1 + \frac{2\pi B_{sat} r_i}{\mu I_{beam}}}$$

A plot of K versus ferrite core inner radius, r_i , for several beam currents from 1 kA to 5 kA is shown in Fig. 2.4. The coupling coefficient increases with increasing beam current and decreasing inner radius.

The total cost and weight of the accelerating structure is linearly proportional to the volume of the ferrite core, $V_{ferrite}$

$$V_{ferrite} = \frac{V_{acc}}{V_{cell}} h \pi (r_o^2 - r_i^2) \quad (3)$$

Using Eq. 2 to solve for r_o in terms of V_{cell} and B_{sat} and substituting into Eq. 3 yields

$$V_{ferrite} = \frac{V_{acc}}{V_{cell}} v_g \tau_p \pi r_i^2 \left(\exp \left(\frac{2V_{cell}}{B_{sat} v_g r_i} \right) - 1 \right) \quad (4)$$

The ferrite core volume required per MeV of acceleration is plotted as a function of accelerator cell gap voltage for several accelerator cell inner radii, r_i . For large values of the exponential argument in Eq. 4, the ferrite core volume increases exponentially with gap voltage. For a specified gap voltage, there exists an inner radius, r_i , which yields the smallest ferrite core volume according to Fig. 2.5. Likewise, we can see that the minimum ferrite core volume required is achieved by operating with the lowest possible gap voltage. Other constraints (i.e. restricting the overall length of the accelerator) may restrict the gap voltage to be larger than some minimum value. Figures 2.5 and 2.6 show that designing for the smallest inner core radius

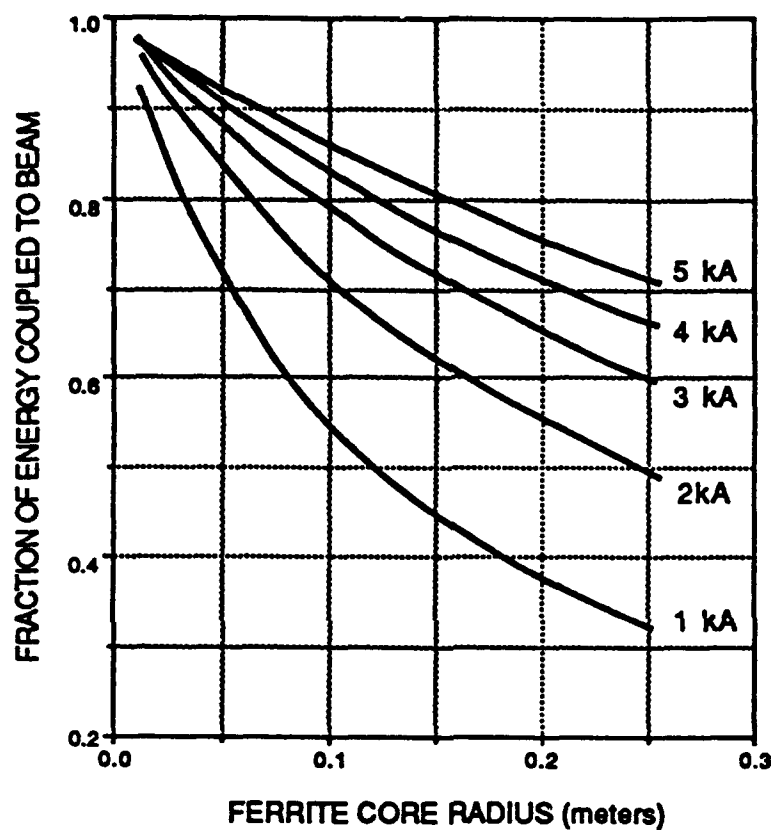


Figure 2.4: Coupling coefficient, K , versus ferrite core inner radius for beam currents from 1 to 5 kA. Ferrite parameters: $\mu_r = 400$, $\epsilon_r = 12$.

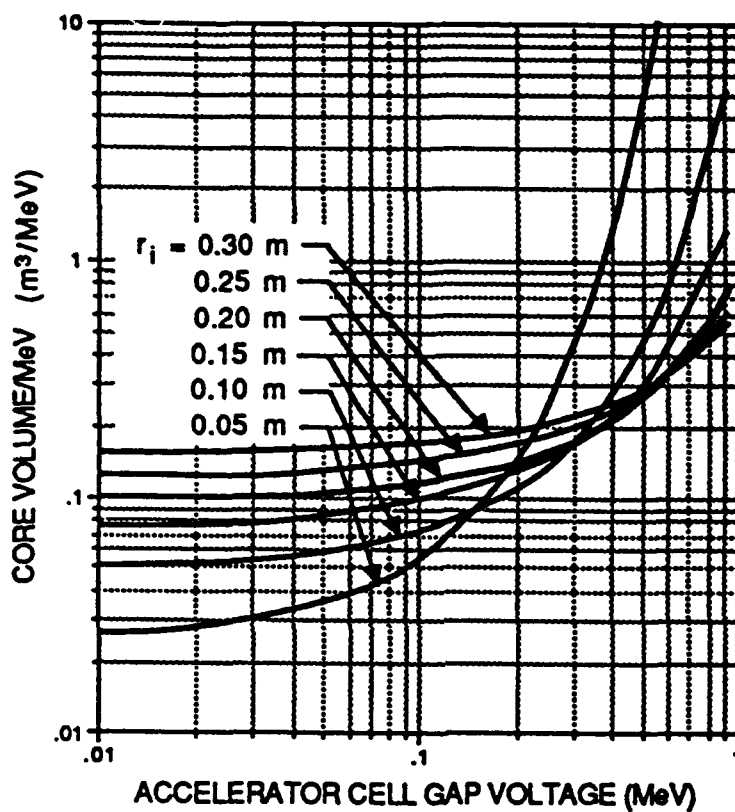


Figure 2.5: Required ferrite core volume, ν_{ferrite} , versus accelerating gap voltage for $r_i = 0.05, 0.10, 0.15, 0.20, 0.24, 0.30$ meters. Ferrite parameters: $\mu_r = 400$, $\epsilon_r = 12$, $\tau_p = 50 \text{ nsec}$.

and lowest gap field will always yield the most economical design. However, arbitrarily reducing these parameters at fixed beam current will result in the onset of the beam break-up instability.

An assembly drawing of the SNOMAD-IV driver is shown in Fig. 2.6 and Fig. 2.7. Five hundred volt DC power enters through the eight command resonant charge SCRs which are mounted on the left deck of the driver assembly. Eight Intermediate storage SCRs are mounted in reverse polarity from the same deck. The number of SCRs has been chosen so that the dI/dt rating of each device is not exceeded. The saturable inductors, labeled L_0 , isolate the branches of the intermediate storage power supply. These are all wound from a common toroidal core which is mounted on the first compression stage capacitor bank, C_1 . The first stage saturable inductor, L_1 , is single turn design which will utilize a 0.6 mil toroidal metglas core. The discharge of C_1 through L_1 and T_1 to C_2 results in a 5 to 1 temporal compression with a voltage gain of 100. The 1:100 step-up transformer will be wound on four metglas toroidal cores. The design achieves a large step-up ratio with a twenty five turn secondary and fractional, one quarter turn, primary made possible by the use of four transformer cores.

In the second compression stage, high voltage strontium titanate ceramic capacitors, C_2 , will be used. Unlike barium titanate, strontium titanate does not suffer from piezoelectric mechanical failure under high repetition rate operation. The second stage saturable inductor, L_2 , will be a ten turn toroidal inductor wound on a 6.75 inch I.D. X 9.65 inch O.D. X 2 inch wide core. L_2 discharges C_2 into a pulse forming network with a electrical length of 25 nsec. The PFN is a hybrid design consisting of lumped capacitors and distributed inductance. This permits the design to be significantly more compact than either a water filled transmission line or a lumped PFN and allows the electrical length to be varied by the addition of capacitive elements. The output saturable inductor, L_3 , serves as a passive high speed switch to discharge the PFN into the accelerator cell load. L_3 will be constructed using nineteen toroidal ferrite pancakes. A zinc-nickel ferrite has been selected for the output stage to minimize losses and provide fast switching.

A bias conductor, placed on the axis of the driver, will be used for biasing the metglas and ferrite inductor cores into saturation and to provide the reset current between pulses. Both ends of the bias conductor will be terminated with a powdered iron core noise suppression inductor. This prevents electrical noise, generated inside the driver, from being transmitted out along the bias conductor. The assembled driver will be 20 inches in diameter and an overall length of 44 inches. Table 2.2 summarizes the design specifications of the SNOMAD-IV driver.

The SNOMAD-IV driver is capable of powering a 0.5 MeV injector induction cell assembly. In the injector these cells utilize metglas core induction cells. An assembly drawing of the injector showing the induction cells, drive line, cathode stalk and input bus from the driver is shown in Fig. 2.8.

Each induction cell uses a metglas core measuring 6.75 inches I.D. X 12.75 inches O.D. X 2 inches wide. The choice of metglas over ferrite was chosen as a core material for several compelling reasons. The saturation flux density of metglas is a factor of five times higher than nickel-zinc ferrites, allowing a significantly more compact design. In addition, a significant cost savings is realized by using metglas and large toroidal cores are more easily fabricated than ferrite cores. The primary disadvantage of a metglas filled induction cell design are limitations imposed by its electrical pulse performance characteristics. A metglas filled cell exhibits characteristics which are inductive rather than transmission like. As a result, the electrical impedance of the cell decreases as a function of pulse duration. In contrast, the ferrite filled cell presents a constant impedance for the duration of the pulse. This difference can manifest itself by producing an inductive voltage droop during the pulse. The impact is severe on the pulse shape. The square output pulse from the SNOMAD-IV driver is rounded at the beginning by the capacitance of the metal tape wound cores and then the lumped inductance causes a droop toward the end of the pulse. For purposes such as X-ray sterilization and E-Beam processing these effects cause little trouble. For the purposes of an FEL the results are quite serious.

The injector assembly and the 1 MeV module assembly will differ in design in two significant

Table 2.2: SNOMAD-IV Performance Specifications

Input Power Requirements:

Energy/pulse	57.5 joules
PRF	5 kHz
Power	287.5 KW
Voltage	600 volt
Current	481 Amps

Command Resonant Charge

Capacitance	4×640 μ fd
Voltage	600 volts
Energy	922 joules
Stored charge	1.54 Coulombs
τ charge	$\leq 120 \mu$ sec
I peak	1.3×10^3 Amp
dI/dt	3.4×10^1 A/ μ sec
I_T (RMS)	650 Amps
dI/dt per device	8.5 A/ μ sec (4× West Code)
Commutation losses	~ 2.5 joule
Charge Core Type	Powdered Iron
# Turns Charge Core	4×20
Charge Core geometry	4×4×3.0" ID × 5.218" OD × .8" Wide
E.R. Core Type	Powdered Iron
# Turns E.R. Core	60
Core geometry	4×2×3.0" ID × 5.218" OD × .8" Wide

Intermediate Storage

Capacitance	90.8 μ fd
Voltage	1,100 volts
Energy	55 joules
Stored charge	10.0×10^{-2} Coulombs
τ discharge	$\leq 7.5 \mu$ sec
I peak	20.9×10^3 Amp
dI/dt	8.77×10^3 A/ μ sec
I_T (RMS)	2773 Amps
dI/dt per device	1096 A/ μ sec (8× West Code)
Sat. Asst. Core Type	CMD-5005
# Turns	16 × 5
Core geometry	3.5" ID × 5.8" OD × .5" Wide
Commutation losses	~ 2.5 joule

1st Stage

Capacitance	90.8 μ fd
Voltage	1075 volts
Energy	52.5 joules
Core Type	.6 Mil × 2605 CO

Table 2.2: SNOMAD-IV Performance Specifications (Continued)

# Turns	1
Core geometry	1×15.3" ID × 17.8" OD × 2" Wide
$\int V \cdot dt$	$\sim 4 \times 10^{-3}$ Vsecs
Lsat	1.588 nh + .4 nh (STRAY) = 1.988 nh
τ discharge	944 nsec
Losses	~ 1.275 joules (.675 cores, .6 caps)
Core volume	21.557×10^{-4} m ³ , 10.8 kg
Transformer	
Core Type	2605S3A
# Turns (PRIM)	1/5
# Turns(sec)	20
Losses	$\leq .5$ joules
Peak stress	76.7 kV/cm at 107/2 kV (.5" dia. Rod in 1.50 " dia. hole)
Core geometry	5×12" ID × 13.5" OD × 2" wide
2nd Stage	
Capacitance	8.96 nfd
Voltage	106.4 kV
Energy	50.72 joules
Core type	2605 CO Metglass
Core Geom.	1×6.75" ID × 9.65" OD × 2" w (1.224×10^{-3} M ²)
$\int V \cdot dt$	12 Turns × 4.80 Vmsecs/Turn = 106 kV* (1.082 usecs/2)
LSAT	.556 μ h + .1 μ h stray \simeq .656 μ h
τ discharge	170.7 nsec
Losses	~ 1.05 joules
Output Stage	
Capacitance	9.4 nfd
Voltage	102.8 kV
Energy	49.67 joules
Core type	CN-20 Ferrite
Core Geom.	18×4" ID × 8" OD × .5" w
$\int V \cdot dt$	1 Turns × 8.16×10^{-3} usecs/Turn = 102 kV (160 nsec/2)
LSAT	31.2 nh
τ discharge	~ 40 nsec into 6 nfd
Losses	~ 2 joules

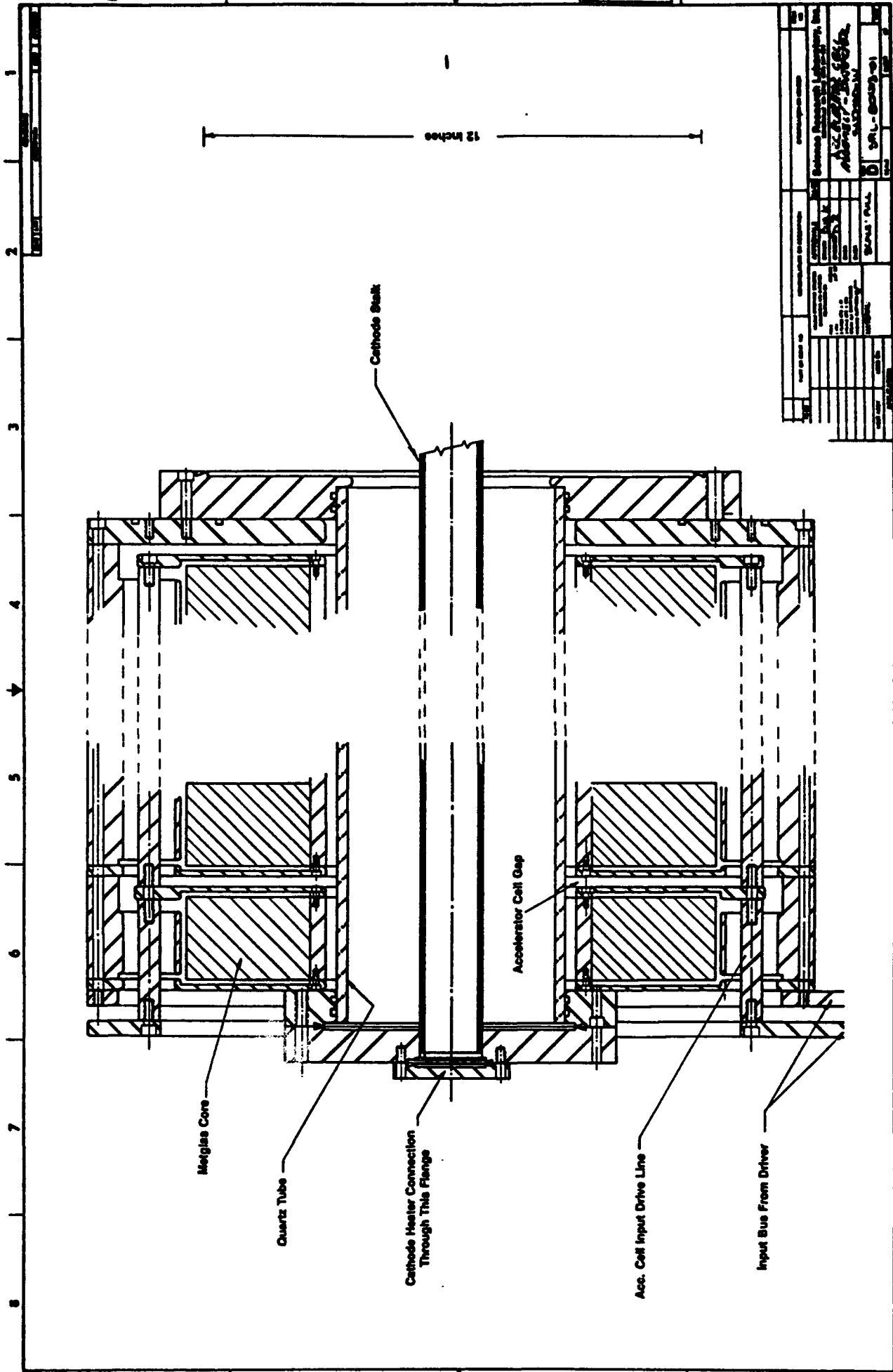


Figure 2.8: Drawing of SNOMAD-IV 0.5 MeV injector accelerator cell assembly.

ways. The injector will utilize a quartz tube as the vacuum interface. This design eliminates many sealing joints and simplifies the construction, cooling and insulation of the accelerator cells. The simplified design is made possible because there is no electron beam present in the injector cells. Electron beam propagation in the accelerator cells require that the walls be of a conducting material to prevent charge accumulation which results from lost beam electrons. Therefore, the accelerator modules will employ o-ring sealed ceramic insulators in each of the accelerator gap. In addition, each induction cell used in the accelerator module will be fitted with a solenoidal focusing magnet which is required for the propagation of high current e-beam propagation.

The injector module will be fitted with a cathode assembly and vacuum pump housing as shown in Fig. 2.9. A 3.5 inch diameter dispenser cathode will be mounted at the end of the cathode stalk and will supply up to 600 amps of electron beam current. The cathode, cathode shroud and anode ring geometry establish the charged particle extraction optics. The radius of curvature of the cathode surface determines the degree of convergence of the extracted beam.

The SNOMAD-IV driver and accelerator cell assembly is housed in a rectangular aluminum enclosure which supplies cooling and electrical shielding to both units. All high voltage bus connections between the driver and induction cells will be made within enclosure forming a self contained 1 MeV accelerator module. External connections to the module will include: 500 volt DC prime power, low voltage timing signals, and entrance and exit ports for the beam.

Several concepts have been investigated for providing cooling and electrical insulation for the driver and accelerator components within the enclosure. A freon vapor environment is sufficient to provide the necessary peak electric field break-down strength of 70 kV/cm, and will permit the accelerator to operate at a repetition rate of 20 kHz for several seconds or an average repetition rate of up to 1 kHz for an indefinite period of time. Heat removal is accomplished by transferring heat to the aluminum tank without additional heat exchangers or coolers. Filling the tank with liquefied freon or transformer oil will permit the accelerator to operate at an average

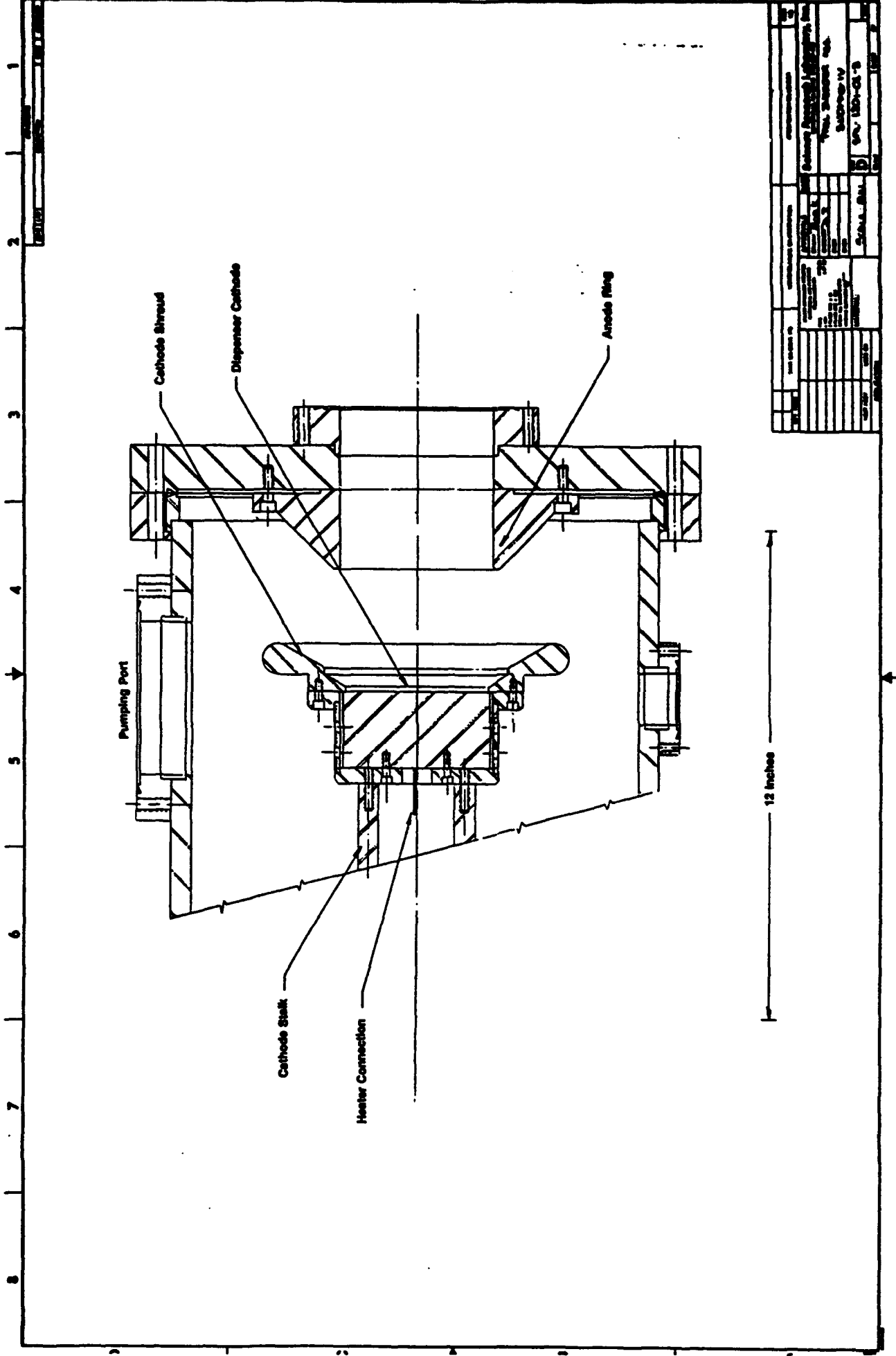


Figure 2.9: Preliminary assembly drawing of cathode extraction optics and vacuum pumping port.

repetition rate of 5 kHz for an indefinite period. In this mode of operation, the aluminum tank can not dissipate sufficient heat and must be assisted by a water cooled heat exchanger mounted within the tank.

For applications such as ECH in present generation tokamak devices, the most likely operating scenario for the proposed accelerator would require very high repetition rates (20 kHz) for short periods of time (up to several seconds) followed by extended inoperative periods (several minutes). Vapor cooling or passive oil cooling will provide sufficient heat removal for this mode of operation. Assembly drawings of the enclosure are shown in Figs. 2.10 and 2.11.

It is planned that after fabrication, assembly and high repetition rate testing of the SNOMAD-IV injector module, the device will be installed in a laboratory at the MIT Plasma Fusion Center which is equipped to provide power, radiation shielding and computerized control. Under the supervision of Dr. Richard Temkin, the accelerator will be made available to research members of the Fusion Center for developing and testing high power millimeter wave sources. SRL will assist in training MIT personnel in the operation and maintenance of the accelerator. The goal of this task will be to gain field experience in operating and maintaining a production prototype of the accelerator module. Information and experience gathered in this effort will be used to improve upon subsequent accelerator designs.

The nearly completed SNOMAD-IV injector is pictured in Fig. 2.12 as it appeared in SRL's Oakley, California facility before shipment. SNOMAD-IV is now housed temporarily in a shielded pit at SRL's Boston, Mass. facility (Fig. 2.13). Here it is being used for a variety of experiments until its new home is completed at the MIT Plasma Fusion Center.

The operating parameters of the SNOMAD-IV injector are represented by the oscilloscope traces in Figs. 2.14 and 2.15. The ringing on the voltage waveform is an artifact of the voltage diagnostic as indicated by the current waveform which should scale as directly as $V^{1.5}$. The droop caused by the Metglas accelerator cores is plainly evident on the current waveform.

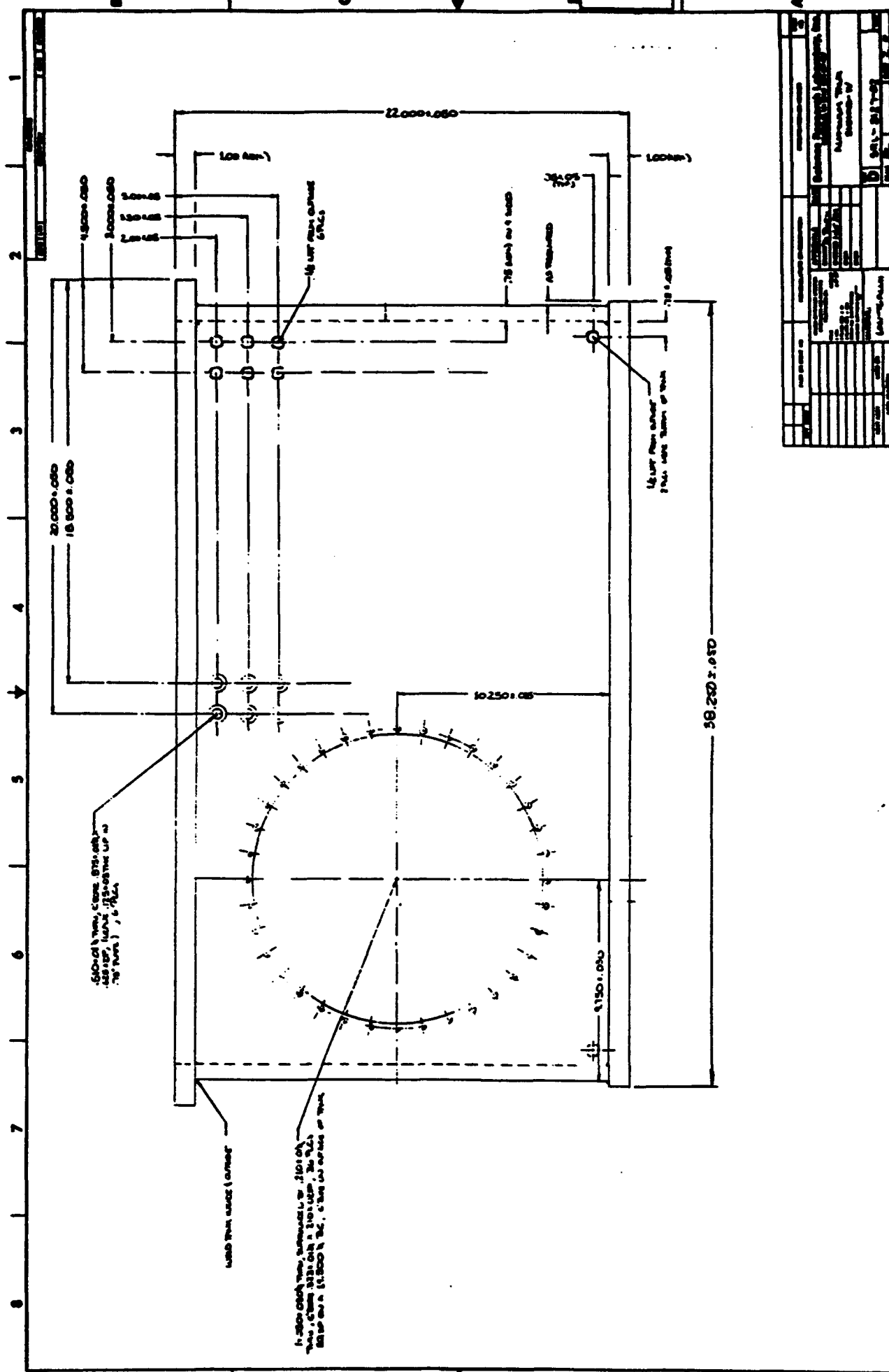


Figure 2.10: SNOMAD-IV Enclosure, elevation

SCIENCE RESEARCH LABORATORY

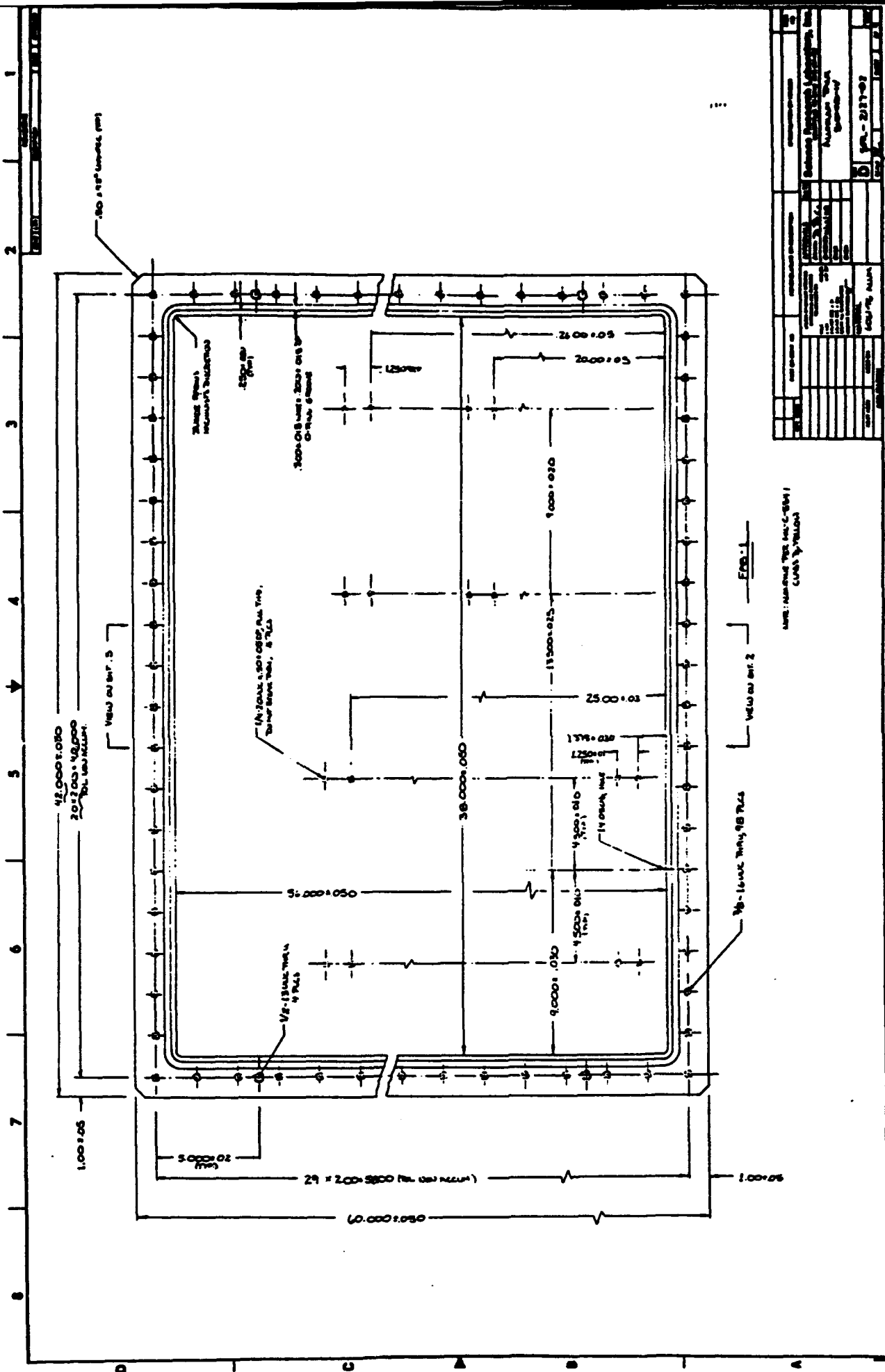
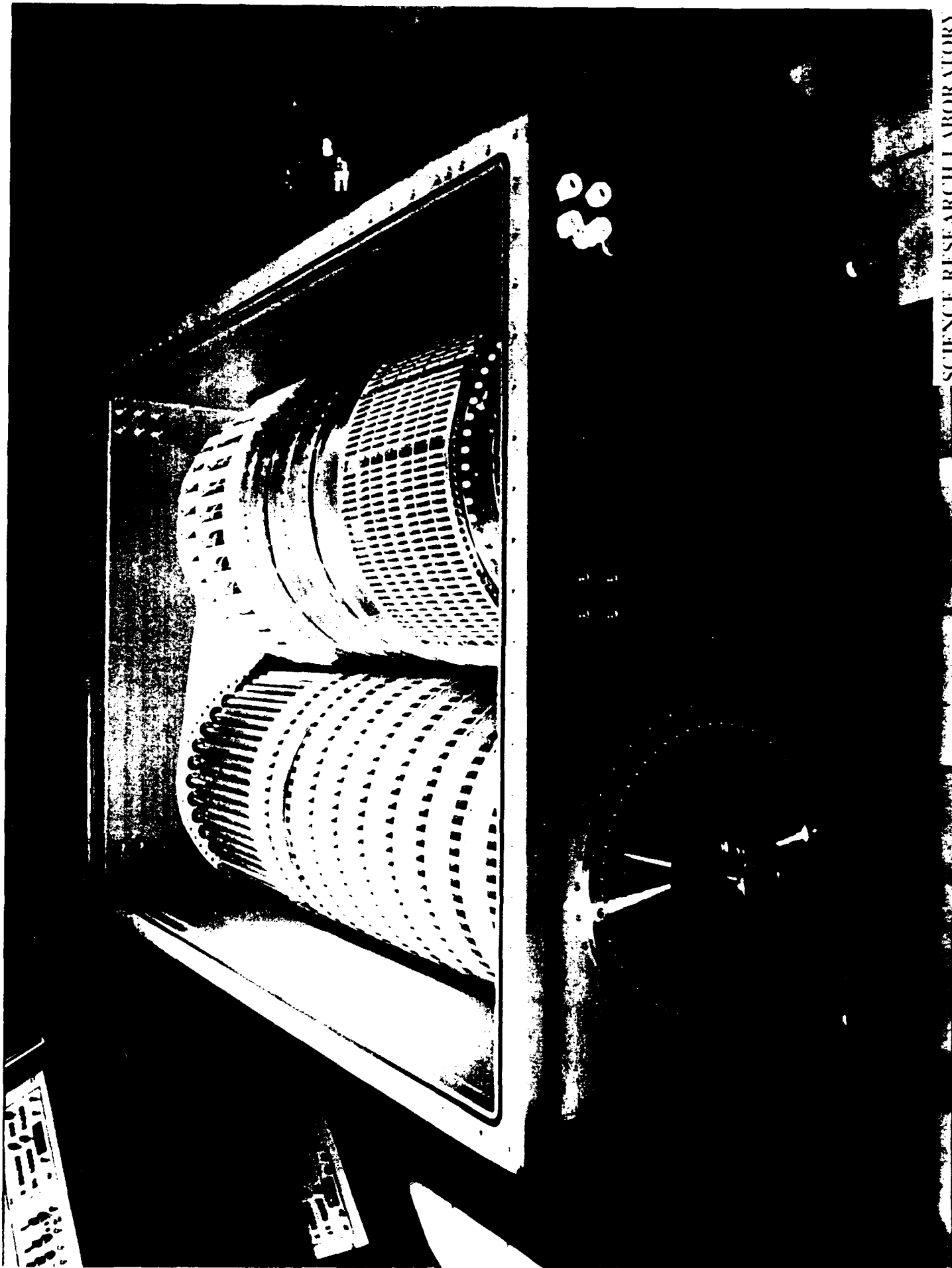


Figure 2.11: SNOMAD-IV Enclosure, plan view



SCIENCE RESEARCH LABORATORY

Figure 1-14: Photograph of the Spectral-Profile Projector and Spectral Analyzer

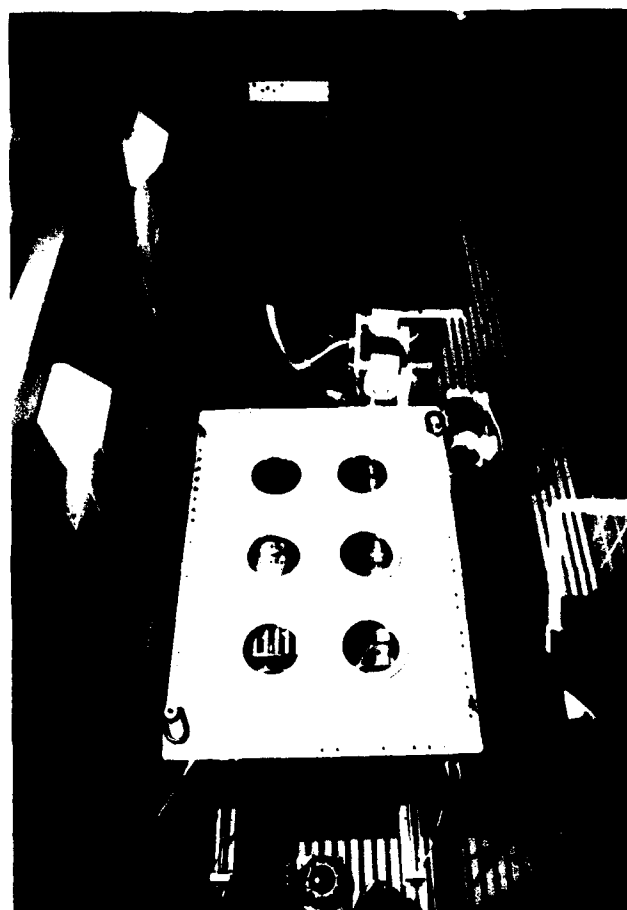


Figure 2.13: The 500 kV induction accelerator and x-ray target (inside the blue lead box) assembly in the experiment vault.

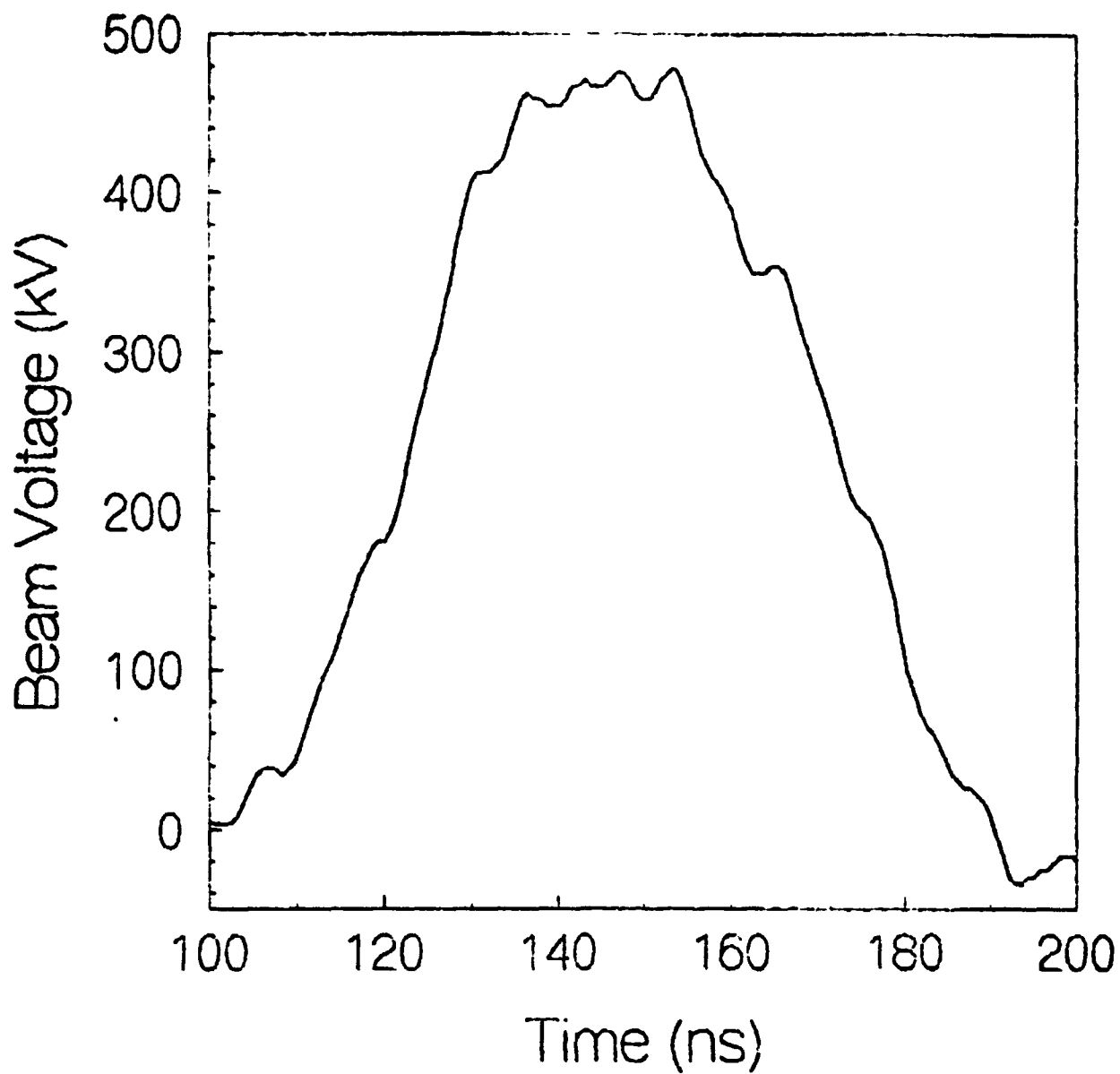


Figure 2.14: Voltage measurement using capacitive divider looking at the cathode stalk.

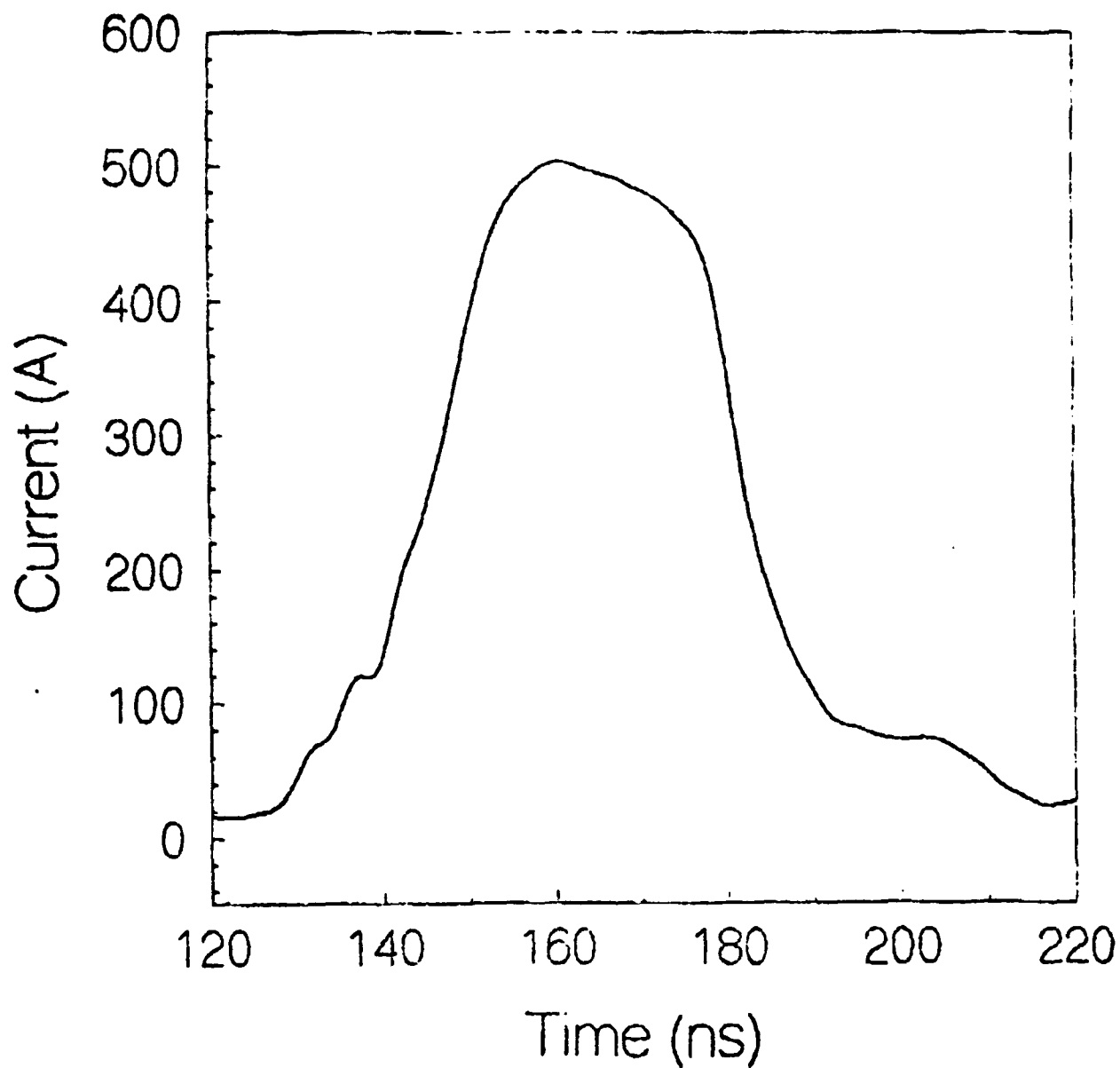


Figure 2.15: Current measured 76 cm downstream, by integrating the dB/dt signal from a single turn pickup loop.

SECTION 3

SNOMAD-IVB, 1.0 MeV INDUCTION ACCELERATOR MODULE

The first SNOMAD-IVB 1.0 MeV accelerator module has been completed. After it was finished it was temporarily installed in line with the SNOMAD-IV injector at SRL's Boston facility. This resulted in an upgrade from 0.5 MeV to 1.5 MeV for that facility. As with the SNOMAD-IV injector, the long term goal is to install this module at the MIT Plasma Fusion Center. In the meantime it is being used for studies on e-beam processing at SRL. A photograph (Fig. 3.1) of the 1.5 MeV accelerator facility shows the SNOMAD-IV, 0.5 MeV Injector in the foreground, the SNOMAD-IVB, 1.0 MeV Accelerator Module in the middle of the picture, and the beam experimental and diagnostic chamber in background.

The SNOMAD-IVB driver (Fig. 3.2) is somewhat larger than the SNOMAD-IV and supplies more than 1.5 times the output energy. A list of specifications for the SNOMAD-IVB driver is supplied in Table 3.1.

The SNOMAD-IVB input section (Fig. 3.3) contains the intermediate storage capacitors, commutator SCRs, initial compression stage and the 144:1 hybrid transformer. The output from this portion of the modulator is a 126 kV, 1.6 microsecond duration pulse which charges the 8.16 nfd, 2nd stage capacitor located at the input of the SNOMAD-IVB Output Section. It is the SNOMAD-IVB Output Section (Fig. 3.4) which further temporally compresses the pulse energy into the 40 nanosecond pulse delivered to the accelerator cells. A cutaway drawing of the entire SNOMAD-IVB Driver is presented in Fig. 3.5.

The SNOMAD-IVB Driver supplies the power to fourteen SNOMAD-IVB accelerator cells. Each SNOMAD-IVB accelerator cell (Fig. 3.6) is designed to operate at 70 kV. Unlike the SNOMAD-IV injector, we have returned to the use of ferrite in the SNOMAD-IVB accelerator cells. A picture of three induction cells during assembly is provided in Fig. 3.7.

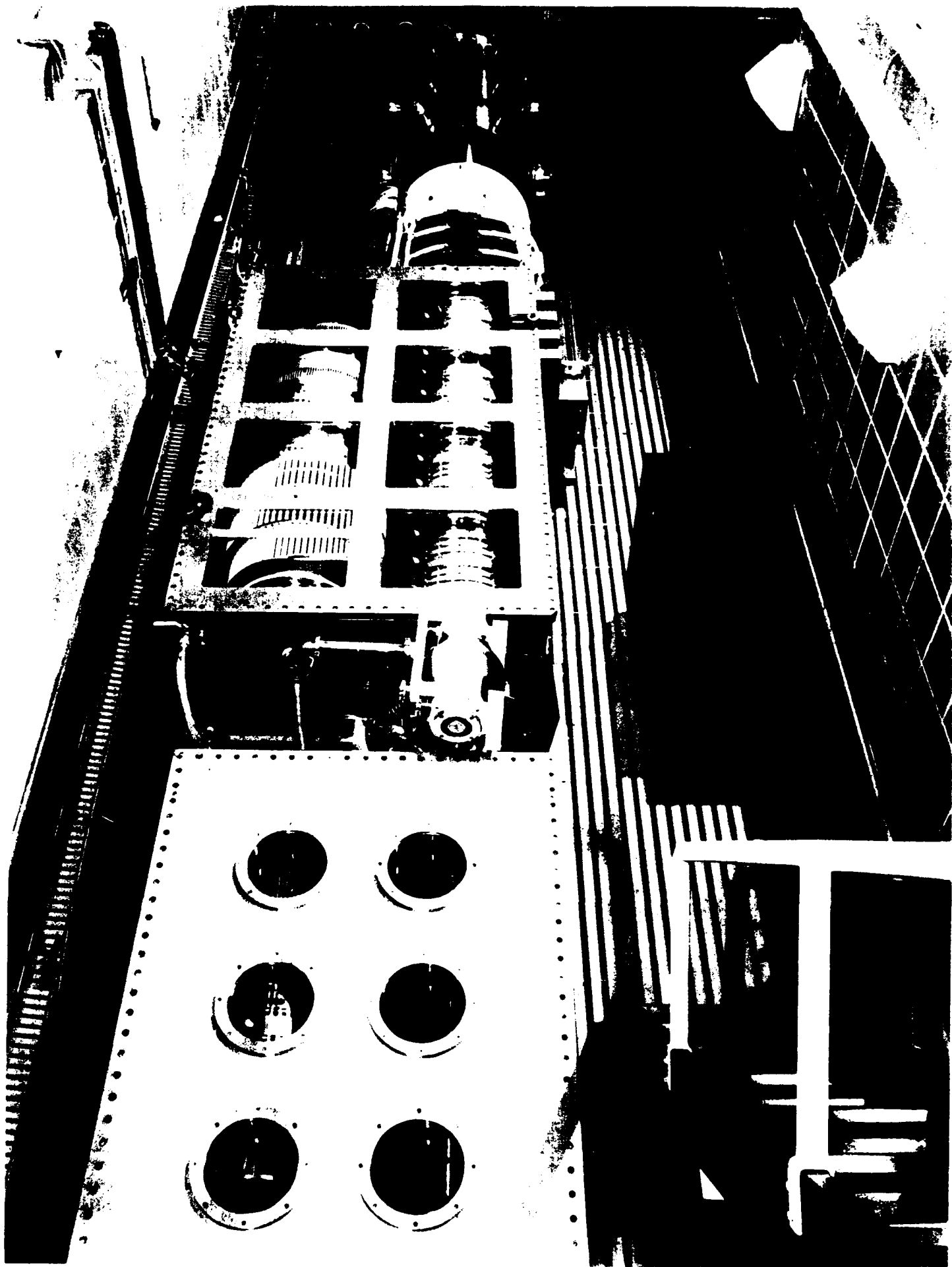
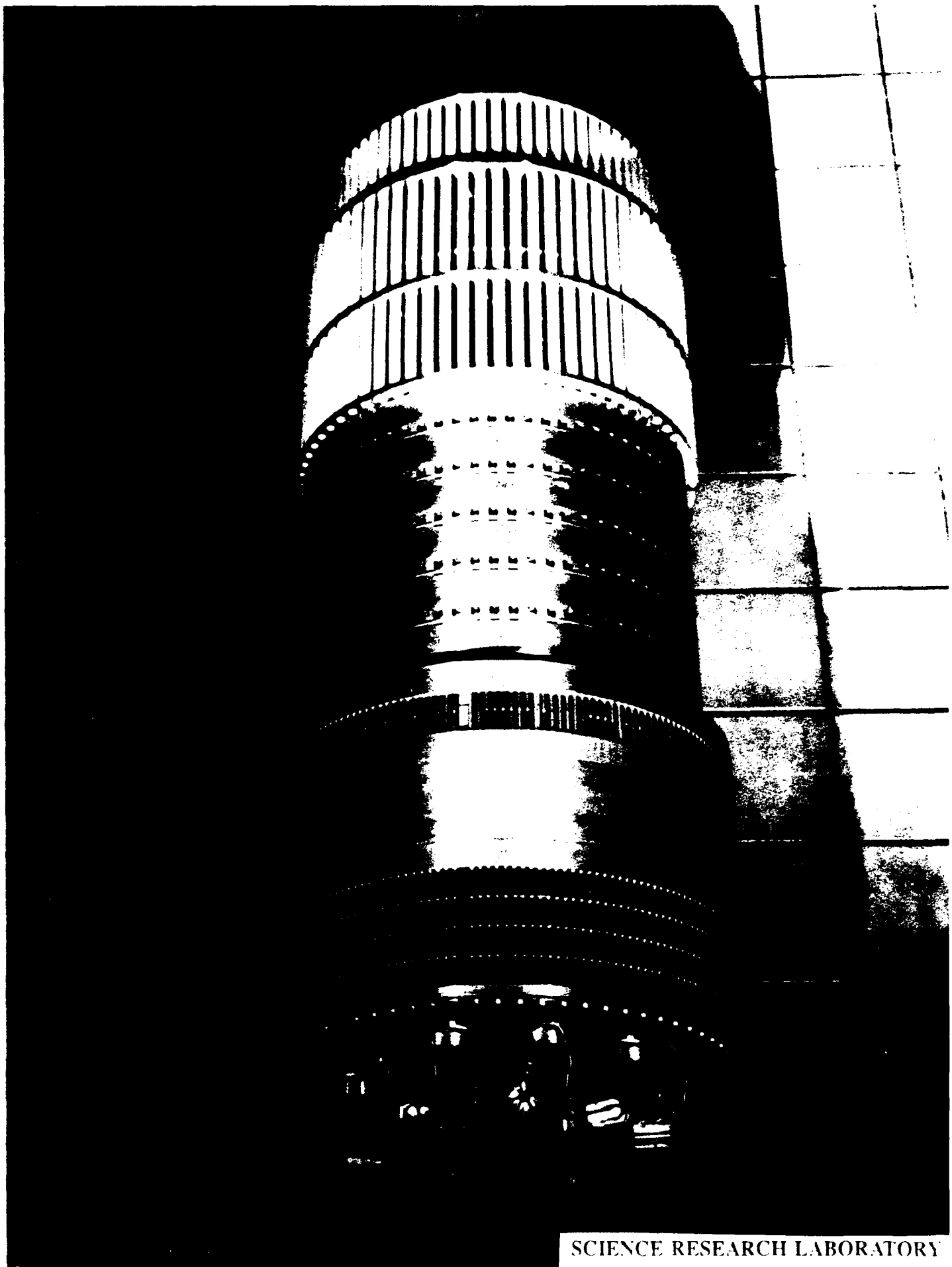


Figure 3.1: Photograph of 1.5 MeV Accelerator Installation at JRI.



SCIENCE RESEARCH LABORATORY

Figure 3.2: SNOMAD-IVB Driver

Table 3.1: SNOMAD-IVB Performance Specifications

Input Power Requirements:

Energy/pulse	75 Joules
PRF	5 kHz
Power	375 KW
Voltage	600 volt
Current	625 Amps

Command Resonant Charge

Capacitance	4×640 μ fd
Voltage	600 volts
Energy	922 Joules
Stored charge	1.54 Coulombs
τ charge	$\leq 120 \mu$ sec
I peak	2.14×10^3 Amp
dI/dt	5.6×10^1 A/ μ sec
I_T (RMS)	1073 Amps
dI/dt per device	14 A/ μ sec
Commutation losses	~ 2.5 Joule
Charge Core Type	Powdered Iron
# Turns Charge Core	4×20
Charge Core geometry	4×4×3.0" ID × 5.218" OD × .8" Wide
E.R. Core Type	Powdered Iron
# Turns E.R. Core	60
Core geometry	4×2×3.0" ID × 5.218" OD × .8" Wide

Intermediate Storage

Capacitance	150 μ fd
Voltage	1,000 volts
Energy	75 Joules
Stored charge	15.0×10^{-2} Coulombs
τ discharge	$\leq 10.0 \mu$ sec
I peak	23.5×10^3 Amp
dI/dt	7.39×10^3 A/ μ sec
I_T (RMS)	3602 Amps
dI/dt per device	924 A/ μ sec (8× West Code)
Sat. Asst. Core Type	CMD-5005
# Turns	16 × 5
Core geometry	3.5" ID × 5.8" OD × .5" Wide
Commutation losses	~ 5 Joule

Table 3.1: SNOMAD-IVB Performance Specifications (Continued)

1st Stage

Capacitance	160 μ fd
Voltage	935 volts
Energy	70 Joules
Core Type	.6 Mil \times 2605 CO
# Turns	1
Core geometry	1 \times 14.875" ID \times 17.8" OD \times 2" Wide
$\int V \cdot dt$	$\sim 4 \times 10^{-3}$ Vsecs
Lsat	1.888 nh + .4 nh (STRAY) = 2.288 nh
τ discharge	1344 nsec
Losses	~ 3.275 Joules (1.675 cores, 1.6 caps)
Core volume	21.557×10^{-4} m ³ , 10.8 kg

Transformer

Core Type	2605S3A
# Turns (PRIM)	1/6
# Turns(sec)	24
Losses	≤ 1.5 Joules
Peak stress	93.2 kV/cm at 130/2 kV (.5" dia. Rod in 1.50 " dia. hole)
Core geometry	7 \times 12" ID \times 13.5" OD \times 2" wide

2nd Stage

Capacitance	8.16 nfd
Voltage	126.4 kV
Energy	65.2 Joules
Core type	2605 SC Metglass
Core Geom.	2 \times 6.75" ID \times 9.65" OD \times 2" w (2.448×10^{-3} M ²)
$\int V \cdot dt$	12 Turns \times 8.23 Vmsecs/Turn = 126 kV* (1.57 usecs/2)
LSAT	1.098 μ h + .3 μ h stray \simeq 1.398 μ h
τ discharge	237 nsec
Losses	~ 2.05 Joules

3rd Stage

Capacitance	8.4 nfd
Voltage	122.6 kV
Energy	63.15 Joules
Core type	2605 SC Metglass
Core Geom.	1 \times 5.0" ID \times 6.8" OD \times 2" w ($.546 \times 10^{-3}$ M ³)
$\int V \cdot dt$	6 Turns \times 2.55 Vmsecs/Turn = 122.6 kV* (.250 usecs/2)
LSAT	.118 μ h + .05 μ h stray \simeq .168 μ h
τ discharge	83.4 nsec
Losses	~ 2.0 Joules

Table 3.1: SNOMAD-IVB Performance Specifications (Continued)

Output Stage

Capacitance	8.6 nfd
Voltage	119.25 kV
Energy	61.15 Joules
Core type	CN-20 Ferrite
Core Geom.	13×4" ID × 8" OD × .5" w
$\int V \cdot dt$	1 Turns × 5.04×10^{-3} usecs/Turn = 120 kV (85 nsec/2)
LSAT	23 nh
$\tau_{\text{discharge}}$	~ 40 nsec
Losses	~ 2 Joules

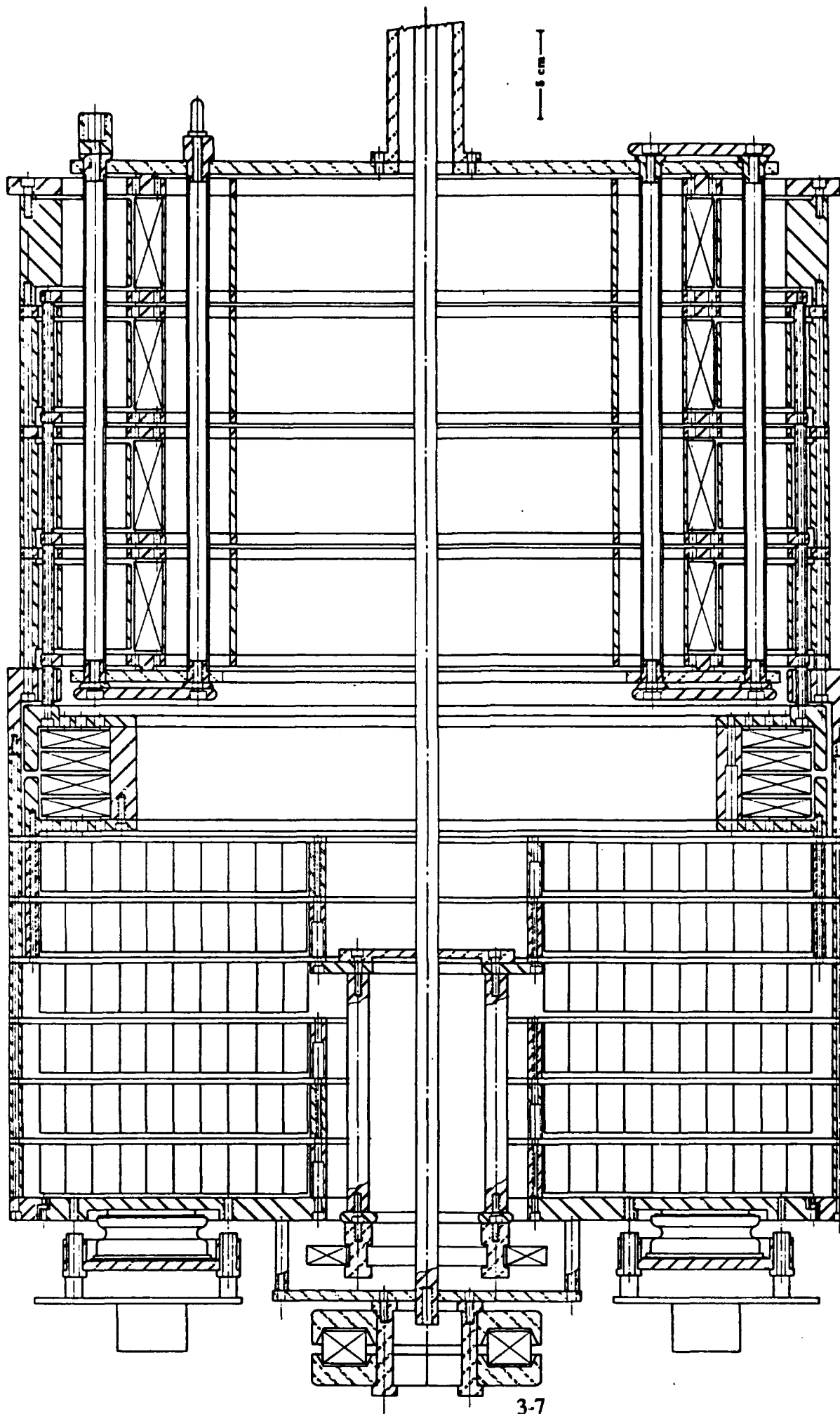


Figure 3.3: SNOMAD-IVB Input Section

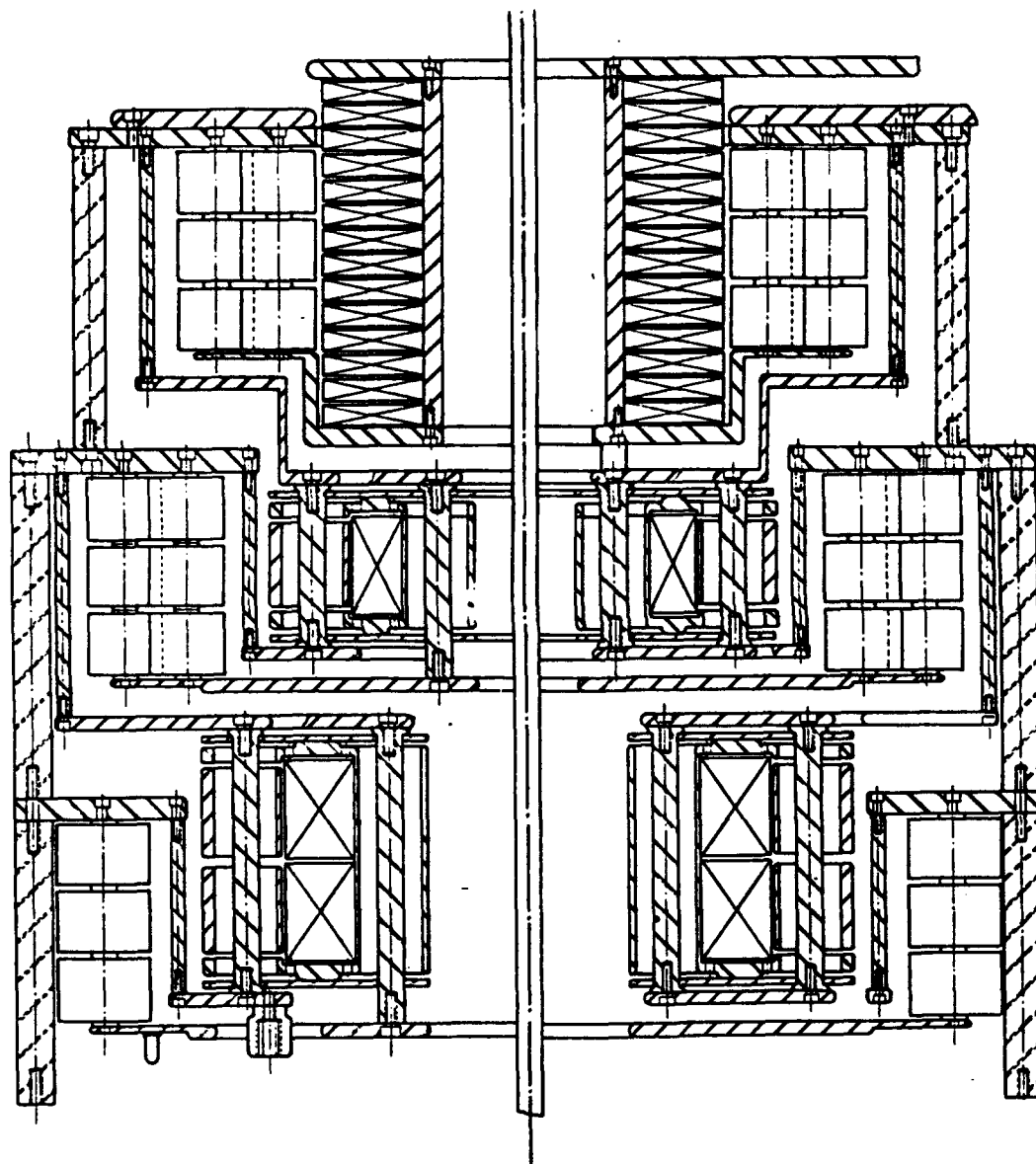


Figure 3.4: SNOMAD-IVB Driver Output Section

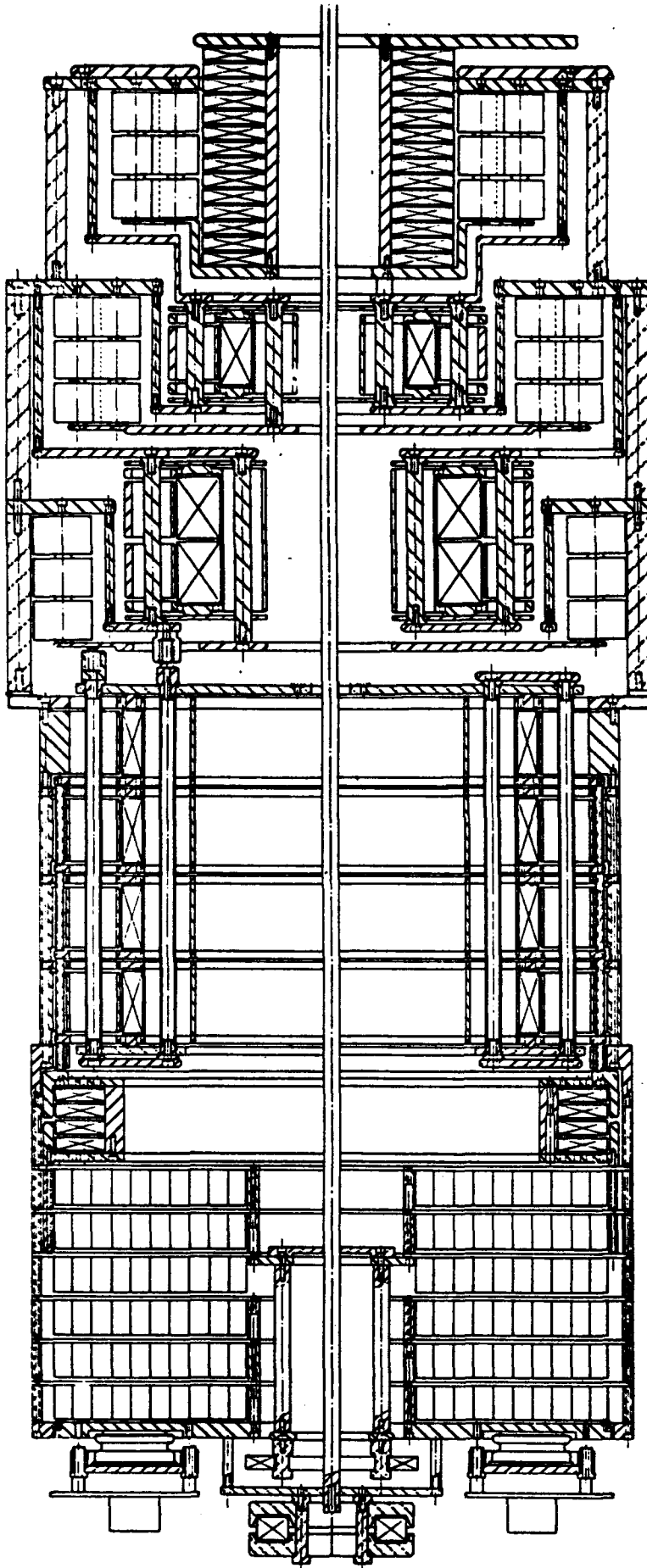


Figure 3.5: SNOMAD-IVB Driver

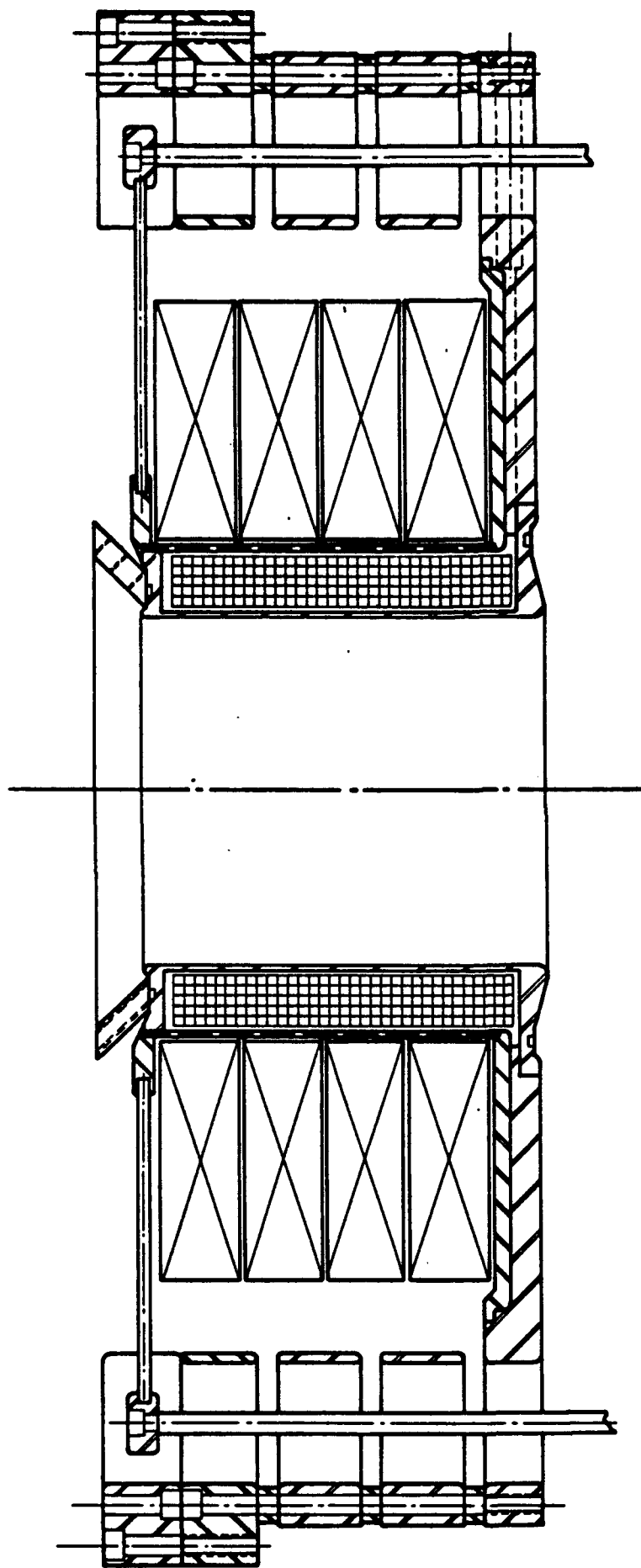


Figure 3.6: SNOMAD-IVB Accelerator Cell



SCIENCE RESEARCH LABORATORY

Figure 3.7: SNOMAD-IVB Accelerator Cells

The SNOMAD-IVB Driver as well as the fourteen SNOMAD-IVB accelerator cells are all conveniently housed in a single aluminum enclosure. Sketches of this enclosure (Figs. 3.8-3.10) show the characteristic dimensions and allow the reader to easily determine the size. The lid of the enclosure has been outfitted with large Lucite windows in order to appease the wishes of the visitors who had a hard time looking through the little portholes in the lid of the SNOMAD-IV module.

The photographs presented in Figs. 3.11-3.13 show the SNOMAD-IVB module in various stages of assembly.

Each accelerator cell is fed by 2 of the 28 independent coaxial transmission lines imbedded into the outer housings. The impedance of these coaxial lines had been chosen so as to provide a good match to the beam load when the accelerator is operated at full voltage and the electron beam current is at 1000 amperes. Presently the SNOMAD-IV injector has been outfitted with a 500 ampere electrode package. The reduced operating current means that the accelerator is better matched to the beam at reduced voltages. This can be seen in Figs. 3.14 and 3.15. Here the SNOMAD-IVB voltage waveform is presented at two different operating levels with a constant beam load of 500 amperes. The waveform corresponding to operation at 0.7 MeV shows a more pleasing profile than the one associated with 1.0 MeV operation.

Aside from the higher operating energy, the operation of the SNOMAD-IVB accelerator modules is virtually identical to that of the SNOMAD-IV injector. With this in mind we will avoid a repetition of the description provided in the previous section and jump to one of the more recent advances incorporated with SNOMAD-IVB. Previously we have always used a simple Command Resonant Charge scheme for supplying the per pulse energy to these accelerator modules. Any variations in the supply voltage appeared as a variation in accelerating potential. We have recently developed a controlled charging scheme based on IGBTs (Insulated Gate Bipolar Transistors).

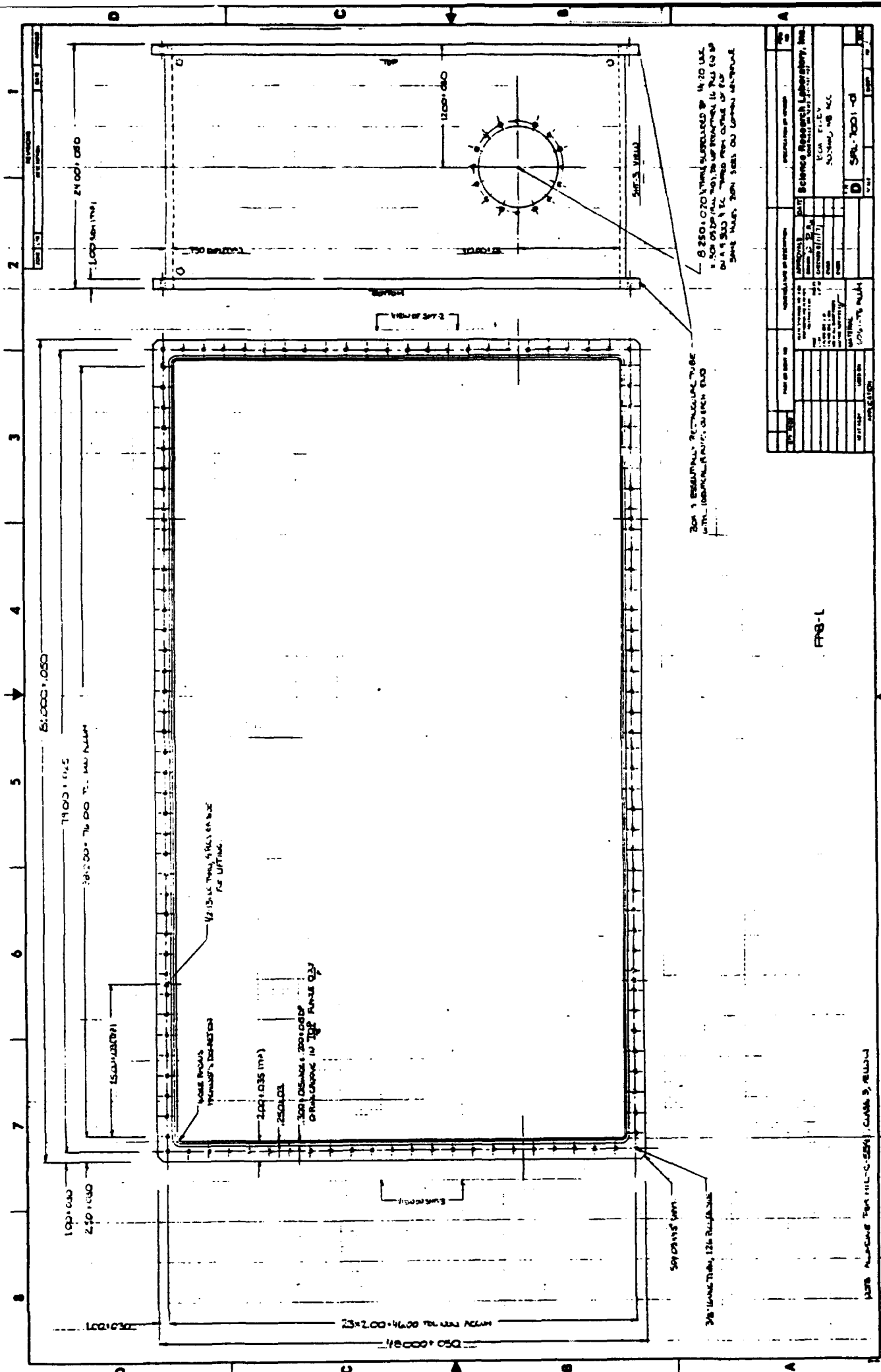
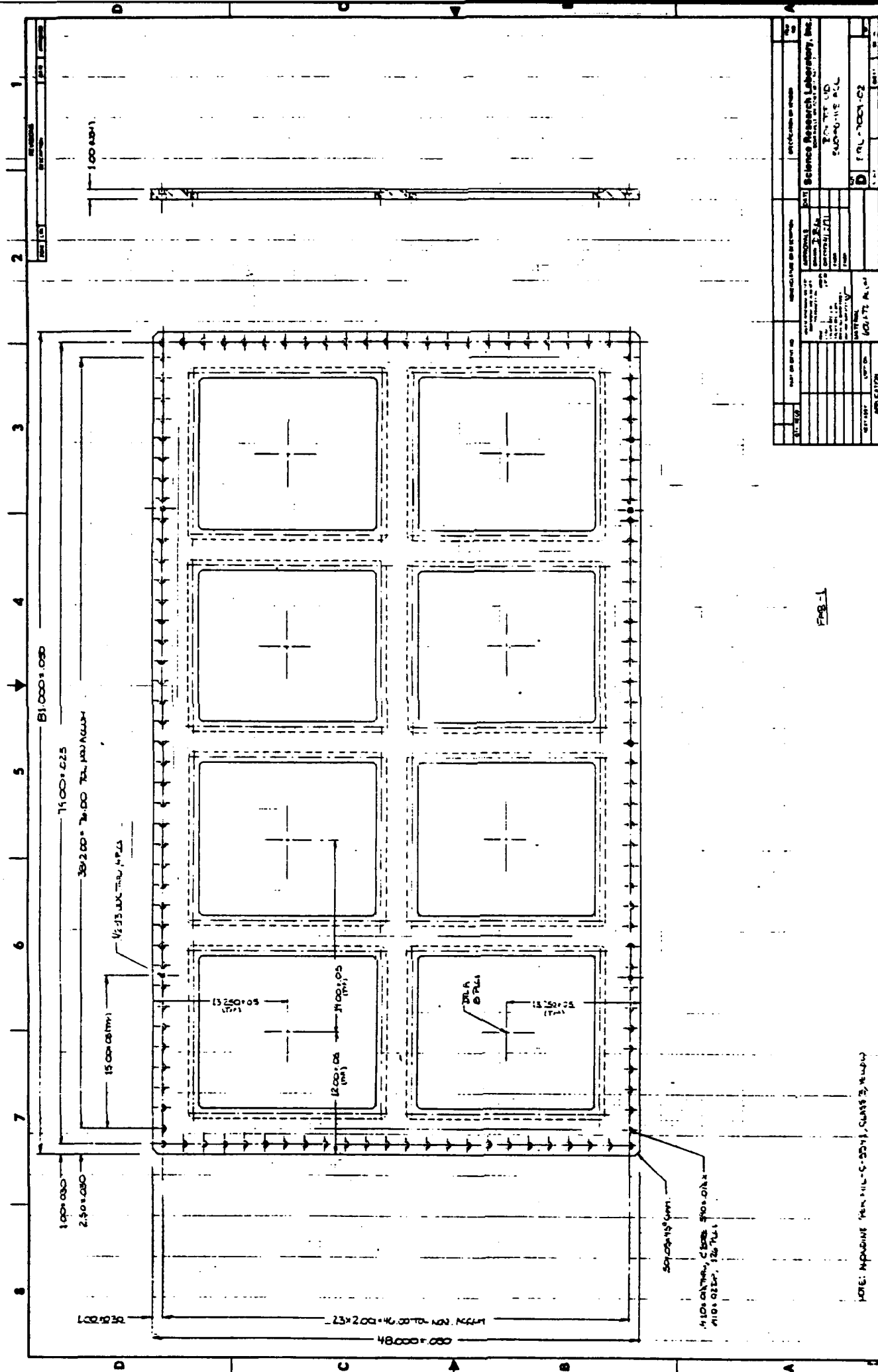


Figure 3.8: SNOMAD-IVB Main Body Enclosure



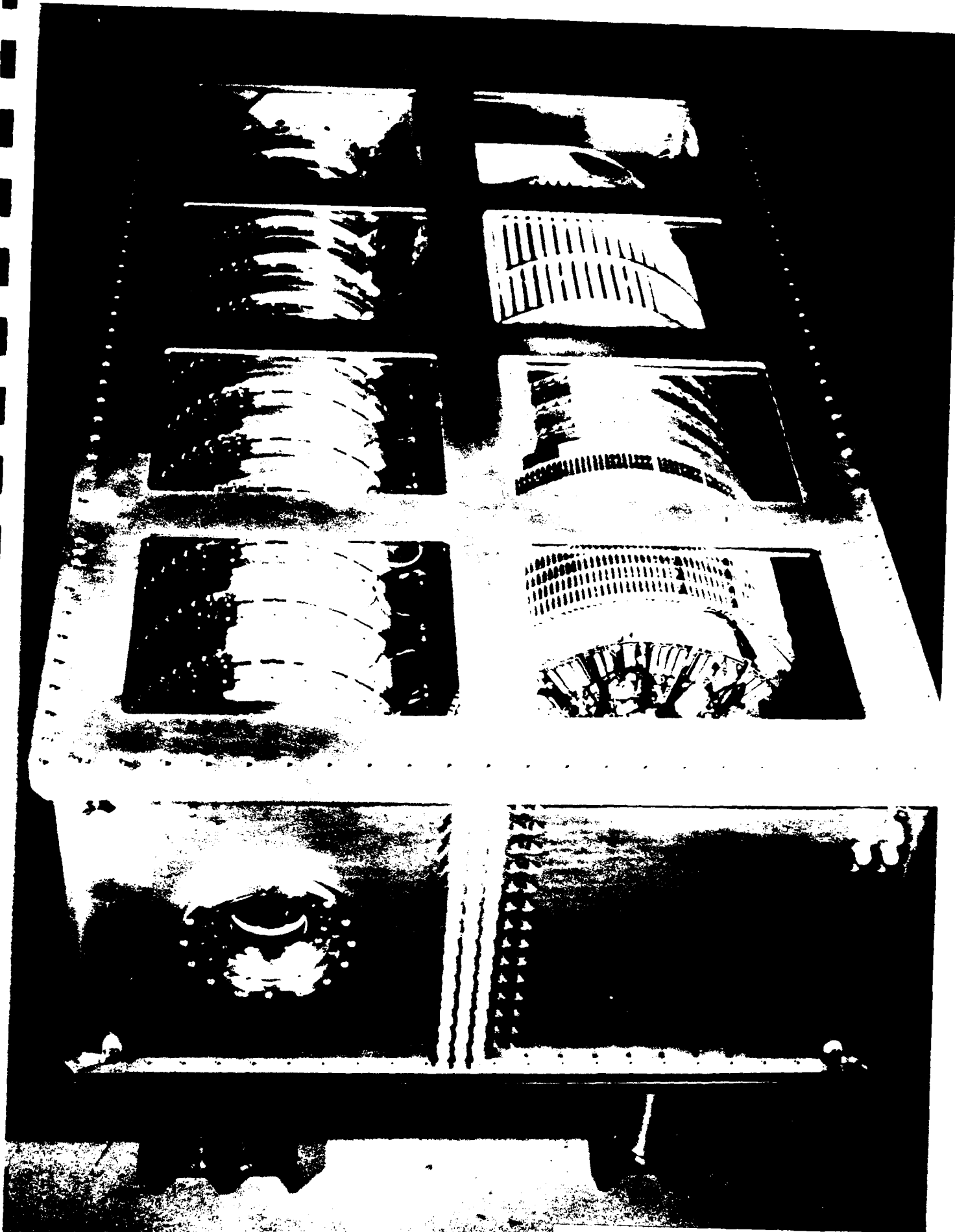


Figure 3.11: Completed SNOMAD-IVB, 1.0 MeV Accelerator Module

SCIENCE RESEARCH LABORATORY

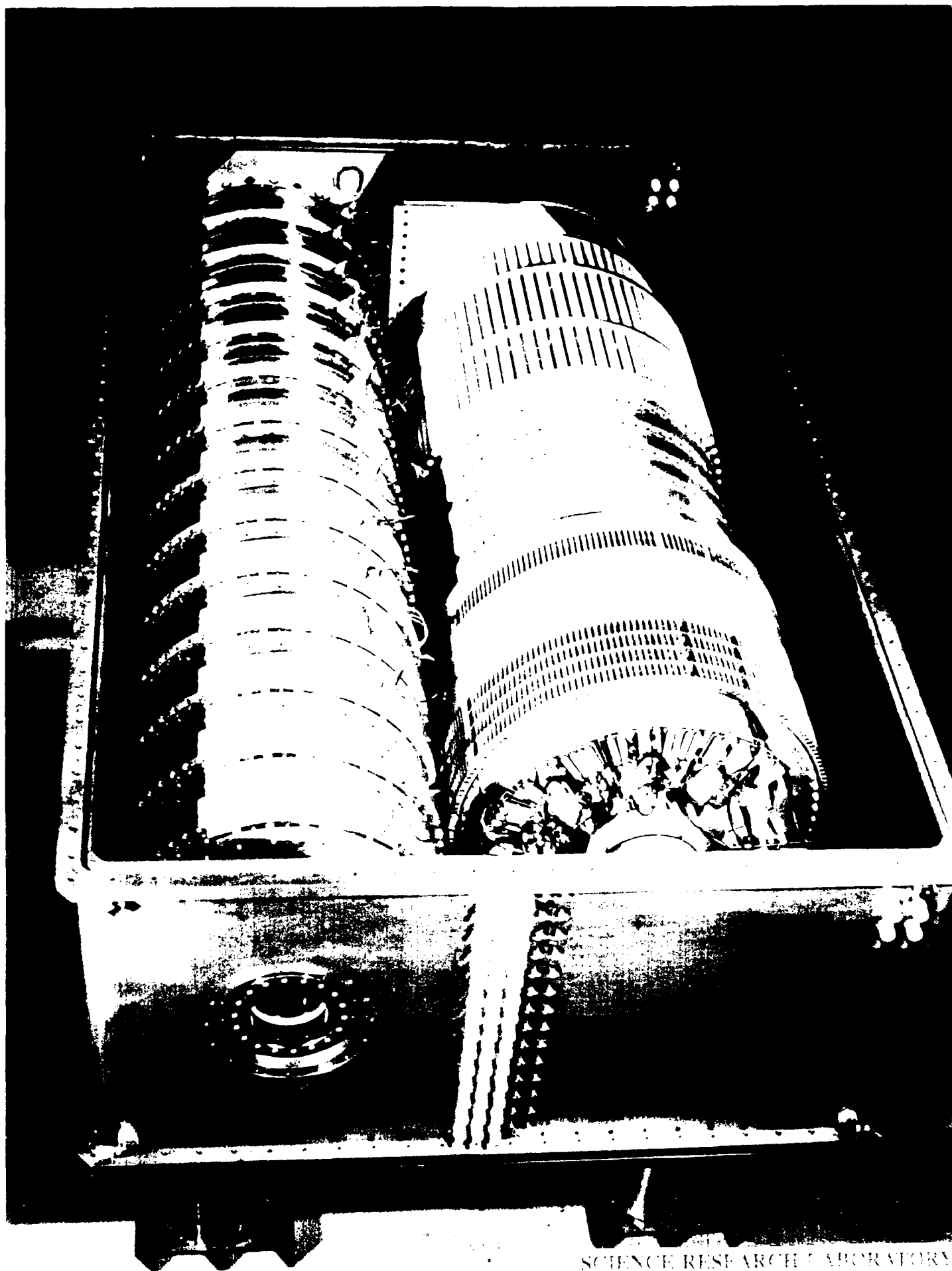
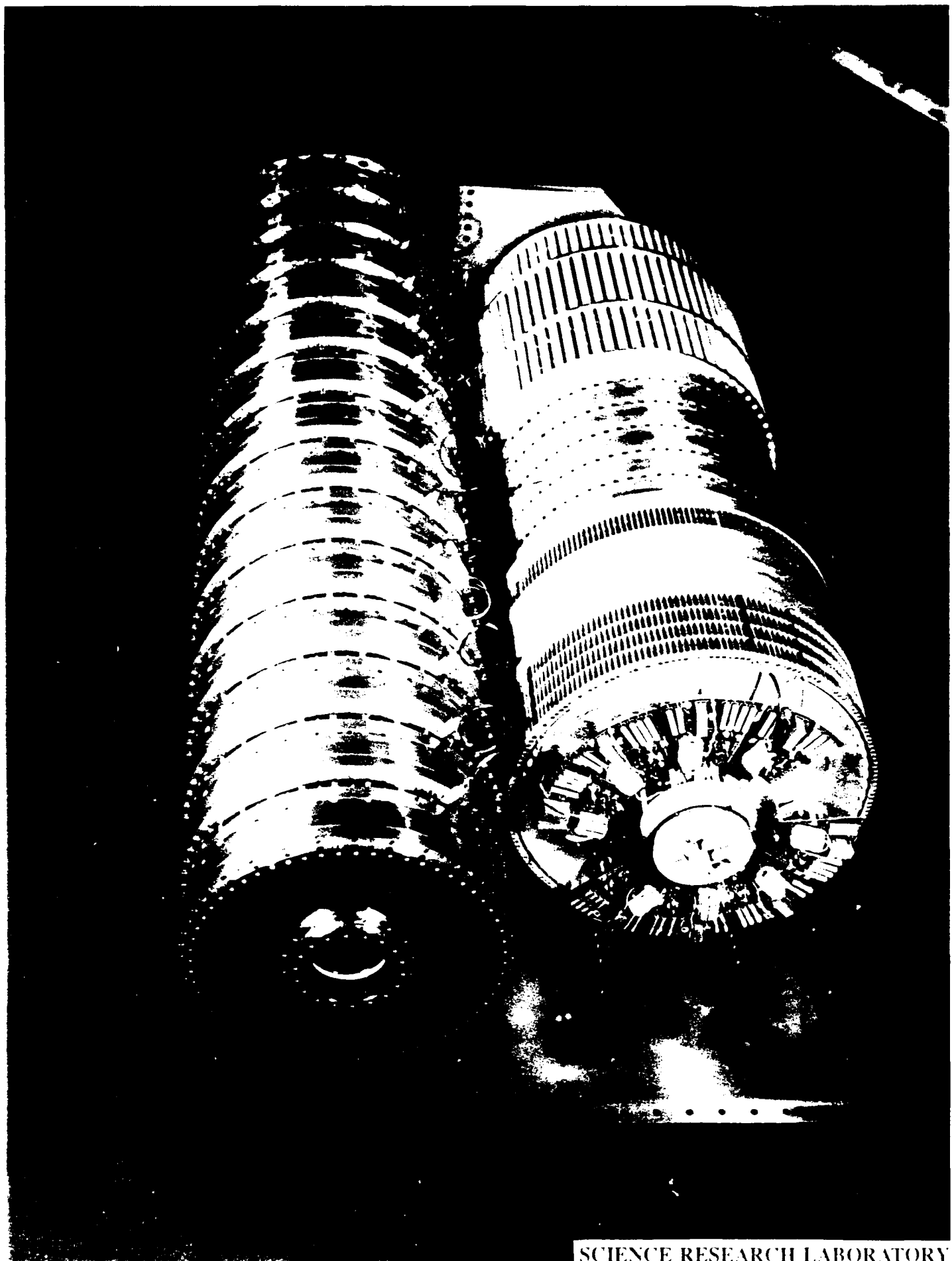


Figure 3.12: SNOMAD-IVB, 1.0 MeV Accelerator Module In Box with Lid Removed.

SCIENCE RESEARCH LABORATORY



SCIENCE RESEARCH LABORATORY

Figure 3.1.14 SMDM-1104 1.0 MeV Accelerator Module Assembly Installation

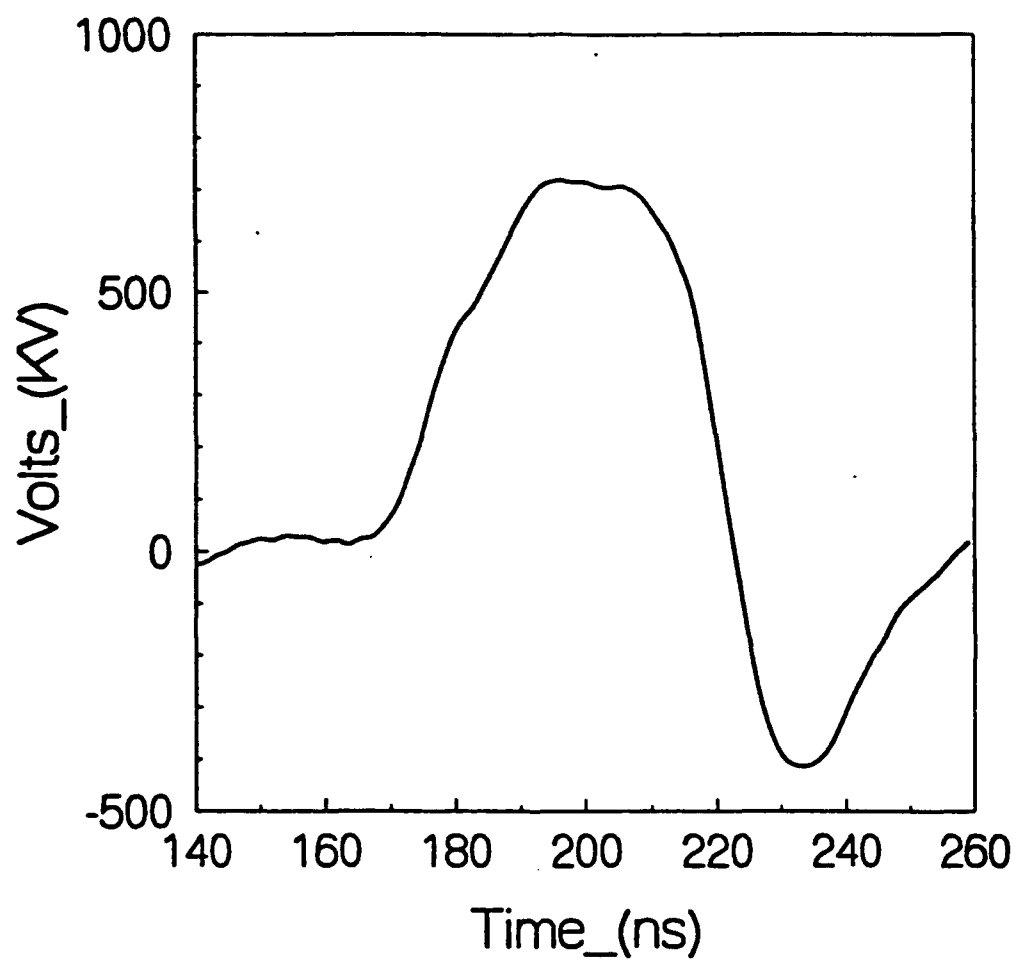


Figure 3.14: SNOMAD-IVB Accelerator Potential – Input Level = 800 Volts

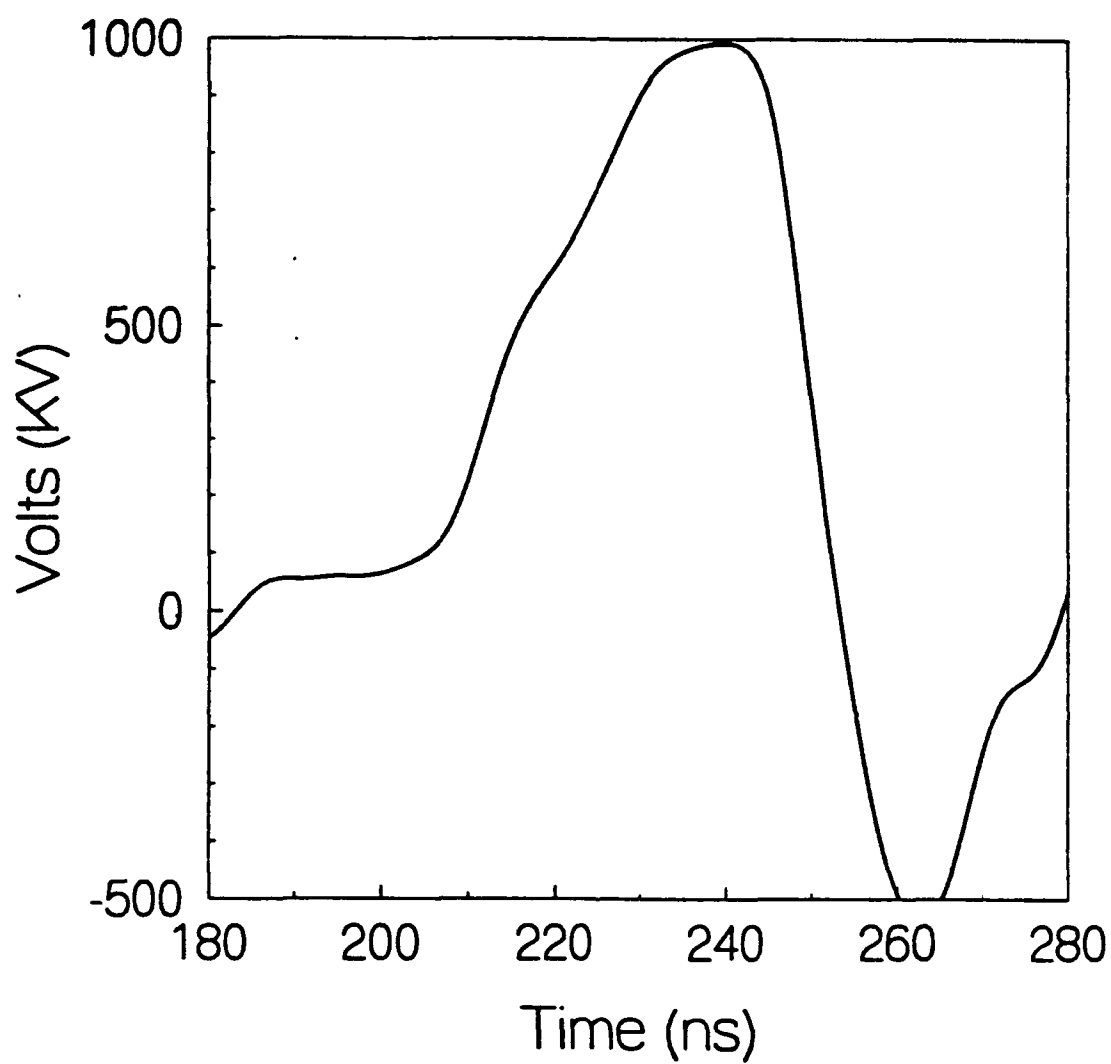


Figure 3.15: SNOMAD-IVB Accelerator Potential – Input Level = 950 Volts

The charge module bears the responsibility of charging the intermediate storage capacitor in SNOMAD-IV accelerator module to a predetermined voltage between output pulses. It was also acquire the reflected energy from the accelerator and add it to the energy required for the next pulse immediately following each discharge cycle.

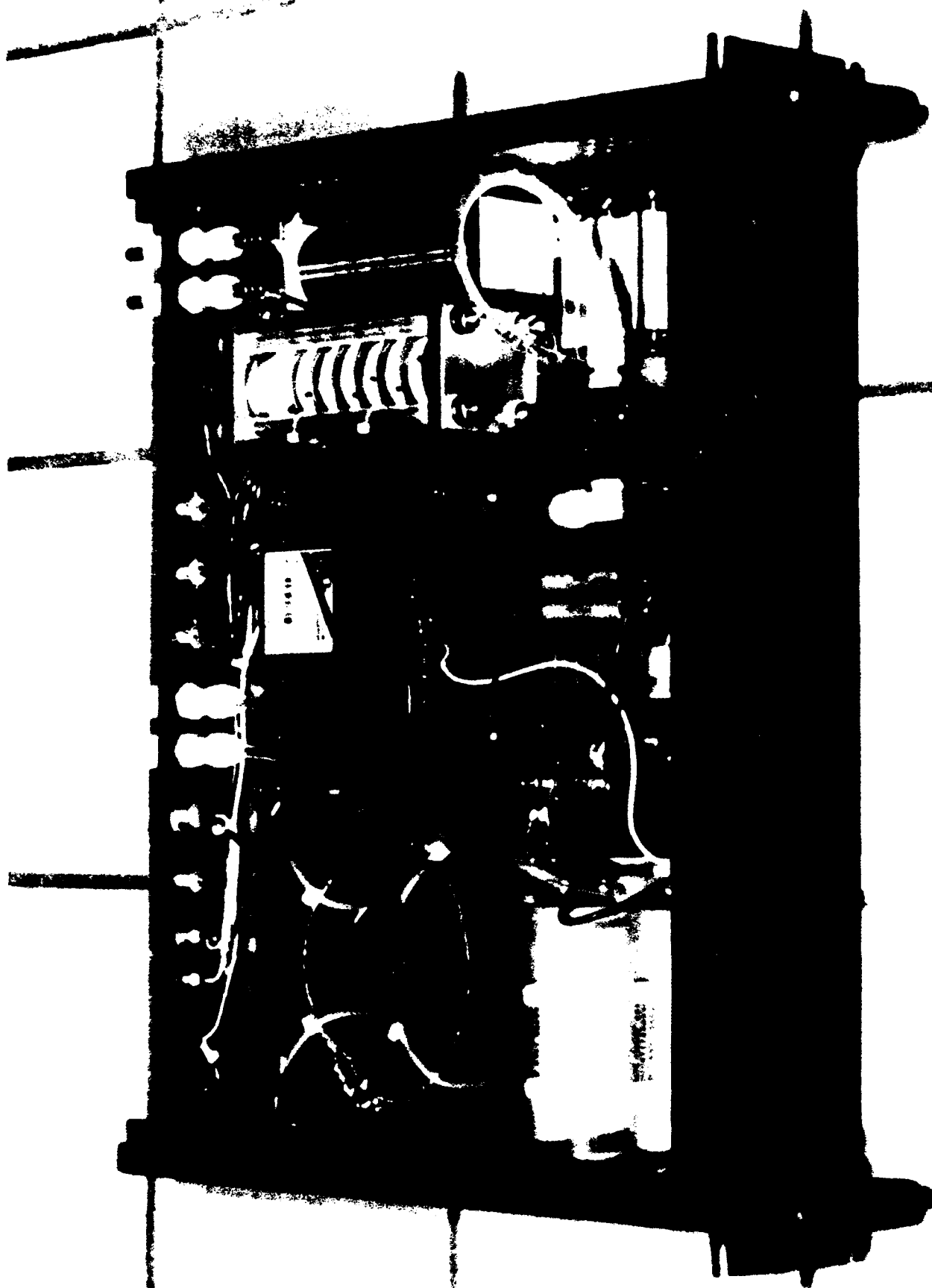
The charge module must provide the same voltage on the intermediate storage capacitor for each succeeding pulse independent of power supply variations and changes in the reflected power. The charging level is controlled by varying the On-state duration of an IGBT. A photograph of the SNOMAD-IVB charge module appears in Fig. 3.16.

On a scale of peak-power-handling, IGBTs fit in the region between MOSFETs and SCRs. MOSFETs and IGBTs can operate as opening switches and SCRs cannot. An SCR can only be brought out of conduction by reducing the conducted current to near zero. IGBTs (MOSFETs) can be brought out of conduction even at the full current rating by simply reducing the voltage to zero on the Gate-Emitter (Gate-Source) connections.

IGBTs differ from MOSFETs in that MOSFETs are a majority carrier device and IGBTs are minority carrier device like all bipolar transistors. Majority carrier devices offer low drive requirements and high switching speeds but high conduction losses and a dangerous positive temperature coefficient of the on-state resistance. That is, as the junction temperature of a majority carrier device rise so does the on-state resistance and therefore the voltage drop increases at a given current as the temperature rises. The hotter the device becomes the more power is dissipated and therefore the hotter it becomes.

IGBTs, like conventional bipolar transistors, are a minority carrier device and exhibit a negative temperature coefficient of on-state resistance. As the junction temperature rises the on-state resistance decreases and therefore the voltage drop decreases at a given current with increasing temperature. The hotter the device becomes the less power is dissipated. Historically, the disadvantage of bipolar transistors has been the enormous drive requirements. IGBTs eliminate the

Figure 3.16: Charge Module



large drive requirement by incorporating a MOSFET driver on the same chip with the bipolar transistor. This MOSFET supplies the drive to the bipolar transistor and we wind up with a device which provides the best of both worlds. The input drive requirements and turn-on characteristics match the superior performance of a MOSFET while the power handling capability models that of a bipolar transistor. Because of this IGBTs are rapidly replacing MOSFET in inverter power supply and many other applications.

When the IGBT is brought out of conduction the charging cycle can not be immediately terminated. There is energy stored in the charging inductor and that energy must go somewhere. The incorporation of a free wheeling diode to ground allows the energy stored in the charge inductor to be transferred into the intermediate storage capacitor after the IGBT conduction cycle is terminated. The final charge voltage will not be simply determined by the intermediate storage capacitor voltage level when the IGBT is brought out of conduction but will also hinge on the current level flowing in the charge inductor at that time.

The SNOMAD-IVB control module must base its decision on two input variables. It must measure the current flowing in the inductor and the voltage appearing on the intermediate storage capacitor. It is simple to show by energy conservation the

$$1/2CV_f^2 = 1/2CV_i^2 + 1/2LI^2$$

and the current can easily be determined by applying the rule that

$$I = CdV/dt .$$

The SNOMAD-IVB control module contains a small analog computer which precisely measures the voltage and its derivative and then makes the determination of the final charge voltage based on the following equation.

$$V_f = \sqrt{V_i^2 + L(dV/dt)^2}$$

The SNOMAD-IVB control module also compares power supply levels and intermediate storage charging levels to predetermined limits and discontinues the driver operation if these

levels fall outset these limits. It also bears responsibility of triggering the SCRs in the SNOMAD-IVB compression module at the appropriate time.

A simplified schematic of the control circuitry found in the SNOMAD-IVB control module can be found in Fig. 3.17 while a photograph of the assembled unit appears in Fig. 3.18.

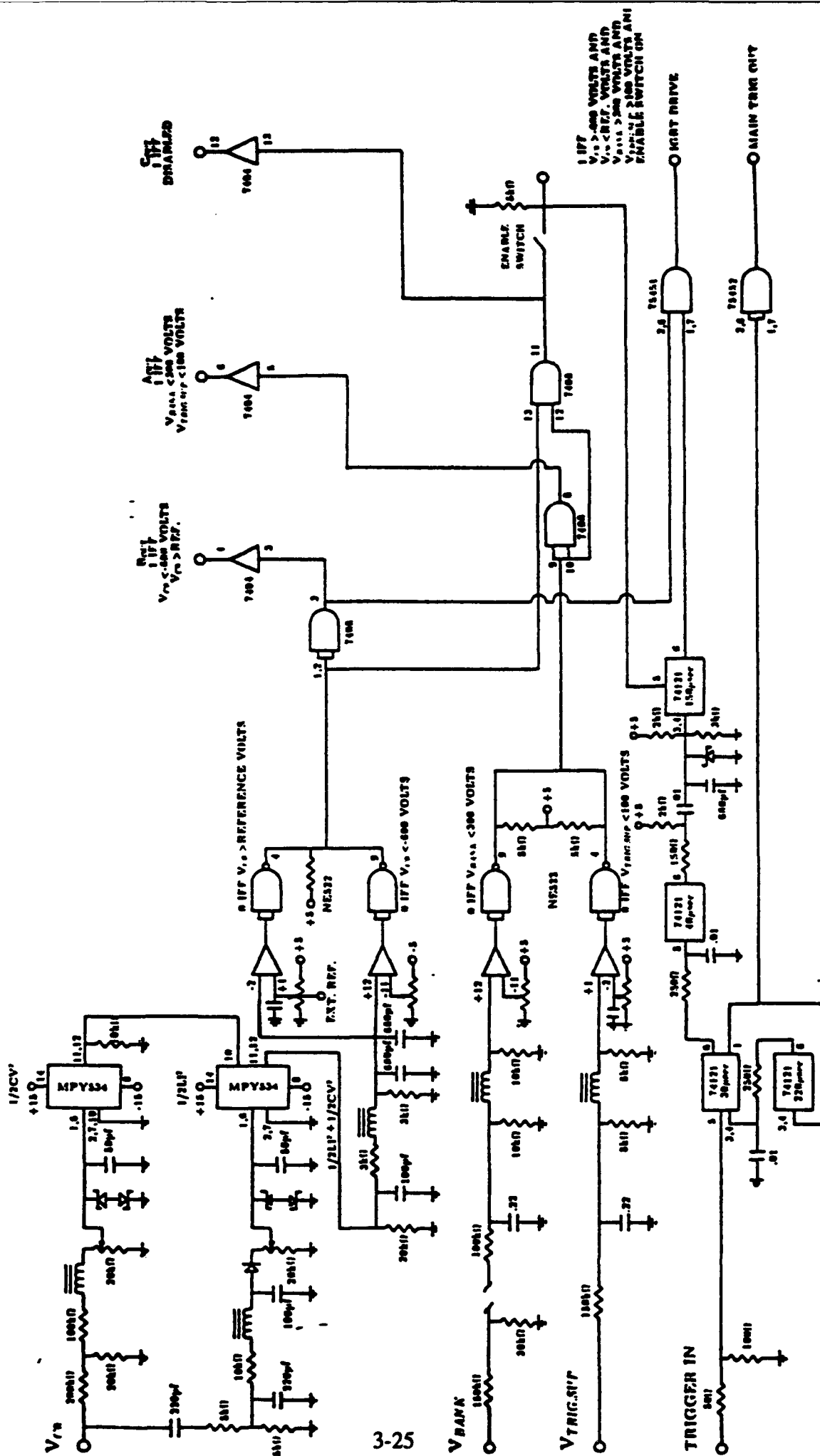
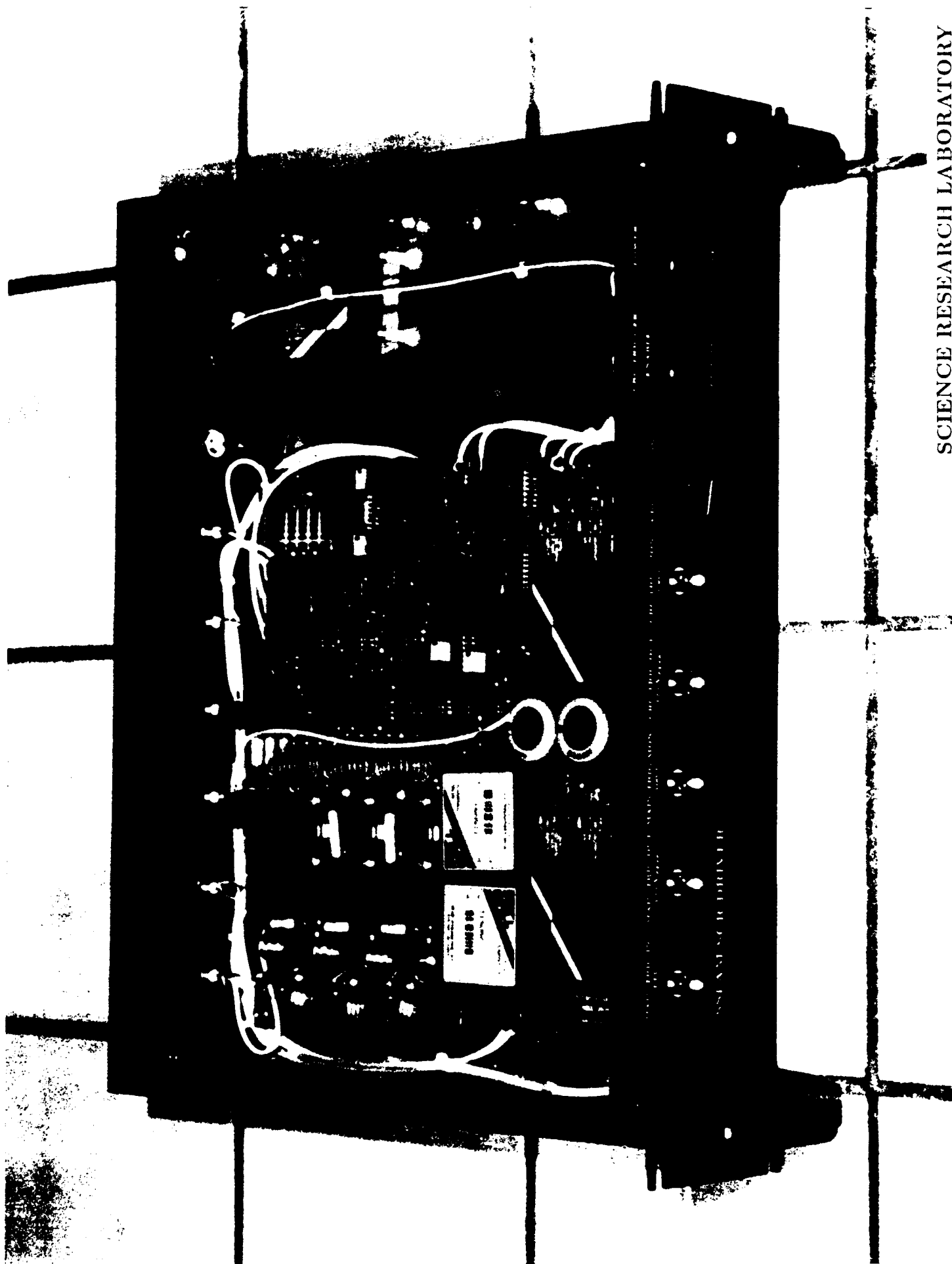


Figure 3.17: SRL-2650B Control Module Logic Circuit

Figure 3.18: Control Module



APPENDIX 1

INDUCTION CELL DESIGN

Both RF and induction linear accelerators are composed of multiple transmission line transformers. While these transmission lines are all driven in parallel as the electron beam passes through them, their voltages add energy to the electron beam in series. Isolation between the transmission lines is achieved by connecting them with a beam pipe which is below cutoff at the operating frequency for all modes except the TEM₀₀. The electron beam forms the inner conductor for this mode. Early Soviet literature describes RF accelerators as air core induction linacs.

If the accelerator is to be efficient, the losses in the transmission line must be negligible in comparison to the energy coupled into the electron beam. In other words, the effective impedance of the transmission line Z_{eff} must be large compared to V_{LINE}/I_{BEAM} . For an RF accelerator, the characteristic line impedance Z_{LINE} may be low, less than 100 ohms, but it is resonant and therefore the effective impedance becomes $Z_{eff} = Z_{LINE} \cdot Q_L/2\pi$ (lowest order mode) where Q_L is the loaded Q of the resonant cavity.

Resonant RF structures also have the advantage that they provide a voltage step up over the drive voltage by a factor.

$$V_{acc} = V_{driver} \cdot Q_L^*/2\pi$$

where:

$$Q_L^{*-1} = Q_u^{-1} + Q_e^{-1} + Q_{beamloading}^{-1}$$

The disadvantage of resonant structures is that a cavity (shorted $\lambda/2$ transmission line) is never simply resonant with a single mode and the wake functions of the electron beam have Fourier components which feed energy into all available modes. Some of these modes are spatially antisymmetric and act to steer the electrons into the beam pipe wall. This sets an upper limit to the total charge which can be accelerated during an RF cavity decay time ($\tau = Q_L/\omega$).

An induction cell is non-resonant and if designed properly stores neither the drive fields nor the wake fields. This dramatically increases the practical operating current but also places constraints on the minimum efficient operating current. If the induction accelerator cell used vacuum as a transmission line medium, the maximum impedance in practice would be less than a few hundred ohms. In operating induction linacs which provide short pulses (~ 50 ns), this line is filled with ferrimagnetic material (ferrite); for long pulses ($50 \text{ nsec} \leq \tau_p \leq 1 \mu\text{sec}$) ferromagnetic materials (e.g. Si-Fe, Metglass, Superpermalloy) are employed. Most high frequency ferrites have dielectric constants of order $\epsilon_r = 10$ and permeabilities of order $\mu_r = 1000$. With ferrite as a medium, the characteristic transmission line impedance is increased over the vacuum value by a factor of $(\mu_r/\epsilon_r)^{1/2} = 10$, yielding effective shunt impedances as high as several thousand ohms. Also the use of ferrite shortens the length of the transmission line required to provide isolation at the desired drive pulse length. Since the group velocity, $v_g = c/(\mu_r\epsilon_r)^{1/2} \simeq c/100$, the transmission line is shorter than the vacuum equivalent by a factor of order 100. Some low frequency RF accelerators employ ferrite solely for this purpose even though the line is resonant.

In summary the use of ferrite in the accelerator cell increases the practical micropulse length by a factor of 100 and the use of a non-resonant structure (induction linac) increases the maximum electron beam current by not storing wake fields. The penalty accompanying these advantages is centered on the fact that induction accelerators are incapable of efficiently accelerating very low current beams.

Design of an induction accelerator cell is relatively straightforward if these basic operating principles are kept in mind. The following rules must be observed. The variables discussed refer to those pictured in Fig. 1.1.

I. The length (h) of the ferrite loaded transmission line is determined by the pulse length and the electrical characteristics of the ferrite.

$$\begin{aligned} 2 \cdot h &\geq \tau_p(\text{pulse length}) \cdot \text{velocity} \\ &= \tau_p \cdot \frac{c}{\sqrt{\epsilon_r/\mu_r}} \approx \frac{\tau_p \cdot c}{100} \end{aligned}$$

In practice, the best performance is achieved by setting $h = \tau_p \cdot c/100$ or in other words setting the line length equal to a single transit time rather than a round trip time. This constraint arises because the ferrite properties are field dependent and the minimum ferrite volume is achieved by designing around a single transit time. Making h longer than a transit time is wasteful as the additional ferrite will never be seen by the pulse. Summarizing, for optimum performance:

$$h \approx \frac{\tau_p \cdot c}{(\epsilon_r/\mu_r)^{1/2}} \approx \frac{\tau_p \cdot c}{100}$$

II. The value for $(R_o - R_i) = \Delta R$ is set by the drive voltage and the maximum flux swing of the ferrite. As the wave generated by the drive pulse is transmitted down the line, the creation of a saturation wave must be avoided or the impedance of the line will appear time dependent.

$$\text{Since : } \int E \cdot dl = -\frac{d}{dt} \int B \cdot da$$

if one assumes μ is constant and $B = \mu H$

then

$$B \leq B_{sat}$$

Two extreme cases may be considered:

A) If $B(r) = \text{const}$, then

$$\text{Voltage} \leq \Delta B_s \cdot \Delta R \cdot v_g$$

B) If $B(r) \propto 1/r$ and if no portion of the line is allowed to saturate

$$B(R_i) \leq B_{sat}$$

and

$$\text{Voltage} \leq \Delta B_s \cdot v_g \cdot R_i \cdot \ln(R_o/R_i)$$

In practice μ is not a constant and is dependent on both dB/dt and H . This causes the real requirement to lie somewhere in between cases (A) and (B) so that $B(r) \propto r^{-\alpha}$, $0 \leq \alpha \leq 1$.

III. Beam Pipe Radius - R_{PIPE}

Three competing requirements determine the optimum value for R_{PIPE} :

(A) The growth of the beam break-up instability (BBI) is exponentially dependent on R_{PIPE}^{-2} .
(i.e. $A = A_o \exp(I_{BEAM} \cdot V_{acc} \cdot \text{Const.}/B_{kg} R_{PIPE}^2 \cdot E_{gap}))$

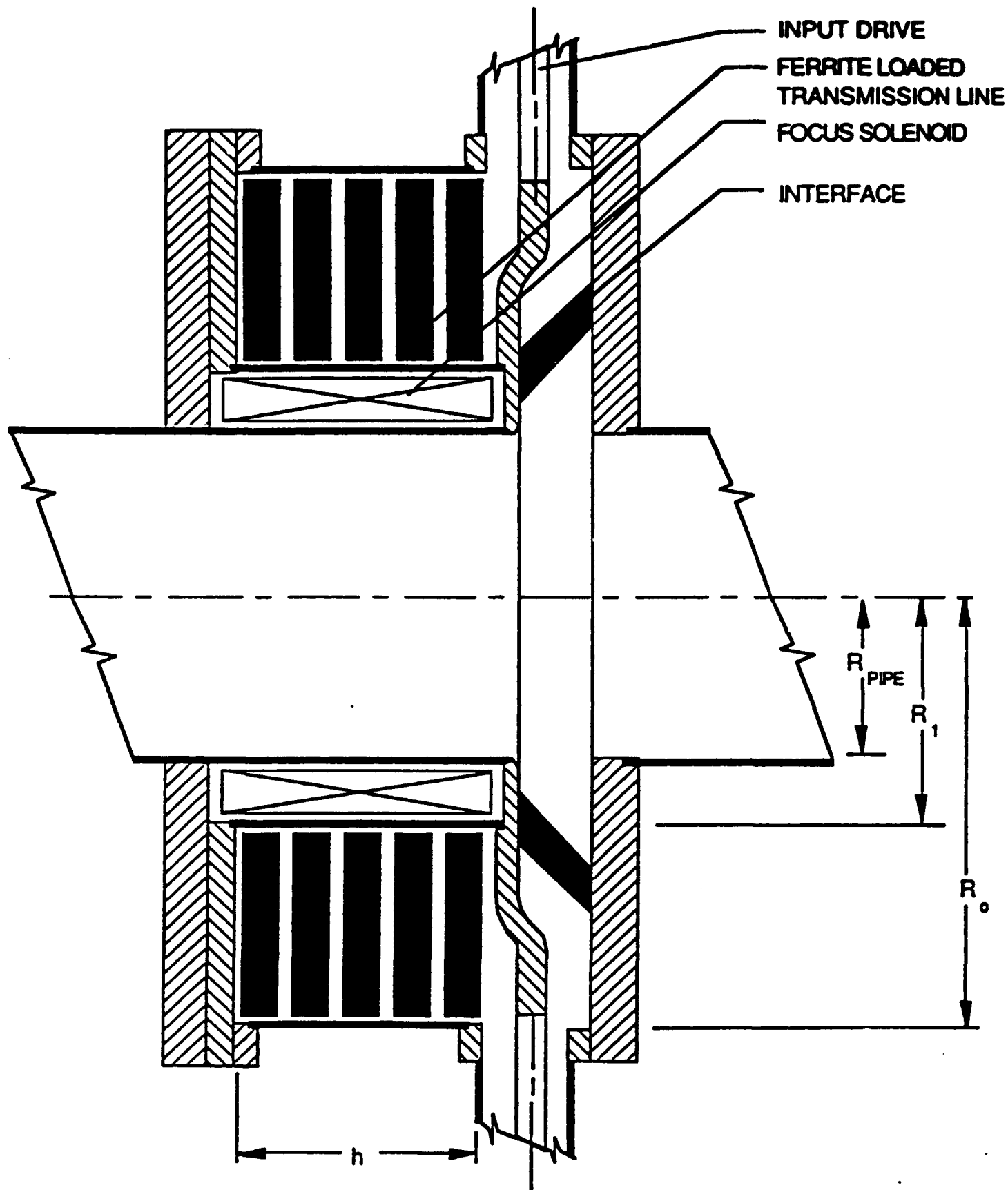


Figure 1.1: Simplified cross section of an induction accelerator cell

(B) The impedance of the ferrite loaded transmission line decreases approximately linearly with R_{PIPE}^{-1} .

(C) The weight of the accelerator increases as the square of R_{PIPE} .

In short the losses are increasing with R_{PIPE} linearly while the growth of BBI is decreasing exponentially as R_{PIPE}^2 . It is essential in these designs to fully understand the dependence of the growth rate of the BBI on pipe diameter. In past designs, the pipe diameter has been undersized and has resulted in designs which were not compatible with full current operation. This applies to both RF and induction linear accelerators.

1.1 Operating Voltage and Gradient

It has been shown above that the length of the accelerator is set by the choice of core material and pulse length. In addition the beam pipe radius is determined primarily by BBI considerations. It was also shown that the value of $\ln R_o/R_i$ was determined by the core material and the individual gap drive voltage. Indeed once the drive voltage, current and pulse length are selected, then limiting values for the accelerator cell are uniquely determined.

The operating current, total accelerator voltage and pulse length are set by the application. This leaves the individual gap voltage the only unspecified parameter. We have shown above that the accelerator gradient is linearly proportional to the individual gap voltage. What we will show below is that while the coupling coefficient (the fraction of energy deposited in the beam versus the energy lost in the accelerator cores) is independent of gradient, the accelerator weight and cost becomes exponentially dependent on the gradient in the limit of large gradients. We will also show that for constant BBI gain, accelerator weight and cost in the limit becomes exponentially dependent on $\sqrt{I_{beam}}$.

The equivalent circuit for an induction linac is the same as that for all transformers.

One must bear in mind that while the number of secondary turns N_{se} is unity, the number of primary turns is fractional given by

$$N_{prim} = \frac{1}{\# \text{ Acc cells}}$$

$$Z_{out} = \frac{V_{acc}}{I_{beam}}$$

while Z_{in} the input drive impedance to the individual cells is given by

$$Z_{in} = \frac{V_{gap}}{I_{percell}}$$

The shunt impedance to ground is determined by the accelerator cell geometry and choice of core material. It is given by

$$Z_{shunt} = \frac{1}{2\pi} \sqrt{\frac{\mu}{\epsilon}} \ln R_o/R_i$$

Under the assumption that no ferrite is allowed to exceed a flux swing of ΔB_s and $B(r) \propto 1/r$, we saw that the accelerator gap voltage was given by

$$V_{gap} = \Delta B_s \cdot v_g \cdot R_i \ln R_o/R_i$$

where $v_g = c/(\epsilon_r \mu_r)^{1/2}$ is the wave velocity in the ferrite, $R_i(R_o)$ the inner (outer) radius of the ferrite core. The accelerator shunt impedance is then simply determined by the characteristic impedance of this ferrite loaded transmission line

$$\begin{aligned} Z_{SHUNT} = Z_{LINE} &= \frac{1}{2\pi} \sqrt{\frac{\mu}{\epsilon}} \ln \left(\frac{R_o}{R_i} \right) = \frac{1}{2\pi} \sqrt{\frac{\mu}{\epsilon}} \frac{V_{gap}}{v_g \cdot \Delta B_s \cdot R_i} \\ &= \frac{1}{2\pi} \mu \cdot \frac{V_{gap}}{\Delta B_s \cdot R_i} \end{aligned}$$

If the electron beam impedance is defined as

$$Z_{beam} = \frac{V_{gap}}{I_{BEAM}}$$

then the coupling coefficient (= energy coupled to the beam/the total energy incident on the accelerator cell) is given by

$$K = \frac{Z_{SHUNT}}{Z_{BEAM} + Z_{SHUNT}} = \frac{1}{\frac{2\pi \Delta B_s R_i}{\mu I_{BEAM}} + 1}$$

A plot of coupling coefficient versus ferrite core inner radius for several different beam currents appears in Fig. 1.2. Here we have assumed a ferrite with a $\mu_r = 400$ and $\epsilon_r = 12$.

It should be noted that the coupling coefficient is independent of accelerator gradient but increases with increasing current and decreasing ferrite core inner radius.

The cost and weight of the accelerator structure is to first order linearly dependent on the core column.

$$\text{Core Volume} = \# \text{cells} \cdot \text{cell core length} \cdot \pi (R_o^2 - R_i^2) \quad (1.1)$$

and

$$V_{gap} = \frac{V_{acc}}{\# \text{cells}} = \Delta B_s \cdot v_g \cdot R_i \ln (R_o/R_i) \quad (1.2)$$

if $B \propto 1/r$ and no ferrite is allowed to exceed a flux excursion of ΔB_s . We can then rewrite Eq. (1) as

$$\text{Core Volume} = \frac{V_{acc}}{V_{gap}} \cdot v_g \cdot \tau_{pulse} \cdot \pi R_i^2 \exp \left(\frac{V_{gap} \cdot 2}{\Delta B_s \cdot v_g \cdot R_i} \right)^{-1} \quad (1.3)$$

where τ_{pulse} is the pulse length. It should be noted that the minimum core volume (d core volume/d $V_{gap} = 0$) is always achieved when $V_{gap} = 0$. Also for $2 \cdot V_{gap} / \Delta B_s \cdot v_g \cdot R_i < 1$, core volume is approximately independent of V_{gap} while for

$$\frac{2V_{gap}}{\Delta B_s \cdot v_g \cdot R_i} \gg 1$$

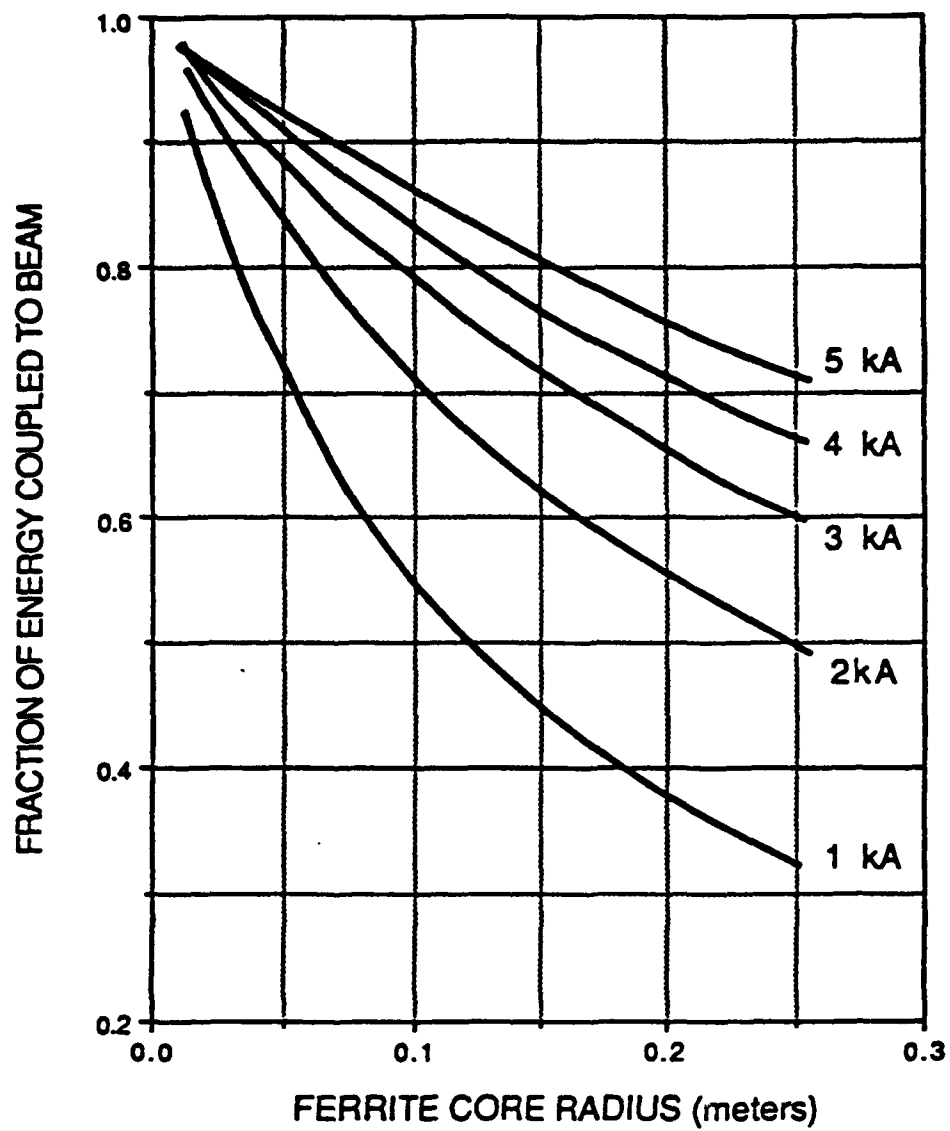


Figure 1.2: Coupling coefficient

core volume becomes exponentially dependent on V_{gap} .

This becomes obvious upon careful examination of Fig. 1.3. Here we have assumed $\mu_r = 400$, $\epsilon_r = 12$, and $\tau_{pulse} = 50$ nsec. Referring to Eq. (3), it also appears that core volume is linearly dependent on τ_{pulse} . The dependency on $v_g = c/(\mu_r \cdot \epsilon_r)^{1/2}$ is somewhat more subtle. For small values of V_{gap}/R_i the core volume varies as $1/\mu_r^{1/2}$ but as V_{gap}/R_i becomes large, core volume becomes exponentially dependent on $\mu_r^{1/2}$.

It is also obvious from Fig. 1.3 that the inner ferrite core radius dramatically impacts the accelerator weight at a given gradient. Referring to Fig. 1.2 the efficiency degrades rapidly as the ferrite inner radius is increased. This inner radius is determined primarily by the beam pipe radius and the thickness of the focusing solenoid. Arbitrary reduction of these parameters independently of the current will result in the onset of the Beam Break-up Instability which will drive the accelerator beam current into the walls.

The amplitude of the BBI oscillation throughout the accelerator is given by:

$$A = A_0 \exp \left(\frac{\text{const.} N I Z_{\perp} \omega}{B_{kg}} \right)$$

where

$$K = 1.16 \cdot 10^{-13} \text{ kg} \cdot \text{sec}/(\text{kamp} \cdot \text{ohm})$$

N = Number of accelerator gaps

ω = Mode frequency

I = Accelerator current

B_{kg} = Focusing field

Substituting

$$N Z_{\perp} = N(Z_{\perp}/Q) \cdot Q = \frac{\text{const.}_1 \cdot Q \cdot V_{acc}}{E_{gap} \cdot R_{pipe}}$$

where

V_{acc} = Accelerator voltage

E_{gap} = Accelerator gap electric field stress

R_{pipe} = Beam pipe radius provides the following equation for the BBI amplitude.

$$A = A_0 \exp \left(\text{const.} \cdot \frac{I \cdot V_{acc}}{B_{kg} R_{pipe}^2 \cdot E_{gap}} \right)$$

Therefore, the BBI amplitude depends exponentially on the inverse of the accelerator gap stress and the beam pipe radius squared.

In order to minimize both the beam pipe radius and the solenoid thickness (B_z) while holding BBI gain constant at a given current and accelerating potential, the accelerator gap stress must

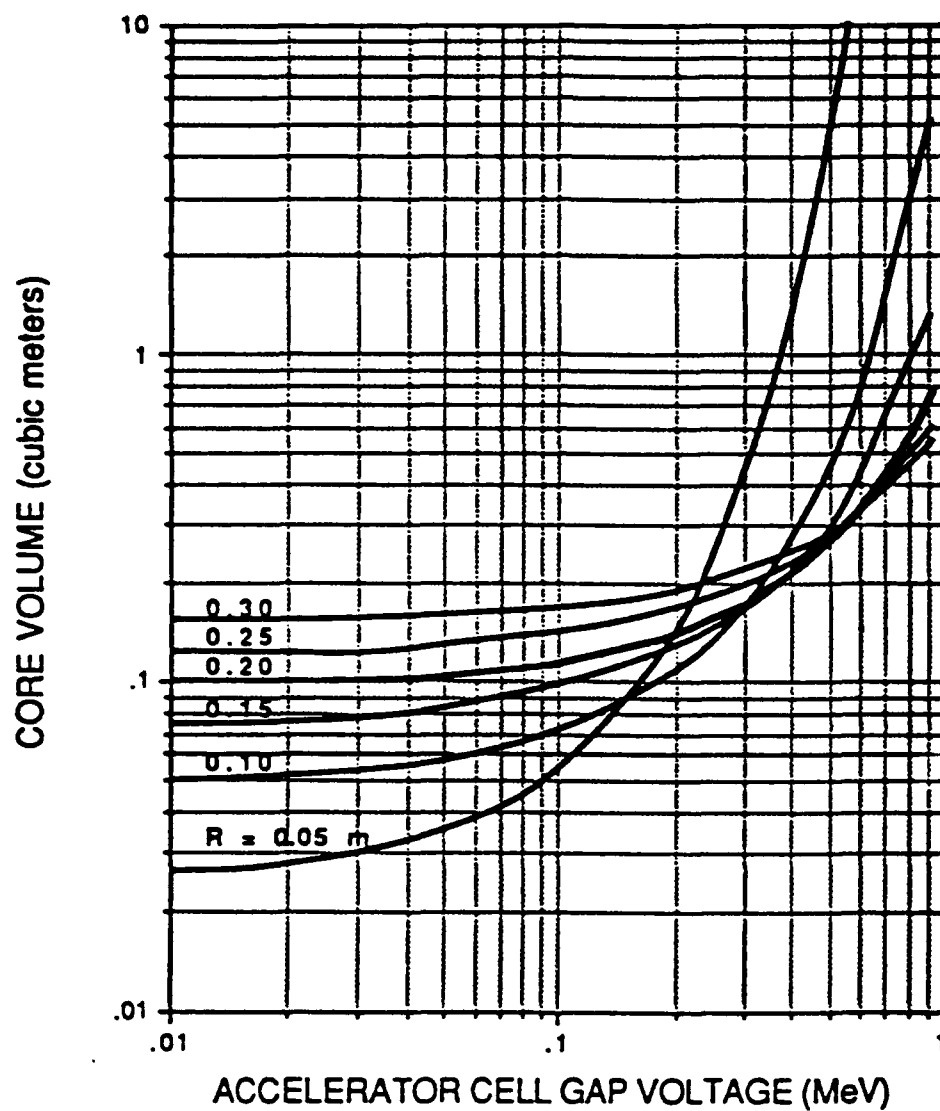


Figure 1.3: Accelerator core volume per megavolt

be increased to as high a value as practicable. Unfortunately at the high duty factors required for most of these applications, exceeding the threshold where field emission in the gap occurs is not allowed. Understanding this limit is essential to optimizing the design.

The core volume become exponentially dependant on the inverse of ΔB_s . This makes things somewhat complicated as the individual gap voltages and beam pipe inner radius must be determined before the optimum material can be selected. At this point we will attempt to document the ferrite properties and the optimum choice will be left for the engineer responsible for a specific accelerator cell design.

APPENDIX 2

NONLINEAR MAGNETIC MATERIAL SELECTION

It is important to understand when it is advantageous to use ferrite rather than metglass or Ni-Fe tapes. In this section we will compare the attributes of ferrites with those of metglass and Ni-Fe tapes. The first stage compression reactor step-up transformer and (sometimes) the second stage compression reactor are designed around metglass cores. This is the last stage in the compression chain where metglass can be employed if efficiency is an important consideration. Metglass is composed of a mixture of silicon and iron which is mixed while liquefied and then rapidly quenched so that it remains amorphous. The resistivity of this alloy is three times that of most ferro-magnetic materials. However, at saturation times much less than 10^{-6} seconds, the losses begin to scale inversely with the saturation time as eddy currents become the dominant loss mechanism (see Fig. 2.1).

Metglass, a mixture of silicon and steel possesses the magnetic properties of steel (i.e. $\Delta B \sim 36$ kg, $H_c \sim 0.05$ Oe, $\mu_r \approx 10,000$) but affords much higher resistivities ($\rho \sim 130 \mu\Omega\text{-cm}$) because of its glass-containing atomic structure. Unfortunately it has a rough surface texture resulting in inherent packing factors of only 0.8 and the addition of interlaminar insulation further reduces this to ~ 0.7 in a wound core. Interlaminar insulation can be avoided if the material can be vapor deposited with a very thin layer of MgO or SiO_2 . The inherent 0.8 packing factor associated with roughness can be improved upon by hot rolling the metglass. These techniques are aimed at the objective of achieving an overall packing factor of 0.8.

Even with a packing factor of only 0.7 (compared to almost unity with ferrite), when the inherent $\Delta B_s \leq 3.1$ Tesla of metglass is compared to $\Delta B_s \leq 0.65$ Tesla of $\text{Zn}_{0.60}\text{Ni}_{0.40}$ ferrite (core volume depends inversely on ΔB_s^2), metglass is preferred when eddy current losses are not a problem. As the saturation times get shorter and eddy current losses increase, removing the waste heat from the interlaminar core structure becomes very difficult. Manganese zinc ferrites would seem a logical choice to span the gap between metglass and $\text{Zn}_{0.60}\text{Ni}_{0.40}$ ferrite, but geometric resonances encountered in the large cores required at this pulse energy eliminate it from consideration. Other iron alloys such as 50-50 Ni-Fe have been tested but suffer from the same heat removal problems as metglass. The higher conductivity of these alloys requires them to be thinner and this results in a greater expense and a lower net packing factor. It is hoped that advances in coating technology will improve the situation in the future.

The time dependent losses in ferro-magnetic ribbons are typically explained in terms of a saturation wave which encircles the tape and proceeds toward the center at a rate which is linearly dependent on the applied voltage. Ignoring the fact that domain wall locations are initially pinned to impurity sites, the H-field required to change the state of magnetization of a tape is given by

$$H_a = H_c + \left(\frac{d^2}{4\rho} \right) \left(\frac{\Delta B}{2B_s} \right) \left(\frac{dB}{dt} \right)$$

where B_s is the saturation induction, H_c is the DC anisotropy coercive field, d is the sample thickness and ρ is the resistivity. The energy density deposited in the tape during saturation is given by

$$E_L = H_c \Delta B + \left(\frac{d^2}{8\rho} \right) \left(\frac{\Delta B^2}{2B_s} \right) \left(\frac{dB}{dt} \right)$$

This theory assumes the material is completely isotropic and possesses no preferred domain geometry. This is certainly not true and experimental measurements of time dependent losses conducted

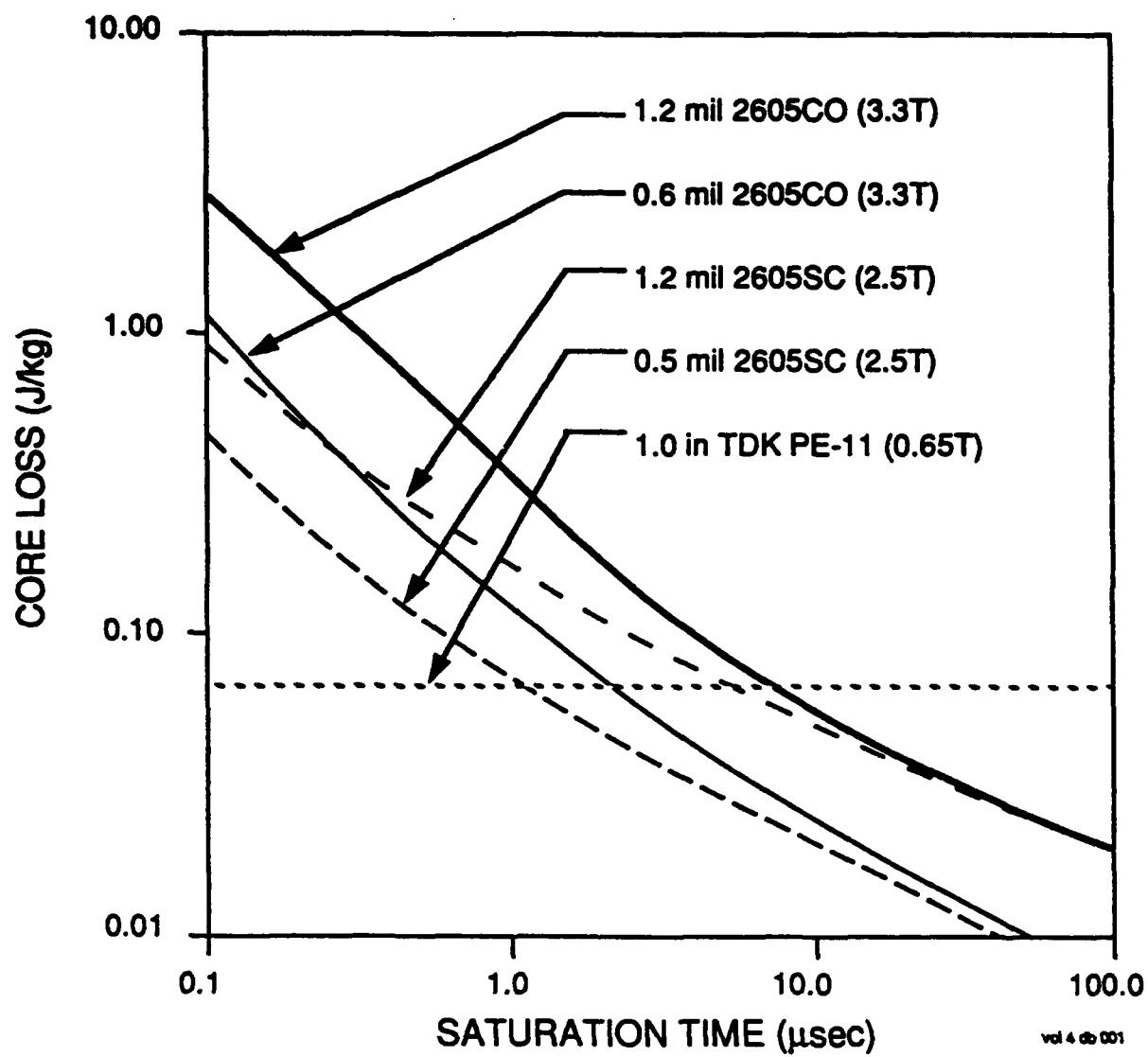


Figure 2.1: Estimated core loss versus saturation time

by Dr. Carl Smith at Allied Chemical Research Laboratories indicate a much more complicated behavior. This data, summarized in Fig. 2.1, is further documented by graphs prepared by Dr. Carl Smith which appear in Fig. 2.2.

The chart of losses versus saturation time in Fig. 2.1 shows clearly that once normalized by $(1/\Delta B_s)^2$, metglass is the optimum material down to 100 nsec saturation times and then ferrite takes over.

In the past ferrite was sometimes used where metglass was the best material choice. The cause of this apparent inconsistency was centered in the fact that techniques for adequately cooling tape wound cores had not been developed. This is no longer true and metglass is the optimum material choice for nonlinear magnetic compressor cores operating with ≥ 100 nsec saturation times.

The effect of saturation time on metglass core loss is further documented in Figs. 2.3-2.8. Here the B-H curves are presented for metglass cores of various compositions driven from $-B_s$ to $+B_s$ over a range of time intervals. The saturation time was varied from $5.0\mu\text{sec}$ to $0.25\mu\text{sec}$ for these measurements and the effect on the B-H curve is quite noticeable. It should be remembered that the energy lost per unit volume of core material is directly proportional to the area under the curve. All samples were wound from unannealed metglass tapes with thicknesses in the range of 0.8 to 1.0 mils.

The B-H curves for both 1.2 mil and 0.6 mil thick Ni-Fe tapes are presented in Figs. 2.9 & 2.10. Ni-Fe tapes are more expensive than Metglass tapes but they are much more consistent and particularly in the case of 0.6 mil thick tapes offer a reasonable alternative. Ni-Fe tapes are rolled and annealed providing a much more uniform cross-section.

Ferromagnetic Resonance

The concept of ferromagnetic resonance can best be understood by simple analogy to the precessional motion of a spinning top. The spinning electron may be treated as an electrically-charged spinning mass. The magnetic forces acting on the spinning electron are similar to the gravitational forces acting on a spinning top. These magnetic forces acting on the electron in a ferromagnetic material are derived from two primary sources. These two components consist of the internal magnetic fields generated by the many individual magnetic dipoles which make up the domains and secondly the external forces which when applied perturb the alignment of these dipoles. When the external fields are applied perpendicular to the internal fields they exert a thrust or torque on the spinning electrons.

In the case of a spinning top (Fig. 2.11) application of a force perpendicular to the axis of spin will initiate precession. The precession frequency ω_0 depends on the angular momentum of the top and the gravitational force Mg acting on the center of mass of the top. The gravitational torque is

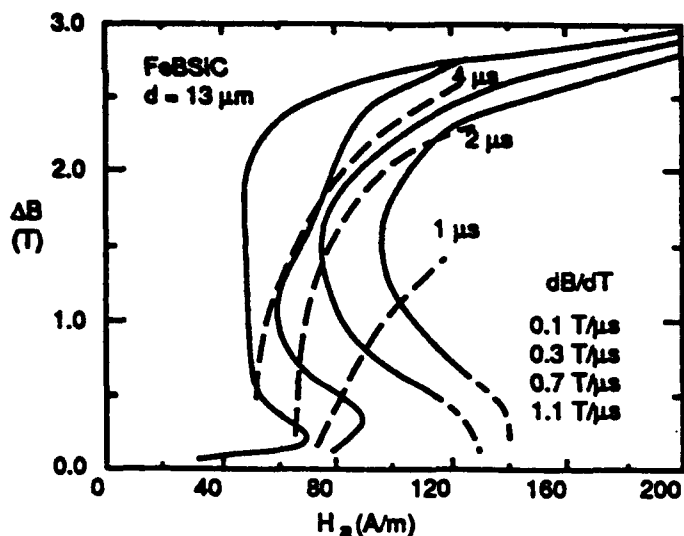
$$T = MgL \sin \theta$$

where θ is the angle of inclination and L is the distance from the pivot point to the center of mass. The angular momentum vector will maintain a constant angle θ with the vertical and the top will precess about the vertical axis with an angular velocity

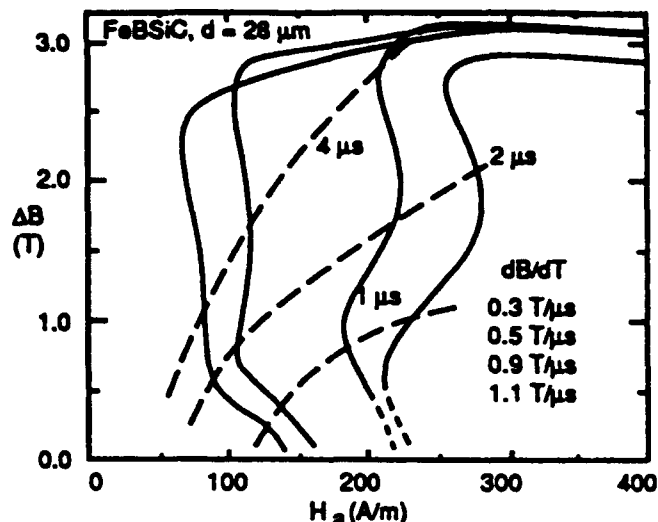
$$\frac{d\phi}{dt} = \omega_0 = \frac{T}{p \sin \theta}$$

The spinning electron can be treated as a spinning top where the forces of gravity are replaced by the magnetic forces. In the case of a spinning electron the angular momentum and magnetic moment are parallel vectors with absolute values of p and μ_e . The gyromagnetic ratio is defined as

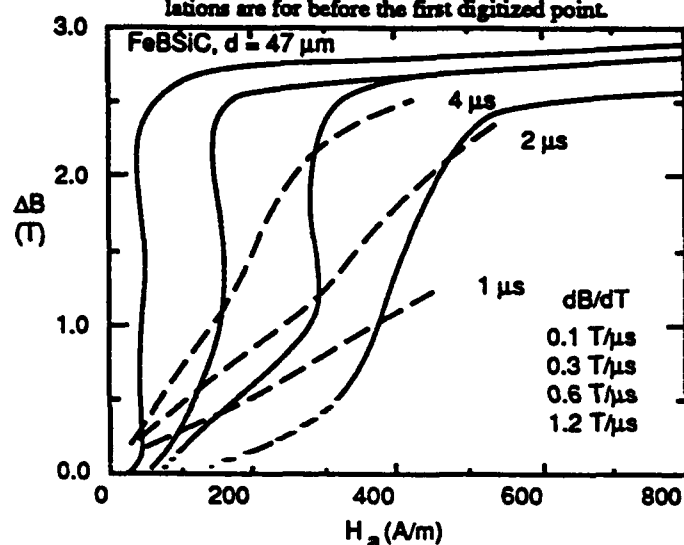
$$\gamma = -\mu_e/p = ge/2mc$$



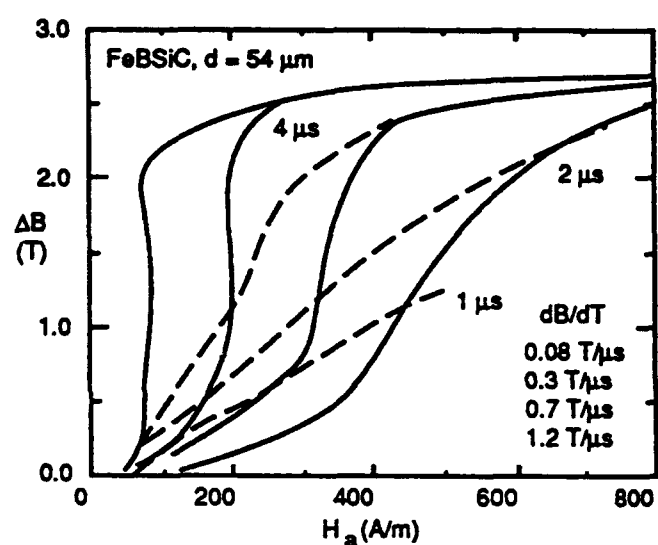
Dynamic magnetization and pulse permeability curves for 13 μm FeBSiC ribbon. Dashed extrapolations are for before the first digitized point.



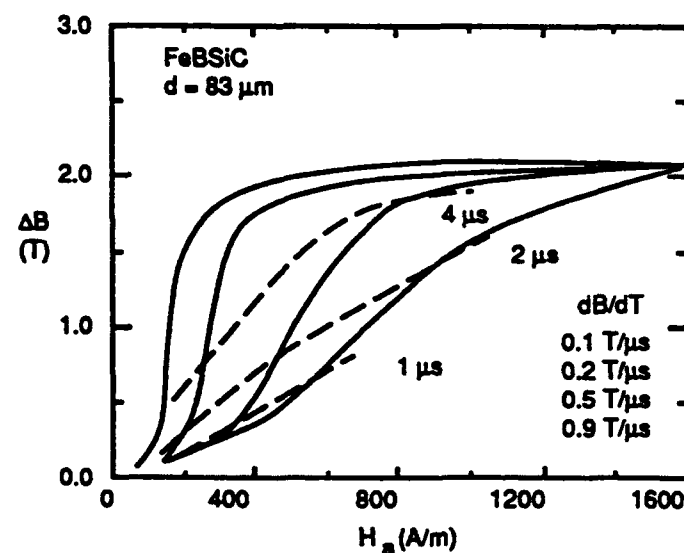
Dynamic magnetization and pulse permeability curves for 28 μm FeBSiC ribbon.



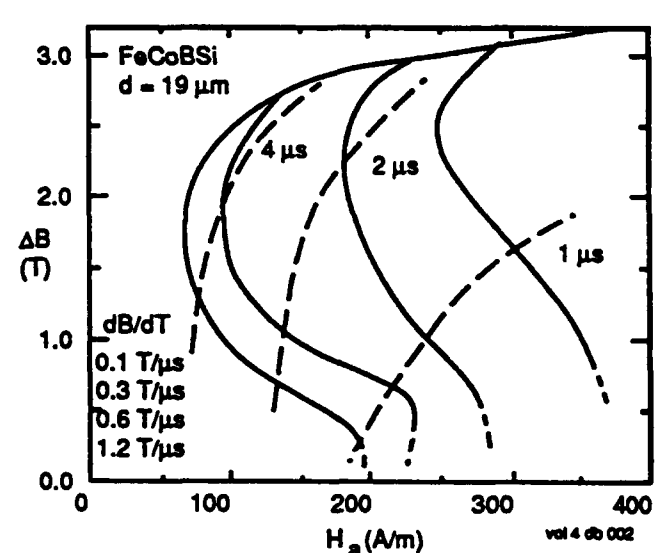
Dynamic magnetization and pulse permeability curves for 47 μm FeBSiC ribbon.



Dynamic magnetization and pulse permeability curves for 54 μm FeBSiC ribbon.



Dynamic magnetization and pulse permeability curves for 83 μm FeBSiC ribbon.



Dynamic magnetization and pulse permeability curves for 19 μm FeCoBSi ribbon.

Figure 2.2: Time dependent ferrite loss measurements

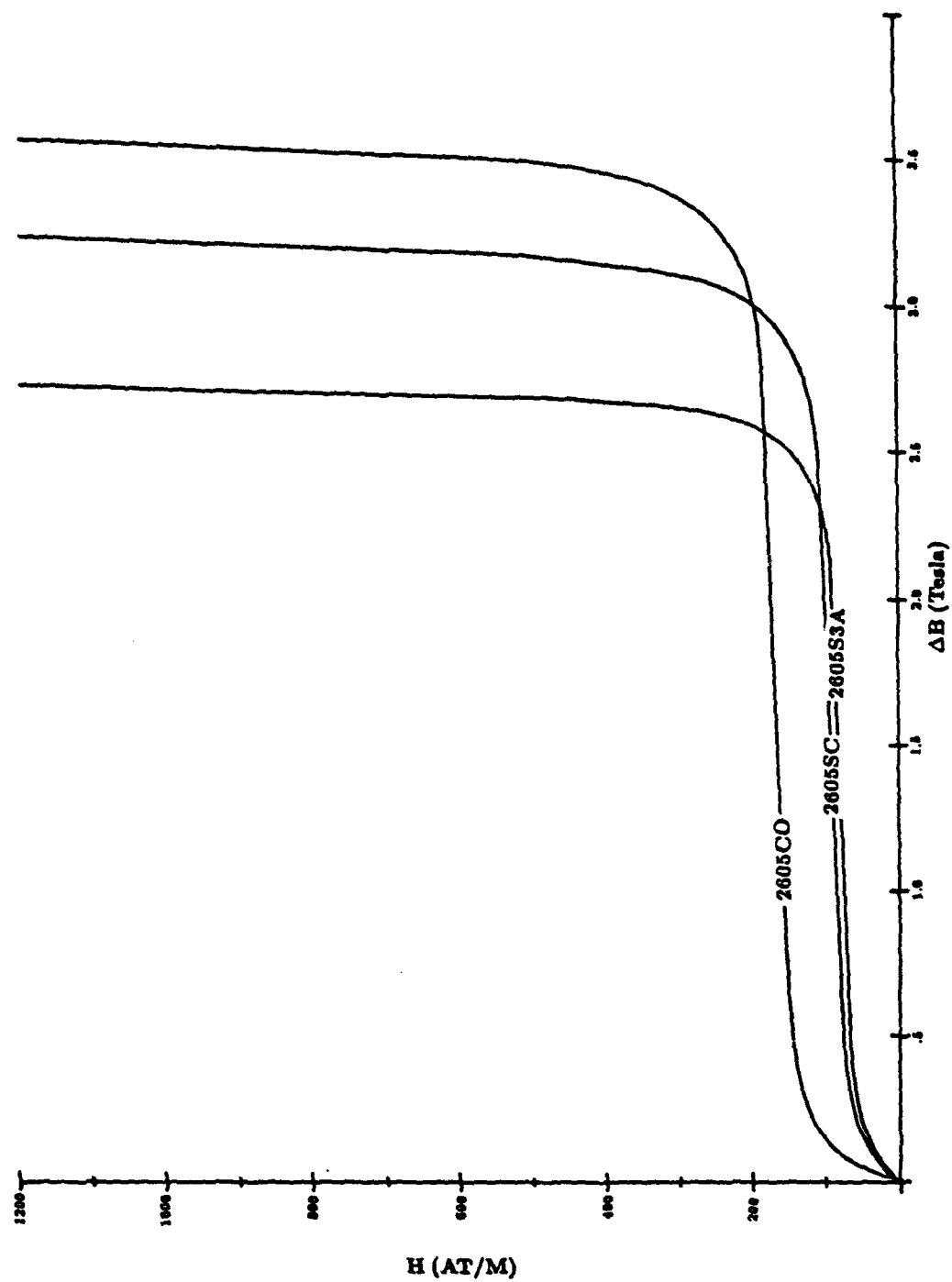


Figure 2.3: 5.0 μ sec Saturation Time

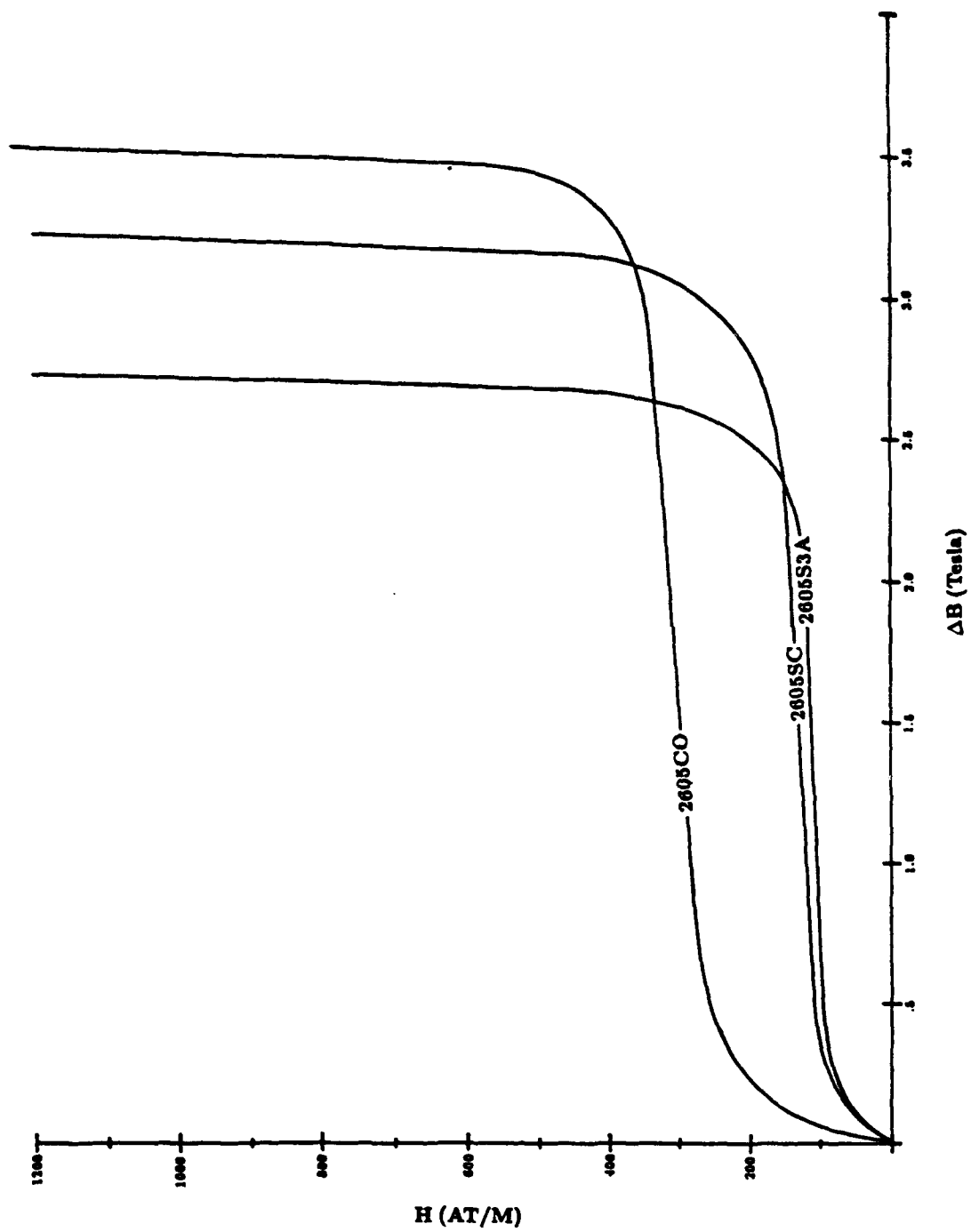


Figure 2.4: 3.0 μ sec Saturation Time

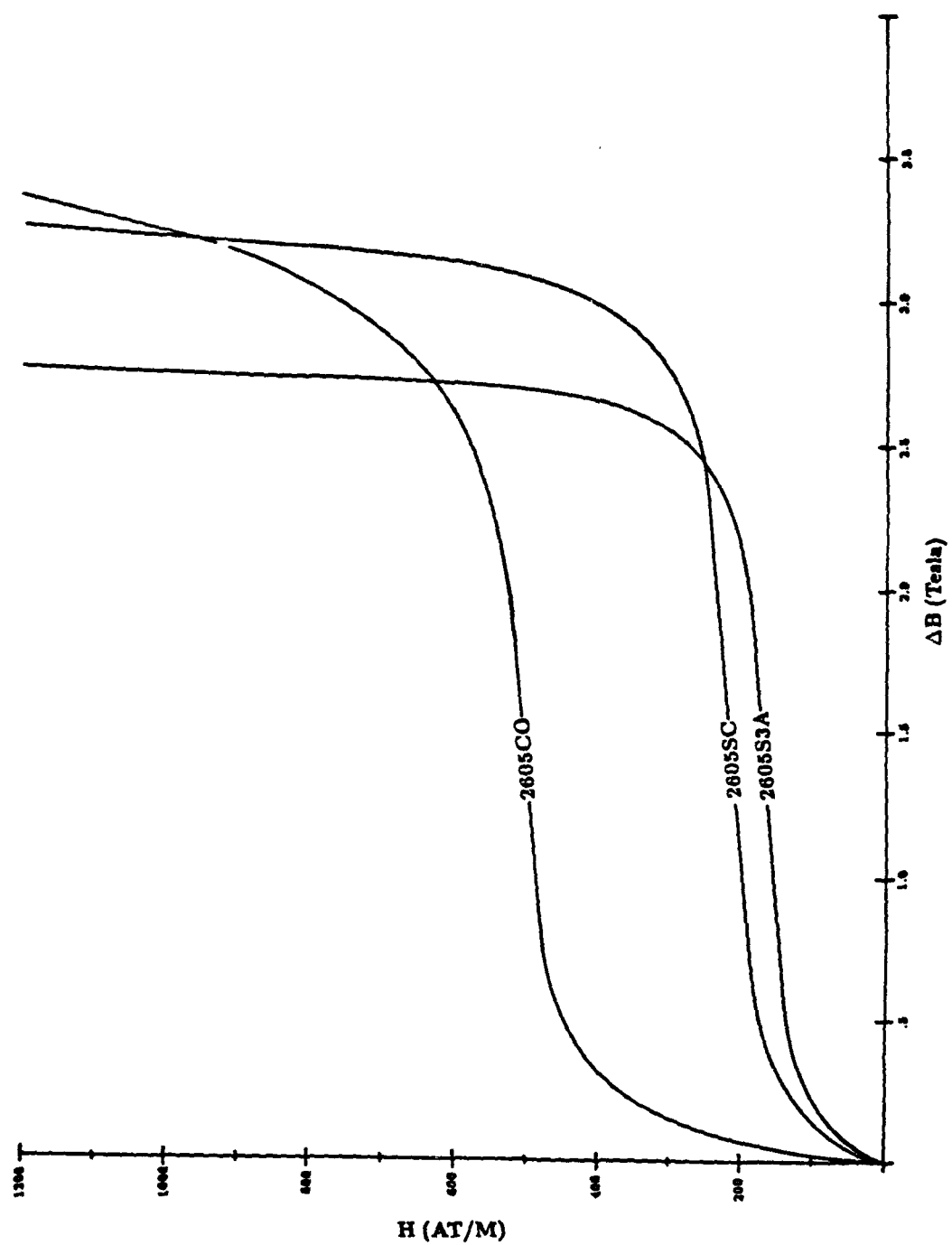
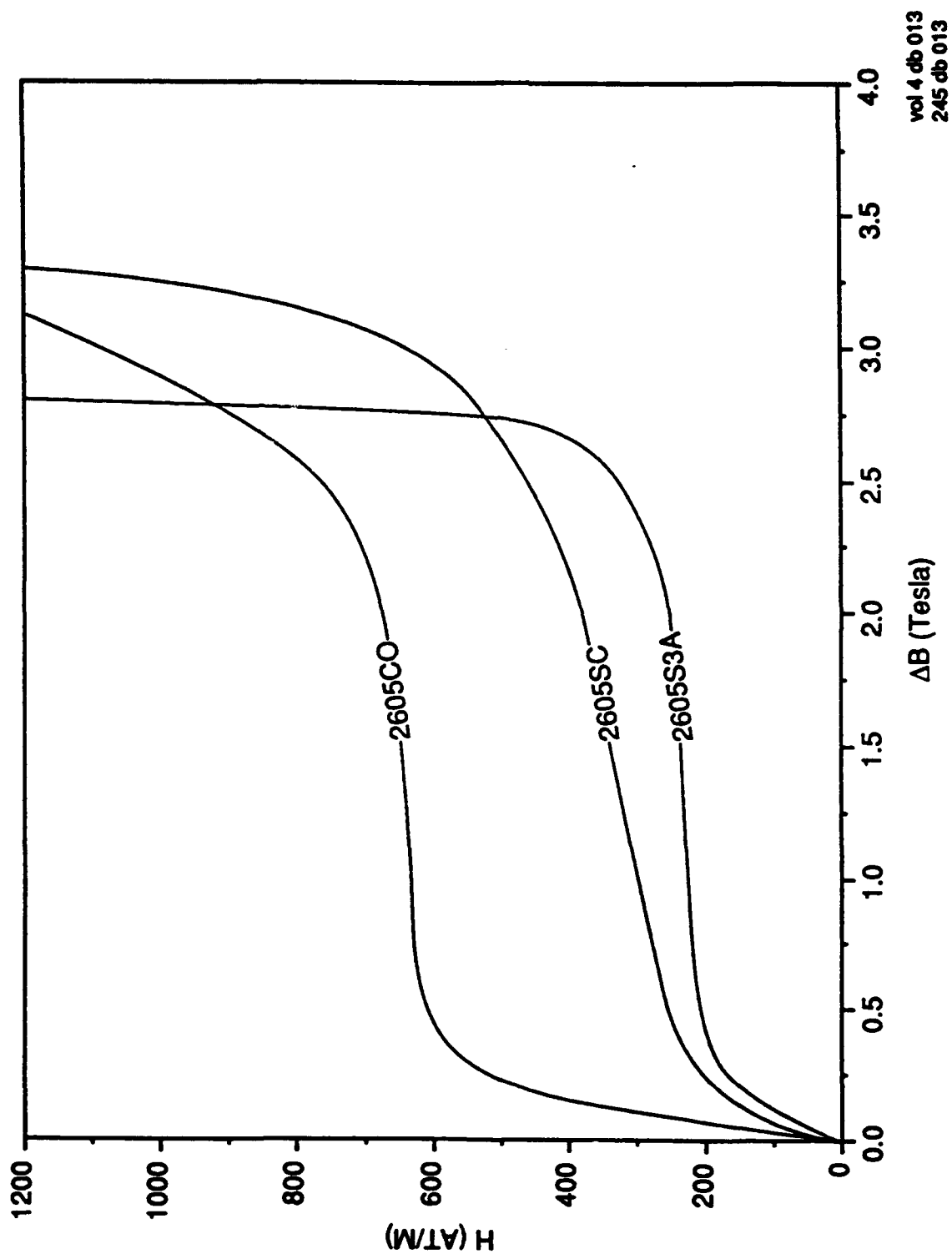


Figure 2.5: 1.5 μ sec Saturation Time



vol 4 db 013
245 db 013

Figure 2.6: 1.2 μ sec Saturation Time

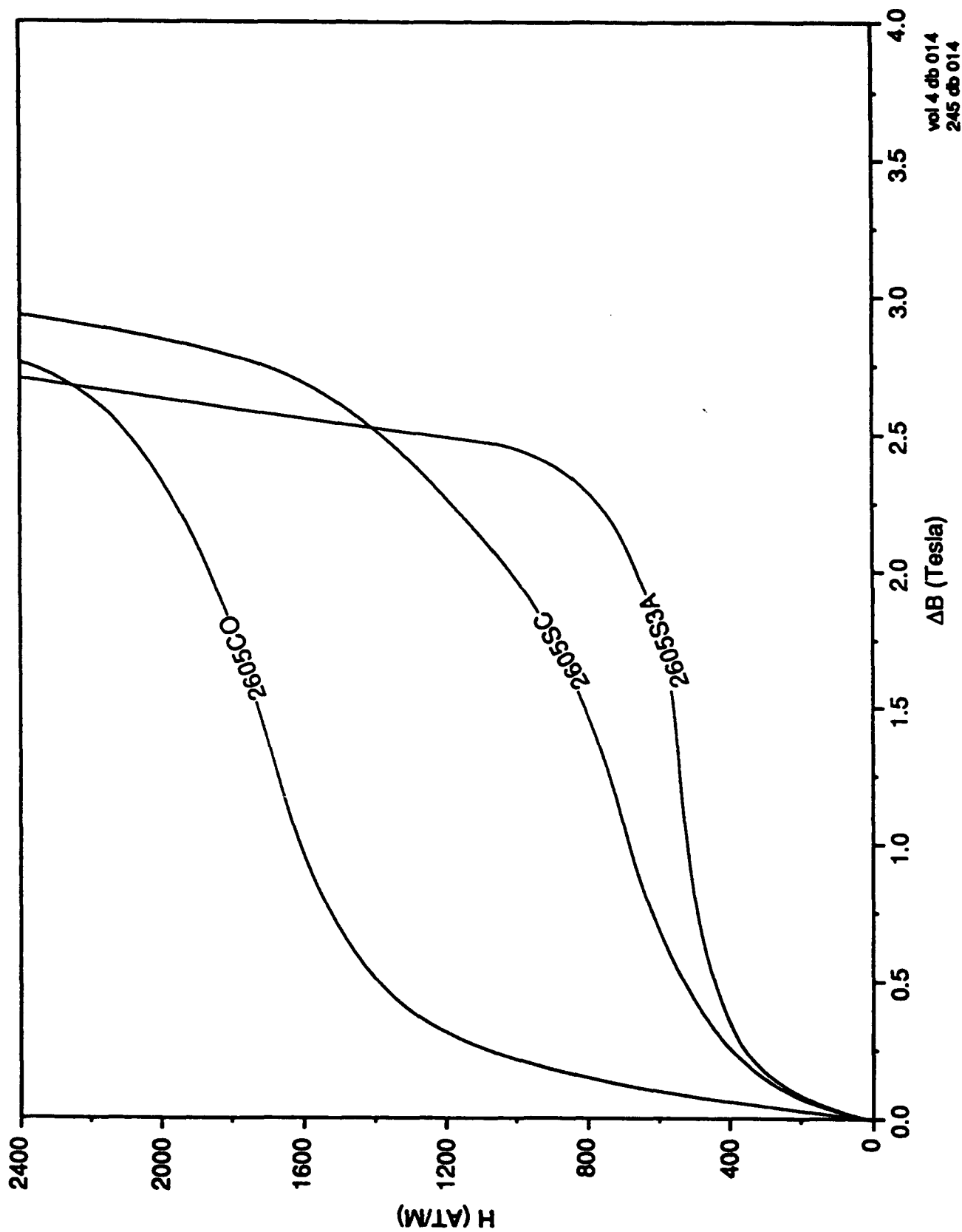


Figure 2.7: 0.5 μ sec Saturation Time

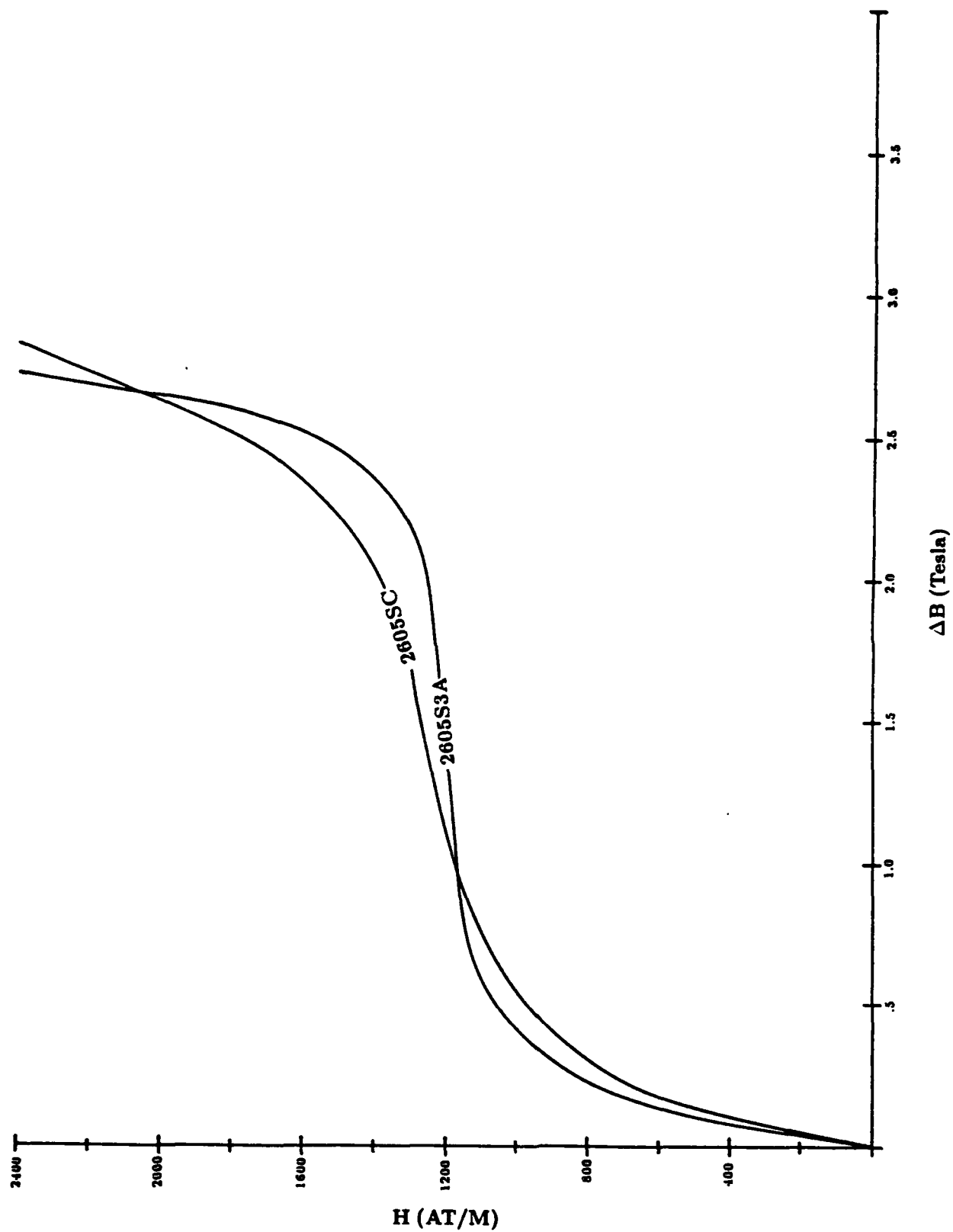


Figure 2.8: 0.25 μ sec Saturation Time

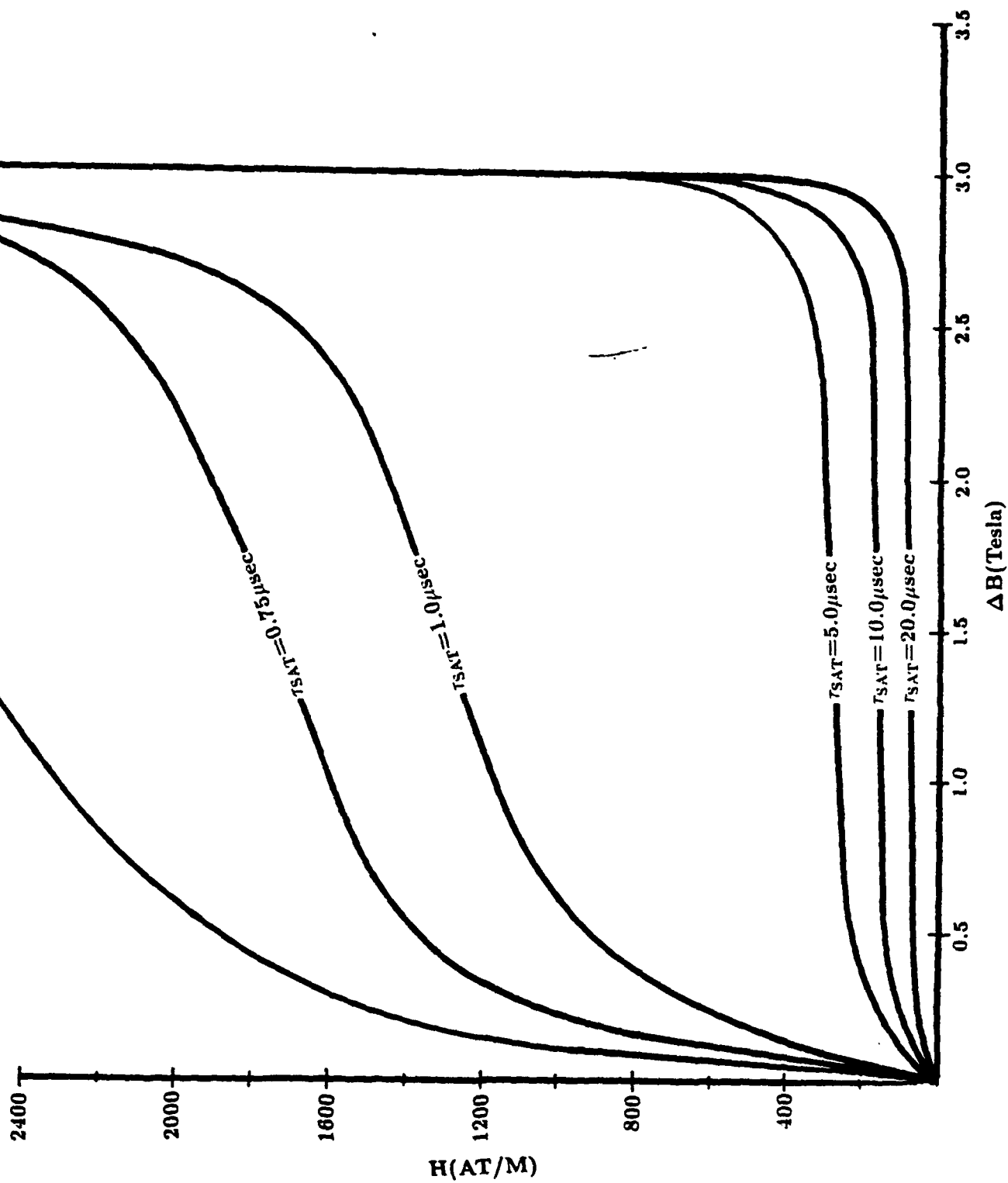


Figure 2.9: 1.2 mil 50-50 Ni-Fe Tape

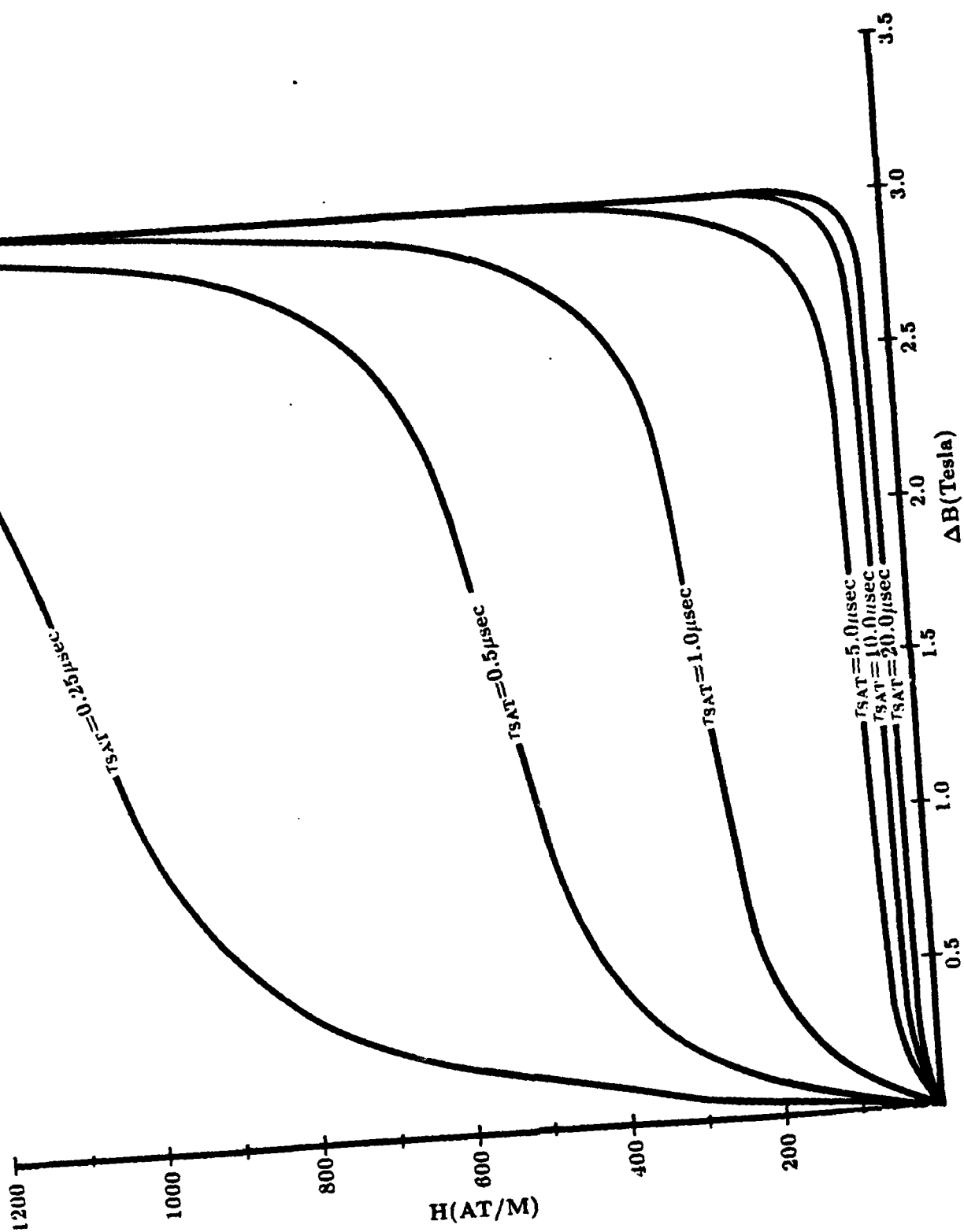


Figure 2.10: 0.6 mil 50-50 Ni-Fe Tape

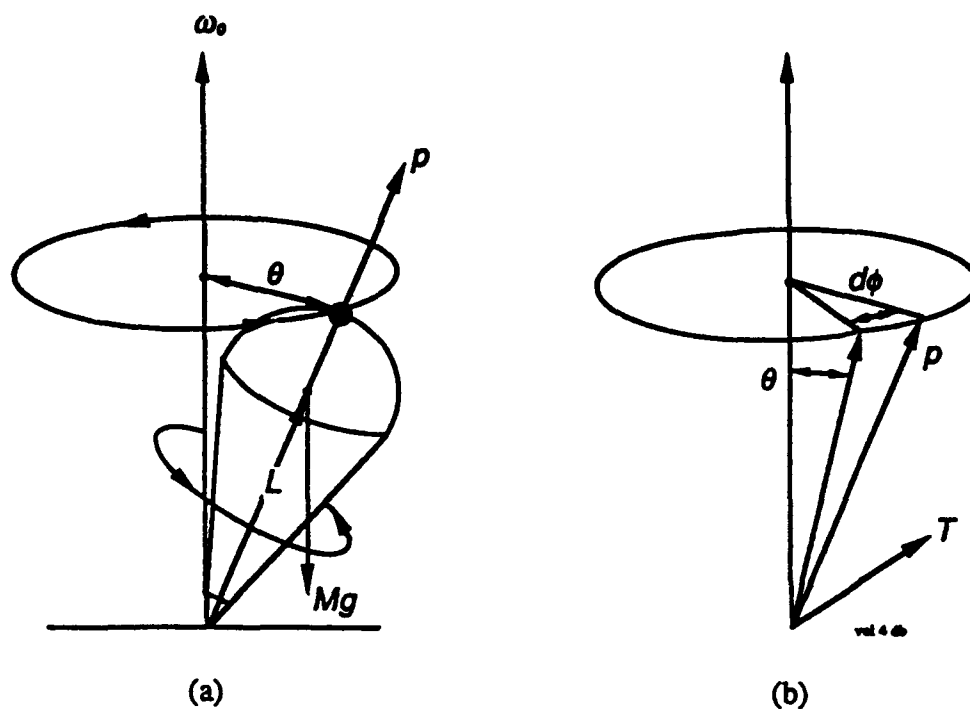


Figure 2.11: Processional motion of a spinning symmetrical top in a gravitational field. The precession of the rigid body at frequency ω_0 is shown schematically in (a), and the angular momentum and torque vectors are shown in (b).

where e is the electronic charge, m the electron mass, c the velocity of light and g is the Lande g -factor and is approximately equal to 2. The torque on the electron from a constant magnetic field is simply

$$T = \mu_e H \sin(\theta)$$

By comparison with the above result for a spinning top, it is obvious that the precessional frequency is simply given as

$$\omega_0 = \gamma H$$

Here the magnetic field H is the actual magnetic field seen by the electron and represents the vector sum of both the internal and applied external fields.

In the case of microwave circulators, a very large external field is applied which dominates the internal fields. In this case the resonance line width is very narrow and occurs at a frequency of thousands of megahertz. In the cases where the internal field dominates, the resonance occurs at much lower frequencies and the linewidth is quite broad as the internal domain structure is by definition nonisotropic and is randomly oriented with respect to the applied field. The internal field arises from the alignment of individual spinning electrons into domains and is given by

$$H_{int} = M_{sat}/\mu - 1$$

If the alignment is truly random, then a simple vector sum will result in an average field given as

$$H_{int} = 2/3 M_{sat}/\mu - 1$$

Therefore, as related above, the resonant frequency in the absence of an externally applied field is given by:

$$\nu_{res} = \frac{\gamma \cdot M_{sat}}{3 \cdot \pi \cdot (\mu_i - 1)}$$

where:

$$\gamma = \text{gyromagnetic ratio } (\sim 0.22 \times 10^6)$$

$$M_{sat} = \text{Saturation magnetization } (2.5 \rightarrow 3.5 \times 10^5 \text{ A/M})$$

$$\mu_i = \text{Initial permeability as } \nu \rightarrow 0.$$

It is now obvious that the resonant frequency of a material can be easily shifted through a variety of measures. Application of an external bias field parallel to the applied time dependent field will increase the resonant frequency. Annealing a toroidal ferrite in the presence of a strong toroidal field can increase the ferromagnetic resonant frequency by a factor of 1.5. Reduction of the permeability will also increase the resonant frequency. This can be accomplished through the introduction of an air gap in the toroid or through a change in composition.

In zinc-nickel ferrites, the initial permeability and therefore the ferrimagnetic resonant frequency can be varied simply by reducing the zinc content and replacing it with additional nickel. An example of this behavior is shown in a plot of the real part of the initial permeability versus frequency for ferrites of various compositions (Fig. 2.12). These ferrites are manufactured by Ceramic Magnetics Corporation and the compositions $(\text{Zn}_{45} \text{Ni}_{55})$, $(\text{Zn}_{30} \text{Ni}_{70})$, $(\text{Zn}_{15} \cdot \text{Ni}_{85})$, $(\text{Ni}_{1.0}) \cdot \text{Fe}_2\text{O}_4$ correspond to C2025, C2050, C2075, N40 respectively. Also available from this manufacturer are the compositions $(\text{Zn}_{54} \text{Ni}_{46})$, $(\text{Zn}_{60} \text{Ni}_{40})$, $(\text{Zn}_{65} \text{Ni}_{35}) \cdot \text{Fe}_2\text{O}_4$ corresponding to C2010, CN20, and CMD5005 respectively.

It is also critical to note that as the initial permeability drops, the Curie temperature increases. This can be understood by realizing that as the permeability drops, the energy required to change

C2025, C2050, C2075, N40 High Frequency Nickel-Zinc Ferrites

This group of materials was specifically engineered to give high flexibility in accommodating requirements to 400 MHz. Our engineering department will work with you on your particular needs to determine which if these ferrites is best for you.

Typical Magnetic Characteristics

	C2025	C2050	C2075	N40
Initial Permeability, <1 MHz	175	100	35	15
Maximum Permeability	1100	390	150	50
Maximum Flux Density, 'gaus	3500	3400	2700	1600
Remanent Flux Density, 'gaus	2600	2400	1800	700
Coercive Force, 'cerstad	1.5	3.0	7.0	7.5
Curie Temperature, °C	270	340	420	510
dc Volume Resistivity, ohm-cm	10^6	10^7	10^8	10^{10}
'@ 40 cerstad applied field strength				

Initial Permeability Versus Frequency

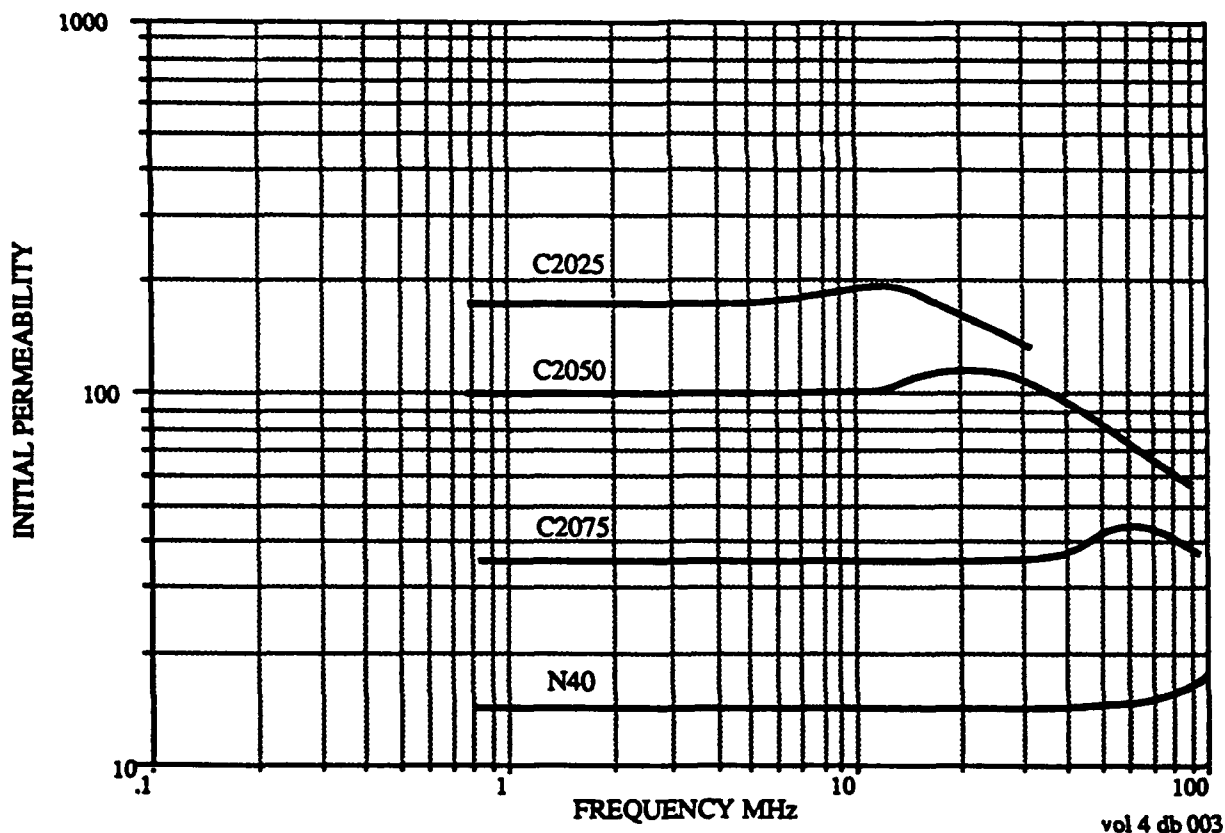


Figure 2.12: High frequency nickel-zinc ferrite permeability

magnetic states increases and therefore the random thermal energy required to disrupt the state also increases.

The frequency dependence of ferrite losses has best been modeled by Landau and Lifshitz. They have proposed that the losses be modeled as

$$\frac{d\vec{M}}{dt} = \gamma(\vec{M} \times \vec{H}) - \lambda \left(\frac{\vec{M} \times (\vec{M} \times \vec{H})}{M_0^2} - \vec{H} \right)$$

In this equation, γ is the gyromagnetic ratio and λ is the relaxation frequency. This model describes the motion of a spinning top in a viscous medium. The term multiplied by γ represents the DC anisotropy and the term multiplied by λ is the viscous damping. The first term represents the precessional motion of the magnetization. This motion as in the case of a spinning top is perpendicular to the direction of both \vec{H} and \vec{M} . The second term signifies a damping force acting on the precessional motion. In the case where the second term dominates, this equation can be rewritten as

$$\frac{dM}{dt} \approx \lambda H \left(1 - \frac{M^2}{M_0^2} \right)$$

The value for λ can be derived from the frequency dependence of the initial permeability. For large displacements around the demagnetized state let us assume

$$\left(1 - \frac{M^2}{M_0^2} \right) \approx 1/2$$

We will also assume the motion is oscillatory in which case

$$\frac{dM}{dt} = i\omega M \approx \frac{\lambda H}{2}$$

and since

$$\mu_r = 1 + \frac{4\pi M}{H}$$

$$\frac{\omega(\mu_r - 1)}{4\pi} = \frac{\nu}{2}(\mu_r - 1) \approx \frac{\lambda}{2}$$

In other words λ is the frequency at which $(\mu_r - 1)$ approaches unity. It might be expected that because the crystal structures are identical, the value of λ would be similar between various ZnNi ferrite compositions. Indeed examination of Fig. 2.13 allows one to draw the conclusion that λ is almost identical between the various compositions and is equal to $\sim 10^{10}$ Hz.

Dielectric Properties

Ferrites are semiconductors with resistivities ranging from $10 \Omega\text{-cm}$ to $10^8 \Omega\text{-cm}$ at room temperature. The relative dielectric permittivity ranges from 10 to as high as 100,000. The dielectric permittivity along with its frequency dependence are extremely important parameters in electromagnetic shock line design as the ferrite forms the transmission line medium.

Ferrite is a polycrystalline material consisting of semiconducting grains surrounded by thin boundaries with much higher resistivity. The grain boundaries are typically composed of insoluble

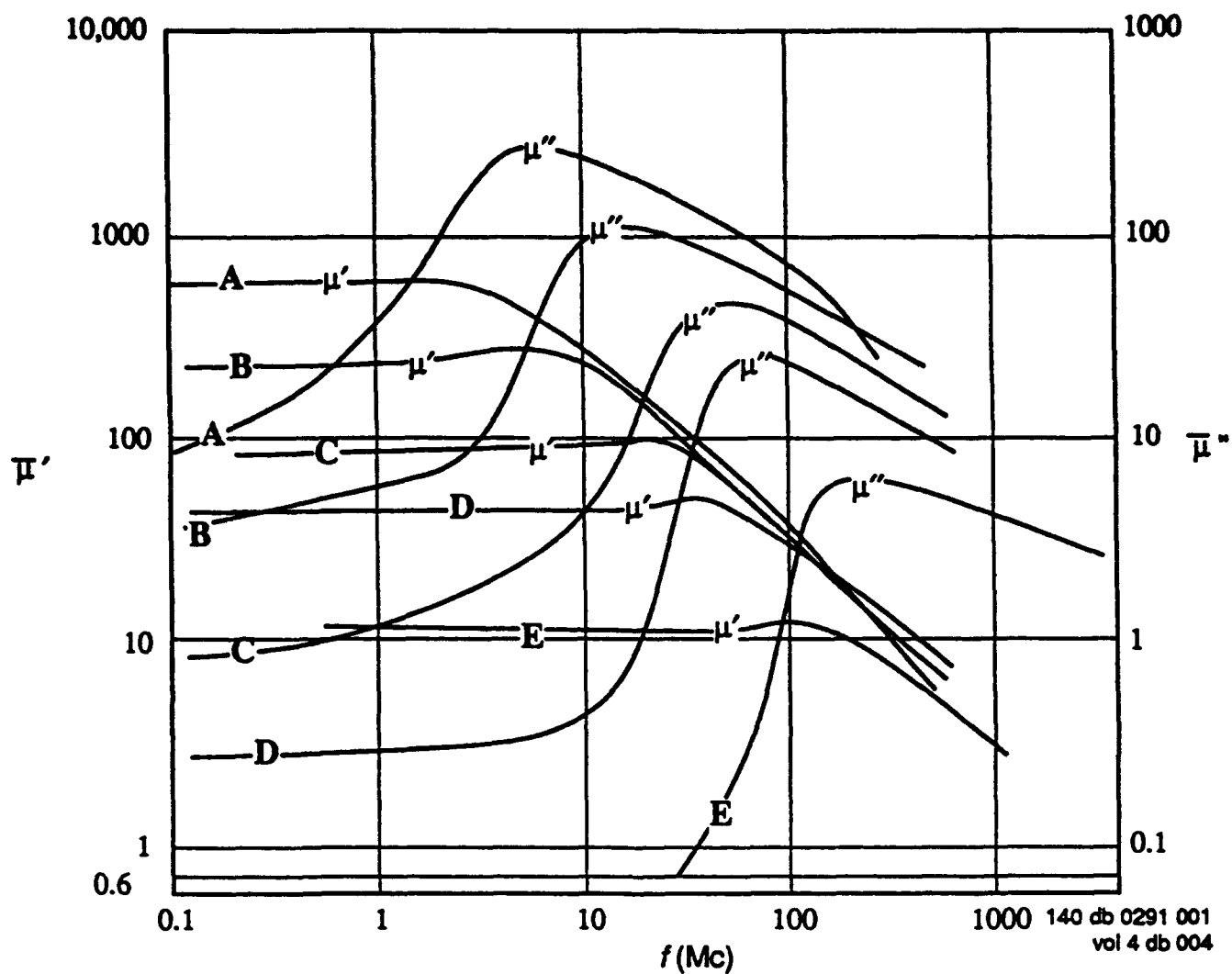


Figure 2.13: Frequency dependence of real and imaginary parts of the initial permeability for polycrystalline NiZn ferrite. (compositional ratio NiO:ZnO = (A) 17.5:33.2, (B) 24.9:24.9, (C) 31.7:16.5, (D) 39.0:9.4, (E) 48.2:0.7, remaining part Fe_2O_3 (Gorter)).

materials which diffuse into the grain boundaries during sintering. They are typically nonmagnetic and are occasionally added intentionally. Calcium Oxide and Silicon Dioxide are examples of materials which are sometimes added by the manufacturer to increase the low frequency resistivity. One example of such a material is Ceramic Magnetics MN8CX. This ferrite is a manganese-zinc ferrite with an artificially high DC resistivity of 10,000 Ω -cm. As we will see below, such additions are of little practical significance at high frequencies at which the large capacitance of these grain boundaries shunts the high resistivity, exposing the inherent resistivity of the crystallites.

If we define α as the ratio of the boundary layer thickness to thickness of the average crystallite, then we can predict the dielectric behavior of the ferrite based on the experimentally determined conditions that $\alpha \ll 1$, $\epsilon_{crystallite} \approx \epsilon_{boundary}$, and $\alpha \rho_{boundary} \gg \rho_{crystallite}$. Therefore at low frequencies the impedance of the crystallite is negligible compared with the impedance of the boundary layers and the resistivity is approximately given as $\alpha \rho_{boundary}$ and the permittivity approaches $\epsilon_{boundary}/\alpha$.

At high frequencies the boundary layer capacitance is short-circuited by the high boundary layer capacitance and the dielectric permittivity and resistivity approach that of the crystallites. The relaxation frequency is defined as $1/2\pi\tau$ where τ is the characteristic decay time of the junction capacitance. The relaxation frequency is given by

$$f_r = \frac{1}{2\pi\epsilon_0} \frac{\frac{1}{\rho_{crystallite}} + \frac{1}{\rho_{boundary}}}{\epsilon_{crystallite} + \epsilon_{boundary}/\alpha}$$

Experimentally-measured curves of both permittivity and resistivity as a function of frequency for two different zinc-nickel compositions are presented in Fig. 2.14. These compositions labeled B1 and 4B1 are produced by Phillips and correspond to $(Zn_{60} Ni_{40})$ and $(Zn_{50} Ni_{50}) \cdot Fe_2O_4$ respectively.

The eddy current power loss density is simply given as

$$P = \frac{(\omega B_0 d)^2}{\rho \beta}$$

where ρ is the resistivity, d is the characteristic dimension and β is the geometric factor. For a toroid, d is the width of the toroid and $\beta = 24$. For a sphere, d is the diameter and $\beta = 80$. The eddy current losses can also be characterized as a contribution to the loss angle given as

$$\tan(\delta_r) = \frac{\omega \mu \mu_0 d^2}{2\rho \beta}$$

The resistivity and permittivity are also temperature dependent. This effect is documented by the measurements presented in Fig. 2.15 of the same two compositions. These measurements were taken at 1 MHz but the slopes of the curves are similar at differing frequencies.

The curves indicate that for Zn-Ni compositions, the resistivity never will drop below 10^4 Ω -cm. This resistivity is 10^8 times higher than the resistivity of metglass. The eddy current losses in a 1 inch thick Zn-Ni toroid are equivalent to the losses in a 0.1 mil metglass tape for the same flux excursion. In Mn-Zn ferrites, the eddy current losses cannot be neglected as they approach 10 Ω -cm in the frequency range we are interested in. This means that a 1 inch thick Mn-Zn ferrite toroid will exhibit eddy current losses equivalent to 3 mil thick metglass tape undergoing the same flux excursion. In addition the Mn-Zn ferrites exhibit a large dielectric constant. Electromagnetic

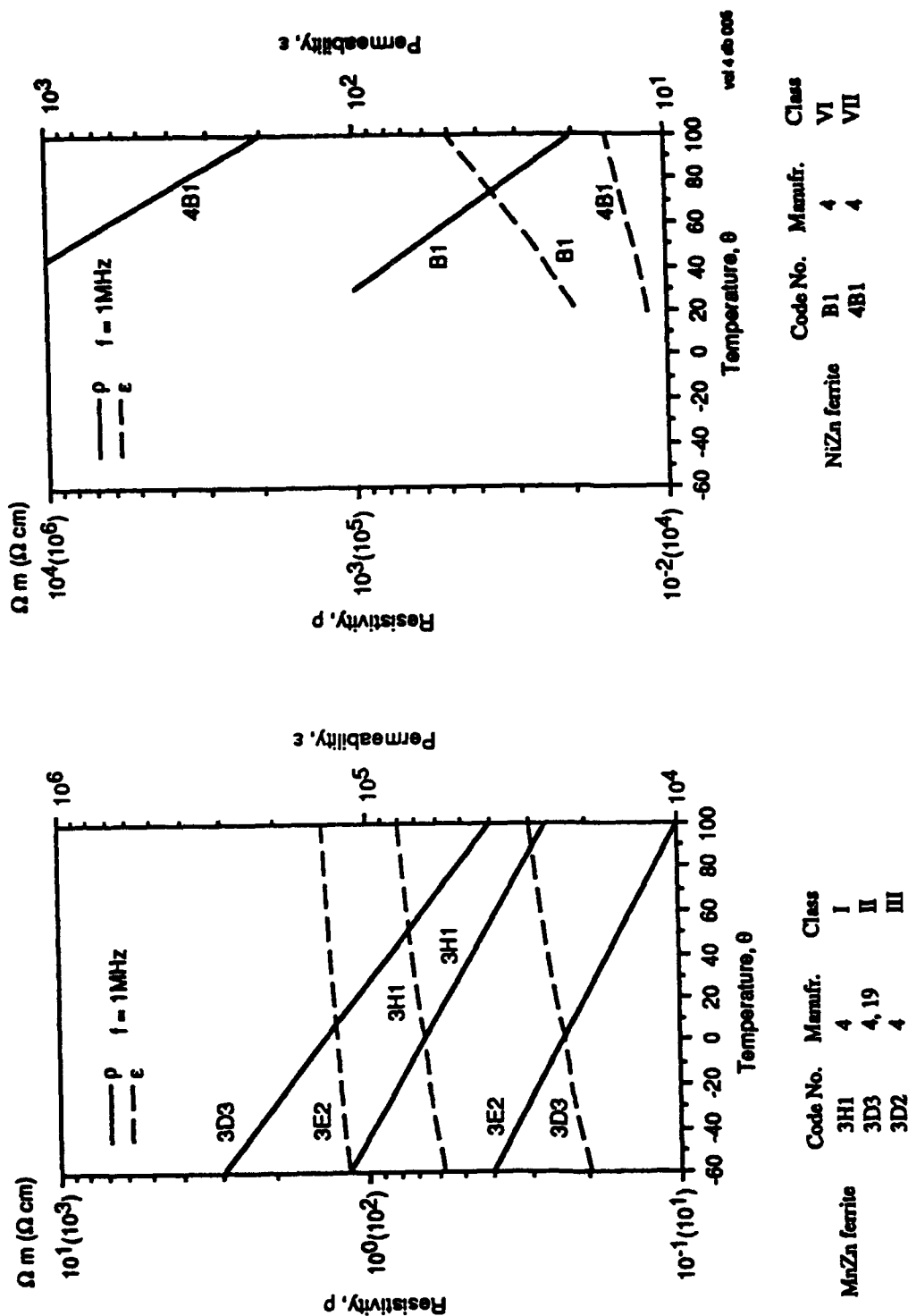
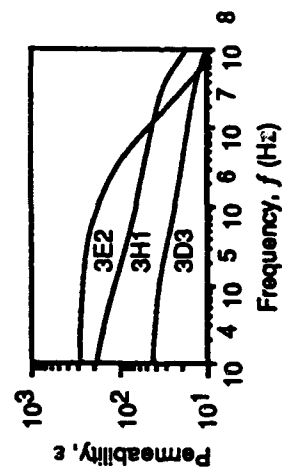
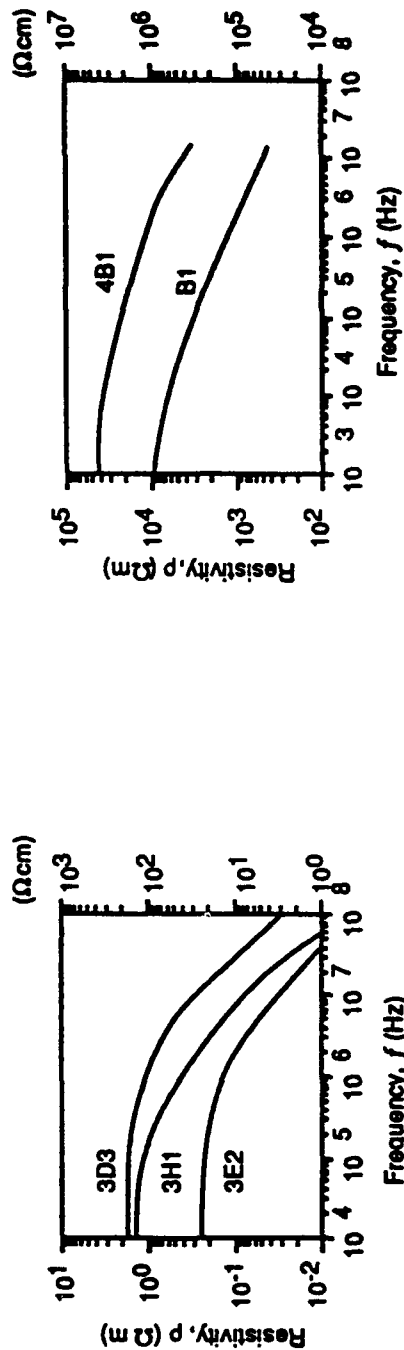
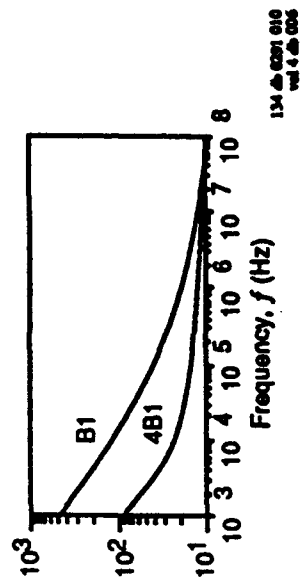


Figure 2.14: Resistivity of various ferrites as a function of temperature



	Code No.	Manufr.	Class
MnZn ferrite	3H1	4	I
	3D3	4, 19	II
	3D2	4	III



	Code No.	Manufr.	Class
NiZn ferrite	B1	4	VI
	4B1	4	VII

Figure 2.15: Resistivity and permeability of various ferrites as a function of frequency

radiation propagates through the material at only a few centimeters per microsecond. This allows fairly small structures to be resonant in the frequency ranges of interest. If the entire ferrite toroid forms a single resonant structure, the loss tangent approaches unity.

Ferrite Sample Measurements

Sample ferrites were tested which spanned the range of applicable compositions. These ferrites were manufactured by Ceramic Magnetics Corporation and the compositions purchased - (Zn₆₅ Ni₃₅), (Zn₆₀ Ni₄₀), (Zn₅₄ Ni₄₆), (Zn₄₅ Ni₅₅), (Zn₃₀ Ni₇₀), (Zn₁₅ · Ni₈₅), (Ni_{1.0}) · Fe₂O₄ - correspond to CMD-5005, CN20, C2010, C2025, C2050, C2075, N40 respectively. Preliminary evaluation eliminated both C2075 and N40 from consideration.

A simplified schematic of the test stand used to evaluate these samples is presented in Fig. 2.16. Samples were reset slowly and then rapidly cycled from $-B_r$ to B_s . Minor loops were not measured as they are not of interest in the applications we are considering where all of the available flux excursion in the ferrite is typically required. The saturation time-scales which could be measured range from 50ns to 500ns. At saturation times longer than 500ns, metal tape wound cores will outperform any available ferrite. At saturation times shorter than 50ns the test stand did not have sufficient drive power. The experimental results are presented in Figs. 2.17-2.20.

The energy dissipated in the ferrite as the flux swings from $-B_r$ to B_s is plotted as a function of saturation time in Fig. 1.21. The units are Joules/Meter³ versus saturation time in nanoseconds.

If the ferrite is employed as a saturable reactor in a nonlinear magnetic compressor, then the volume of core required is linearly dependent on the square of the available flux swing. Simply because a candidate material exhibits a lower loss per unit volume does not mean it is the best choice as the core material. The best technique to identify the optimum core material in a saturable reactor is to plot energy loss per meter³ per Tesla². This plot appears in Fig. 2.22.

In high repetition rate applications, temperature rise can be an issue. As the temperature rises, the available flux swing is reduced until at the Curie temperature the available ΔB goes to zero. The higher the Curie temperature for a given composition, the more power can be dissipated in a given size sample with a specified surface temperature. In a case where the ferrite surface is anchored to a temperature of 50°C, the plot in Fig. 2.23 gives an indication of the maximum repetition rate at which a given composition can be operated. Here the energy loss per cycle is divided by the maximum allowable temperature rise. The lower a curve lies on this plot, the higher the usable repetition rate.

Even though the permeability of various ferrite compositions all approach the same value as the saturation time approaches zero, there are some applications which can benefit by a ferrite composition exhibiting a reduced ΔB . As an example, the optimum ferrite for use in an electromagnetic shock line is the ferrite which saturates at the minimize H field at a given time scale. Therefore if the permeability is to be a constant independent of composition, the composition which will yield the minimum risetime in a shock line application is that which exhibits the minimum ΔB . TTVG-800 and G-350 are two examples of reduced ΔB ferrites which are available from microwave ferrite suppliers such as Trans-Tech. The saturation flux of TTVG- 800 is 1/3 that of CMD-5005 while G-350 exhibits less than 1/6 the ΔB of CMD-5005. This is further illustrated in Fig. 2.24 where coercive force is plotted against saturation time. At time scales of order 1 nanosecond or less the output risetime of an electromagnetic shock line will scale linearly with the exhibited ΔB .

In Fig. 2.25 we plot the energy lost per cubic meter of magnetic material as a function of material and saturation time. As it turns out the saturation losses of ferrite scale linearly with the inverse of saturation time due to spin resonance damping while the metal tapes show the same temporal behavior but for a different reason. In the case of metal tapes the losses at short

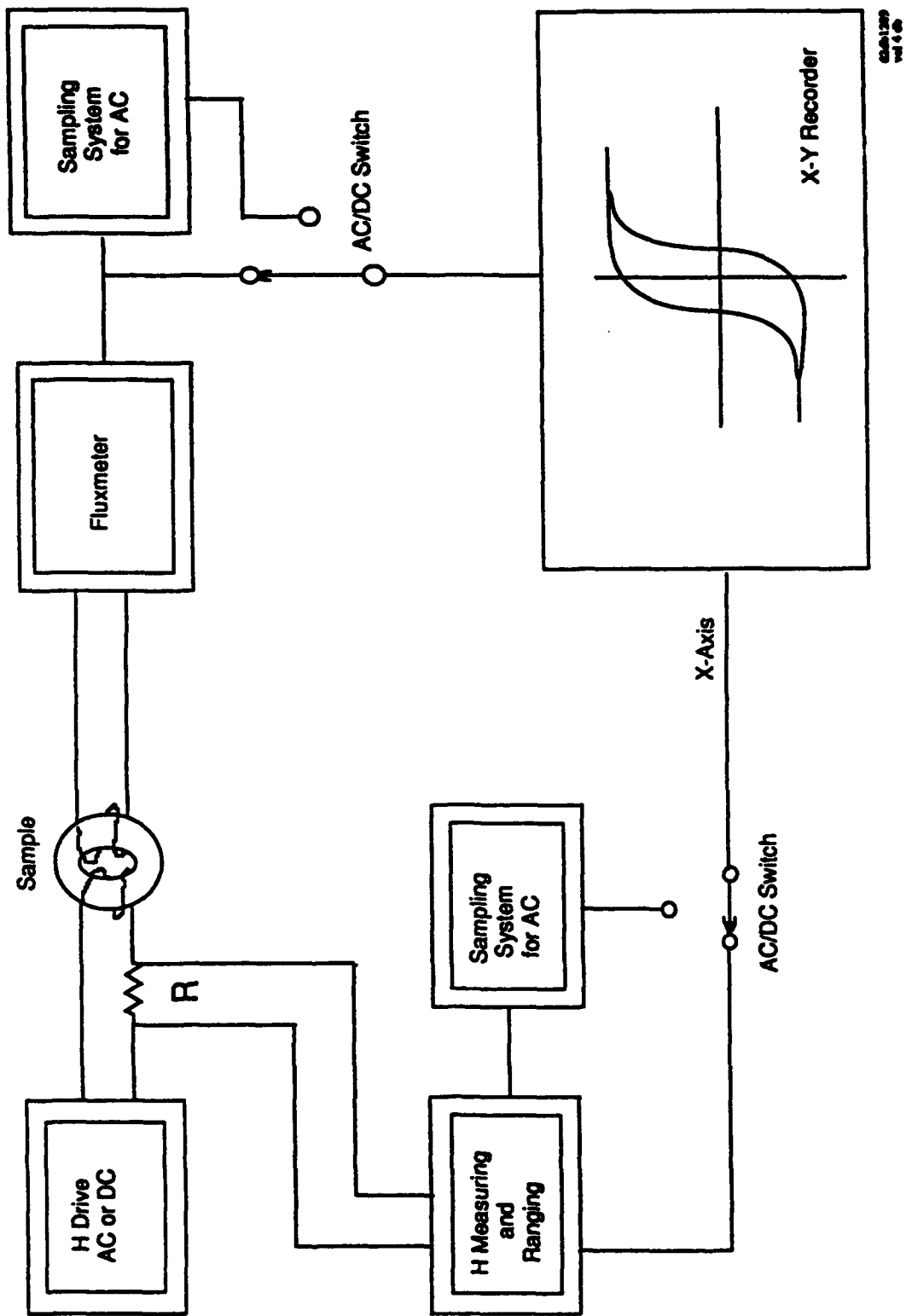


Figure 2.16: B-H loop measurements

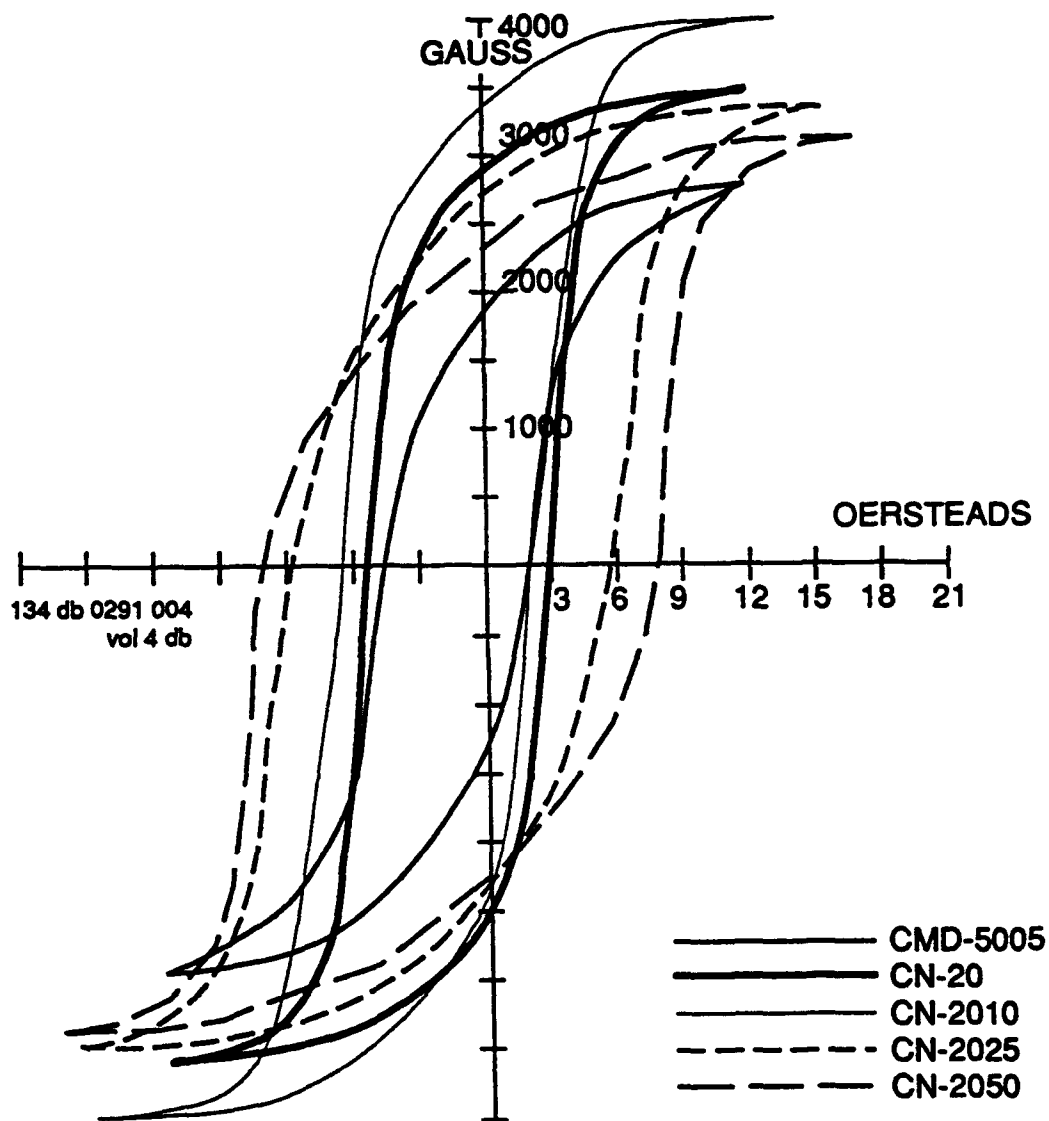


Figure 2.17: Hysteresis curves measured at $\tau_{sat} = 500$ ns

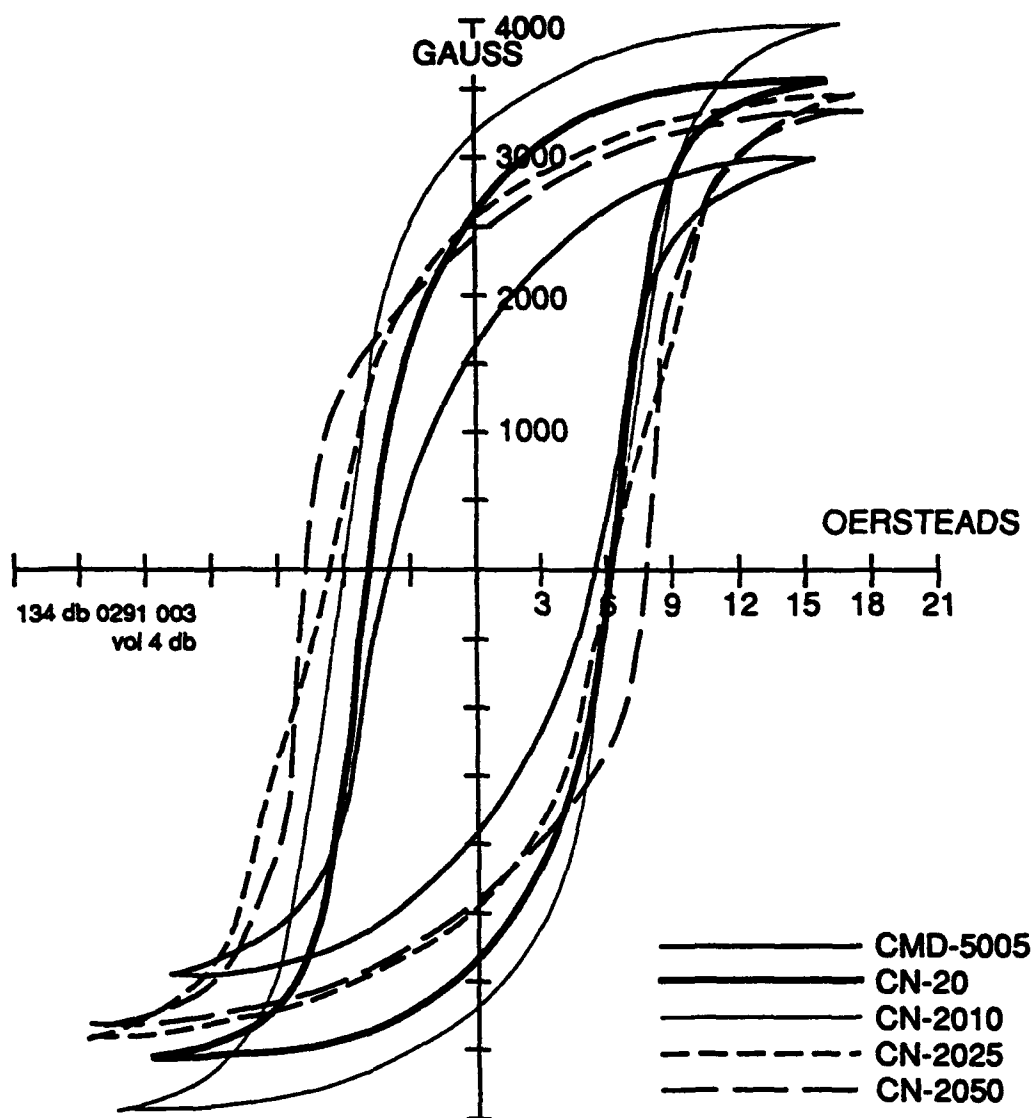


Figure 2.18: Hysteresis curves measured at $\tau_{sat} = 250$ ns

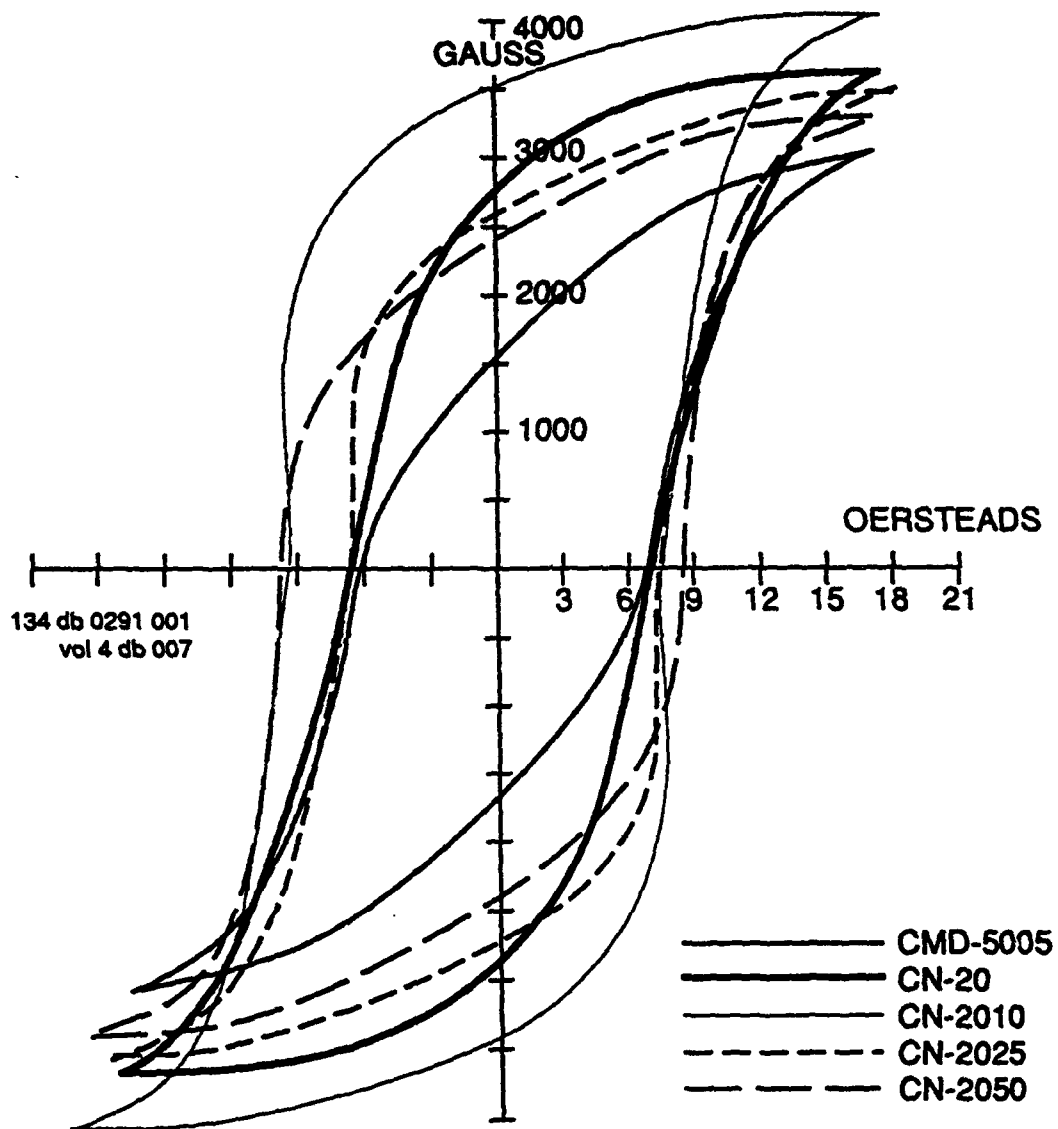


Figure 2.19: Hysteresis curves measured at $\tau_{sat} = 100$ ns

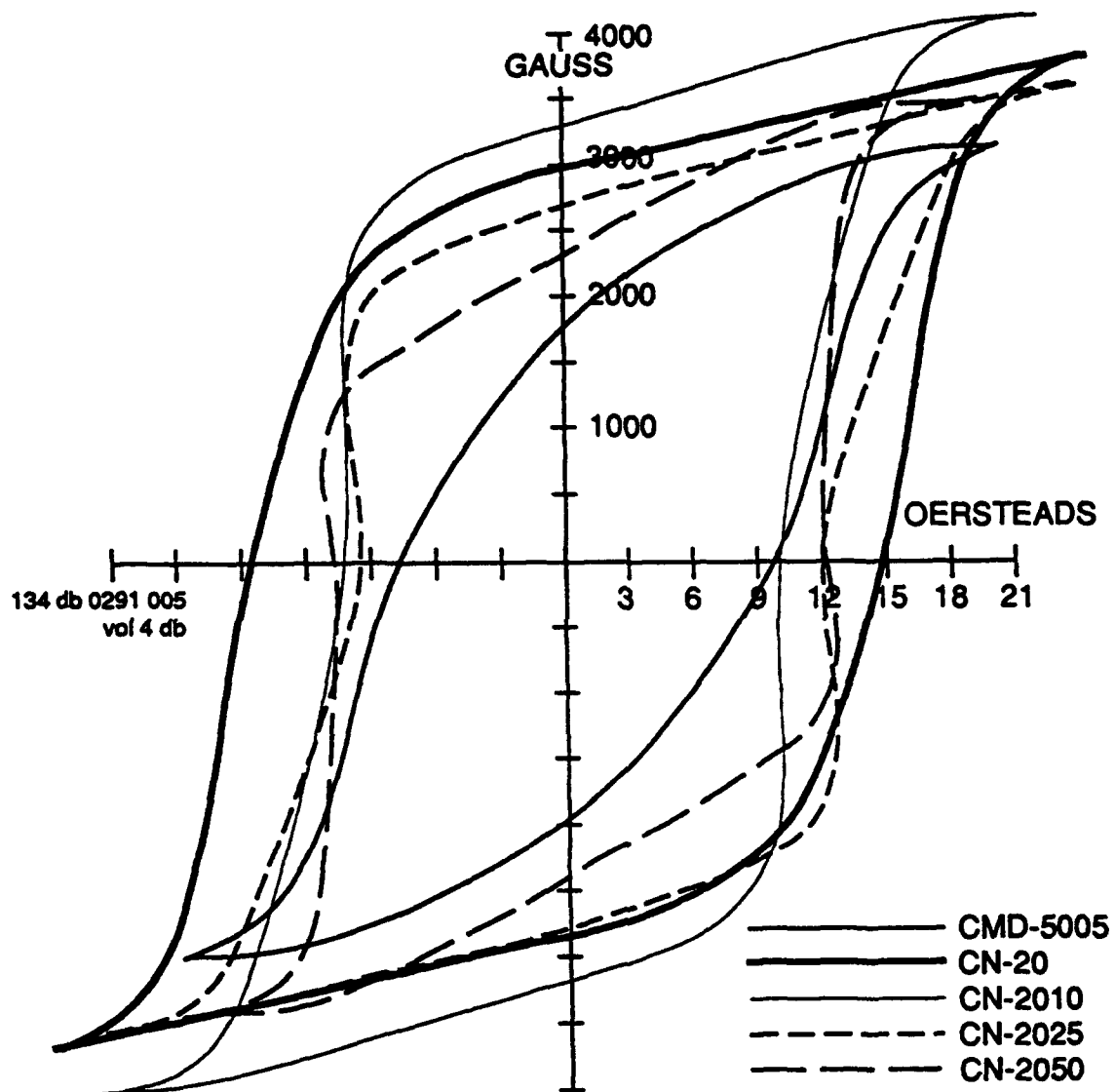


Figure 2.20: Hysteresis curves measured at $\tau_{sat} = 50$ ns

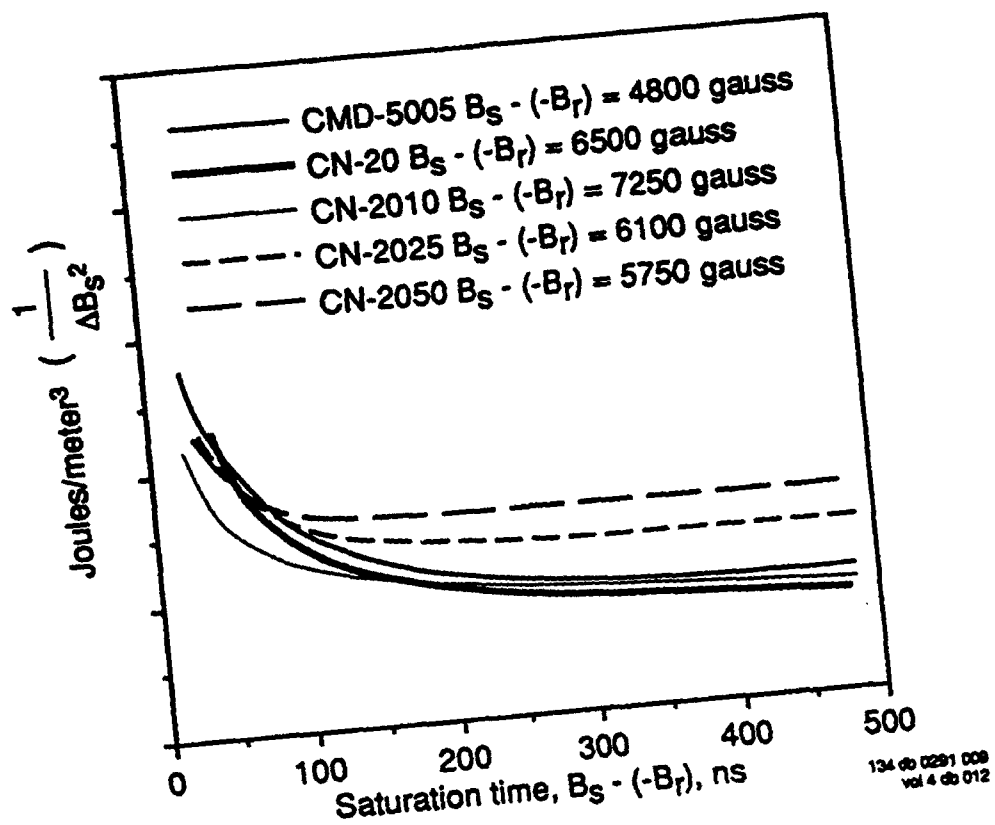


Figure 2.21: Normalized energy dissipated in various ferrite materials as a function of saturation time.

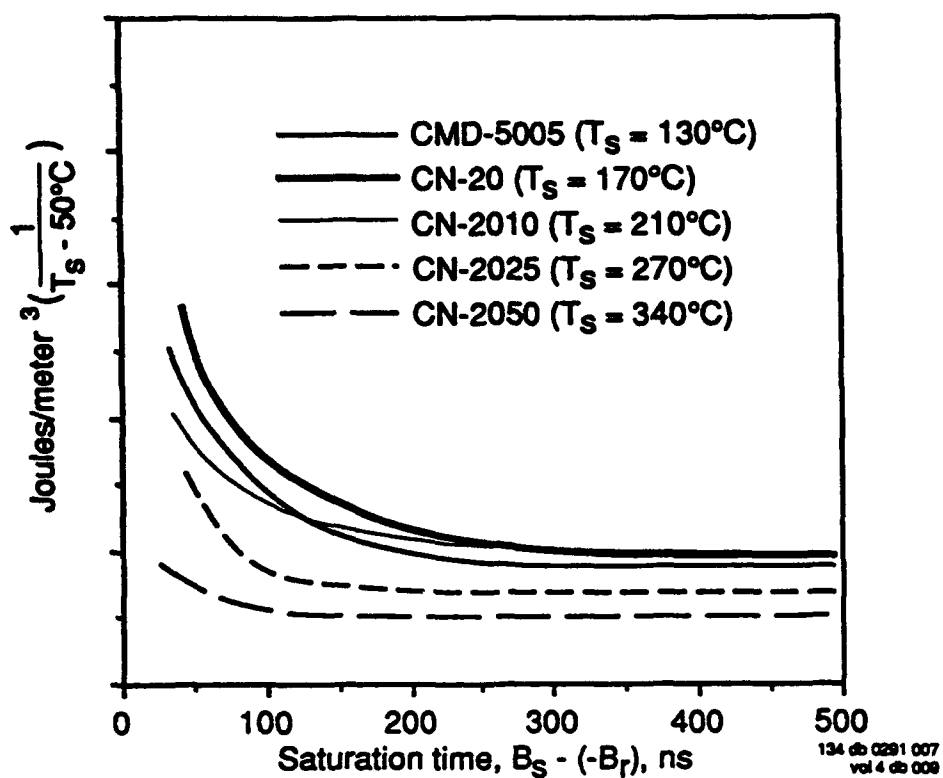


Figure 2.22: Data for maximum temperature rise allowable in various ferrite materials

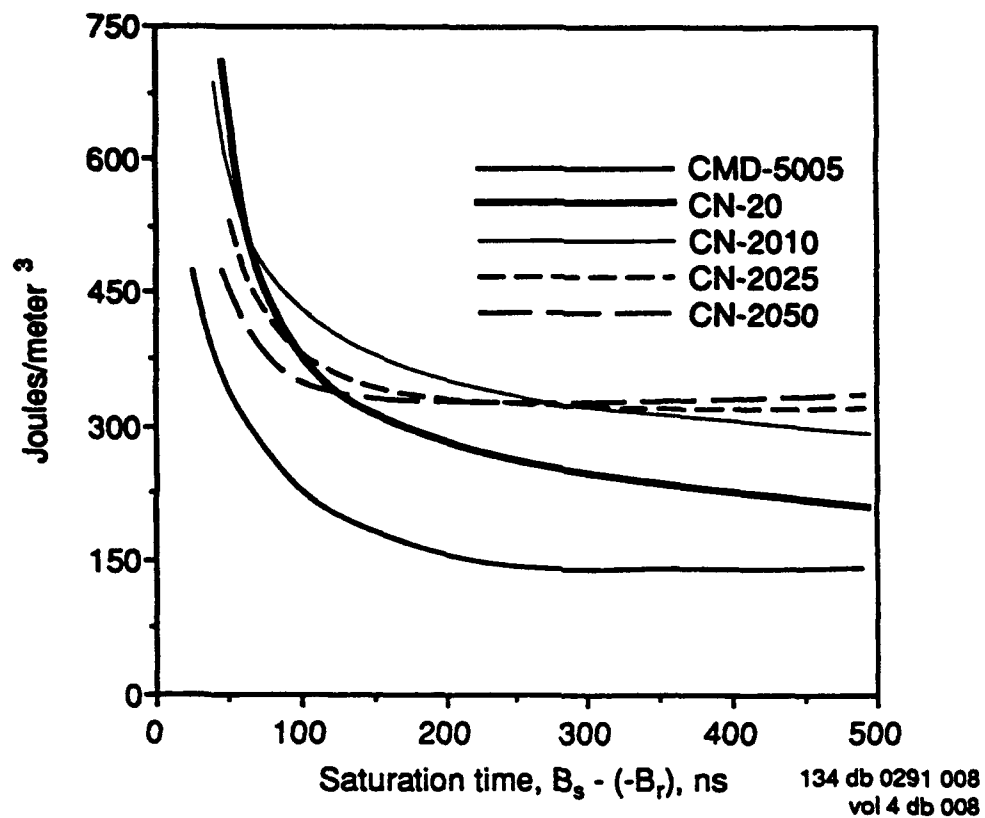


Figure 2.23 Energy dissipated in ferrite materials as a function of saturation time.

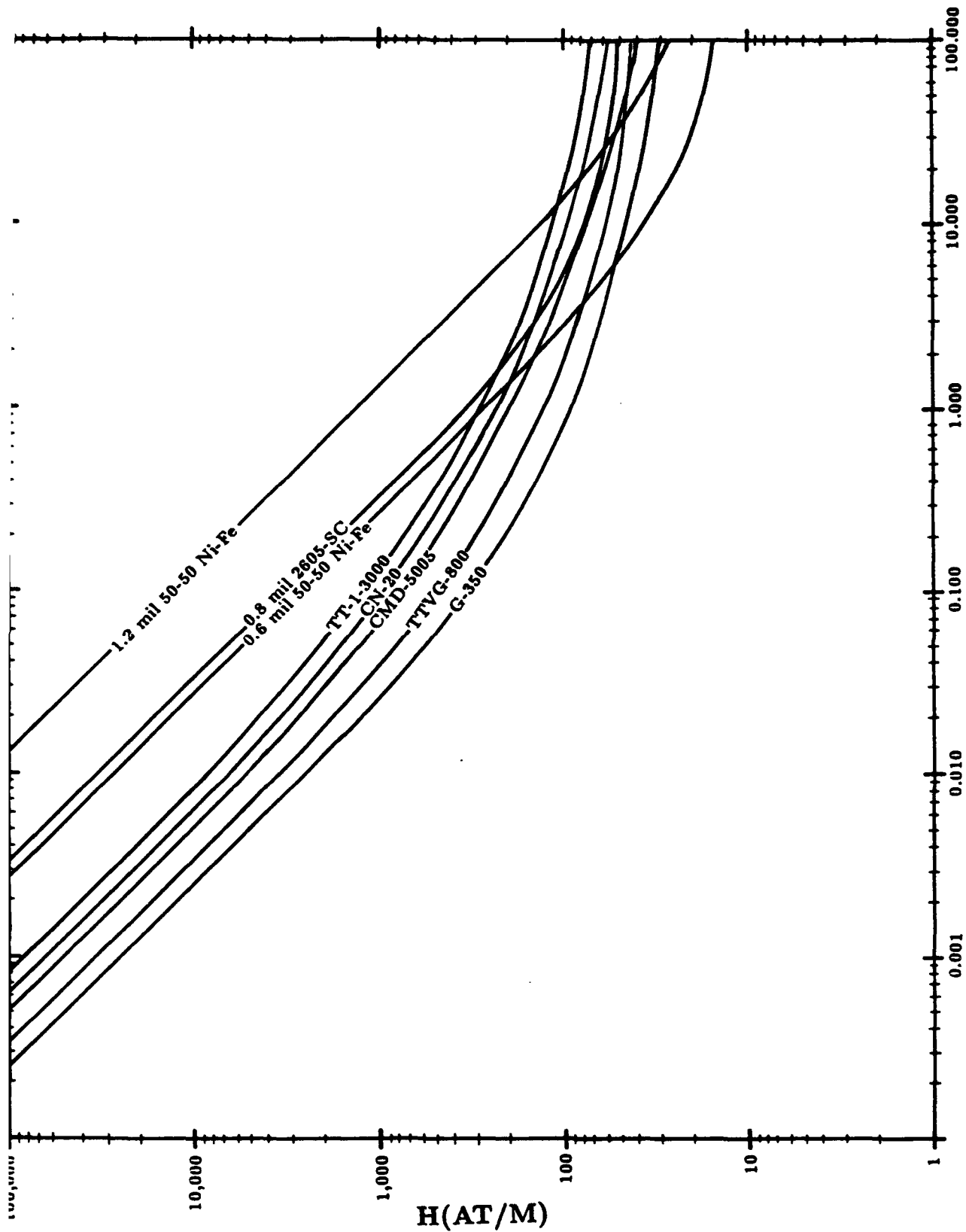


Figure 2.24: Square Wave Saturation Time (μsec)

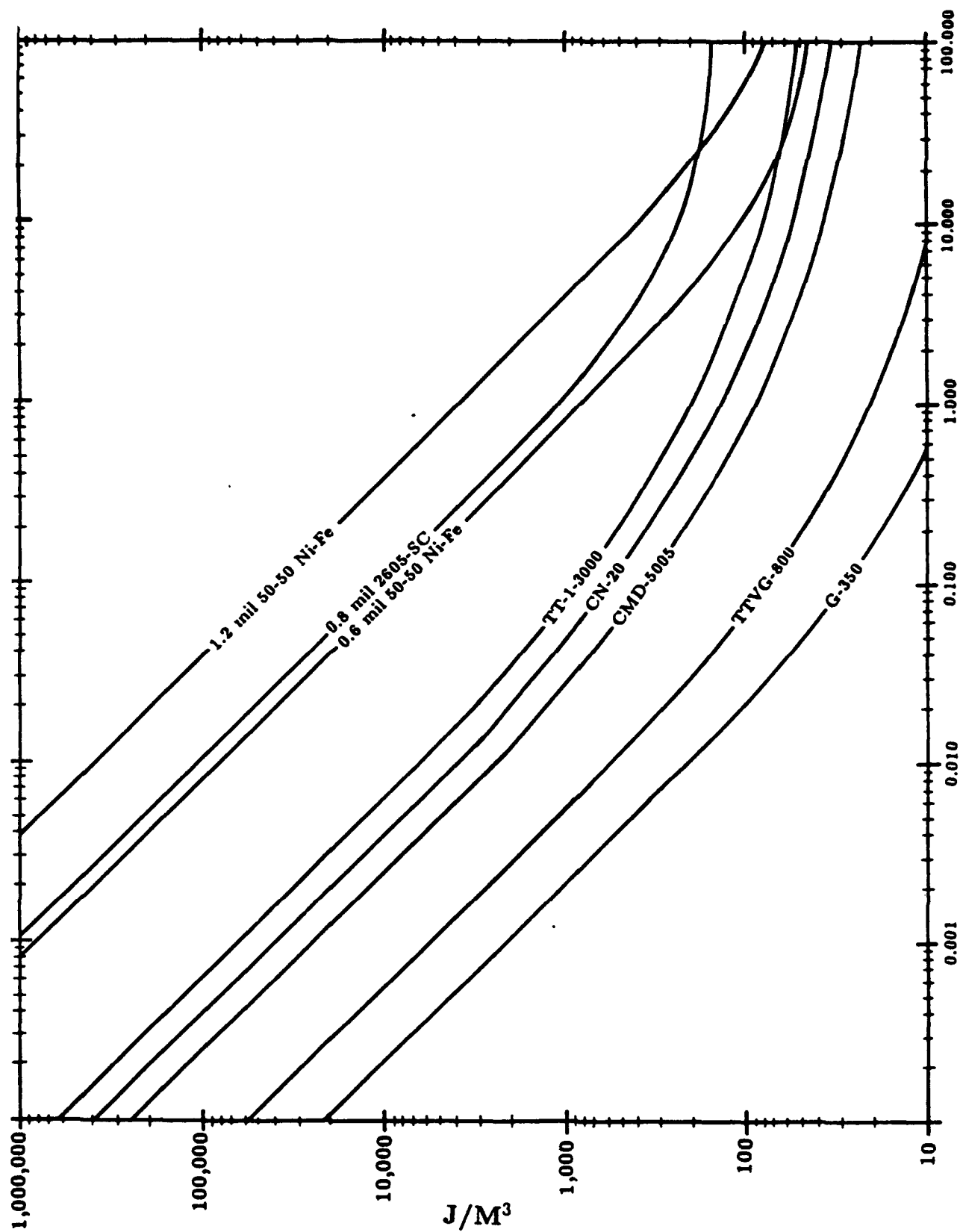


Figure 2.25: Square Wave Saturation Time (μsec)

saturation times become dominated by eddy current losses which also scale inversely linear with saturation time.

An important figure of merit for the design of nonlinear magnetic pulse compressors is the quantity $\% \text{Energy Lost} / \text{Gain}^2$ plotted as function of material and saturation time in Fig. 2.26. The core volume required to achieve a given temporal compression factor with a stage of magnetic compression scales linearly as the square of the gain and inversely as the square of the available flux swing (packing factor $\times \Delta B$). The predicted efficiency can be readily derived from Fig. 2.26 by simply choosing the optimum material, desired gain and saturation time.

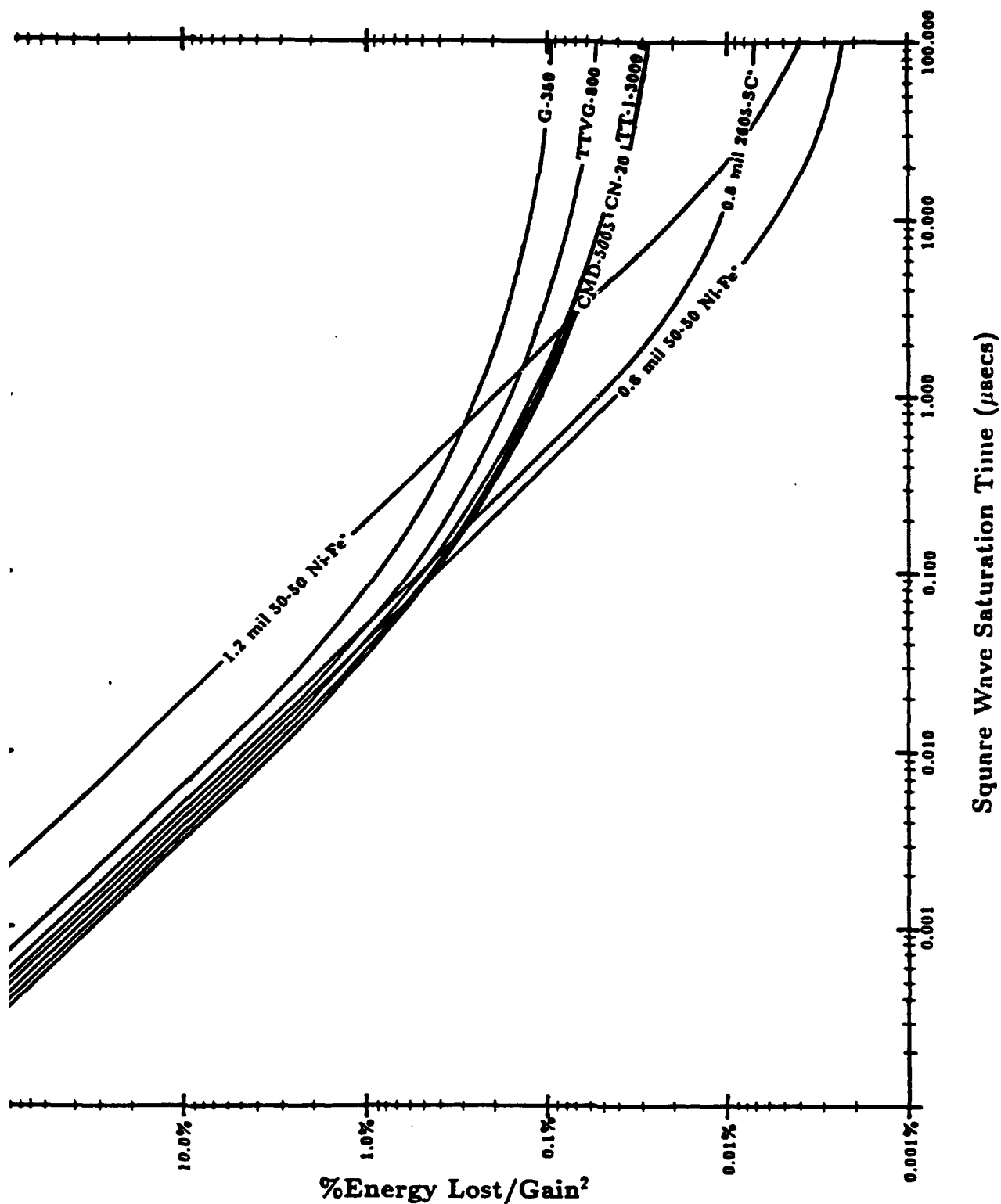


Figure 2.26: *Packing Factor = 0.7 Assumed, Unity Packing Factor Assumed for all Ferrites

APPENDIX 3

SCR SELECTION

Understanding the loss mechanisms in SCRs is important in establishing the operating limitations for these devices. If a simple model is assumed where the usable area of the device is a function of the time interval between triggering ($t = 0$) and device turn-on ($t = t_0$), then for an interdigitized gate structure the active area would be given by

$$A(t) = A_0 \cdot \frac{t}{t_0} \quad t < t_0$$

$$A(t) = A_0 \quad t > t_0$$

For a center-fire gate structure the time dependence of the conducting area should be

$$A(t) = A_0 \cdot \left(\frac{t}{t_0}\right)^2 \quad t < t_0$$

$$A(t) = A_0 \quad t > t_0$$

where A_0 is the total junction area and $A(t)$ is the time dependent region which is fully conductive.

The energy dissipated per pulse will be given by

$$\text{Energy} = \int_0^\tau I^2(t) \cdot R(t) dt$$

where τ is the pulse length and $R(t)$ is the time-varying resistance of the junction. According to this simple model

$$R(t) = R_0 \cdot \frac{A_0}{A(t)}$$

If a current waveform having a sinusoidal time dependence is assumed, then for $t_0 \ll \tau$

$$\text{Energy Loss} = I_0^2 R_0 \cdot \left(\frac{\pi^2 t_0^3}{6\tau^2} + \frac{\tau}{2} \right) \quad A(t) = A_0 \left(\frac{t}{t_0} \right)$$

$$\text{Energy Loss} = I_0^2 R_0 \cdot \left(\frac{2\pi^2 t_0^3}{3\tau^2} + \frac{\tau}{2} \right) \quad A(t) = A_0 \left(\frac{t}{t_0} \right)^2$$

We can therefore define a predicted dynamic resistance given by

$$R(\tau) = R_0 \left[1 + \text{const} \cdot \left(\frac{t_0}{\tau} \right)^3 \right]$$

This predicted energy loss does not adequately describe the experienced time-dependent behavior of SCRs. Immediately following turn-on ($< 1 \mu\text{sec}$), this time dependence may be present, but use of a saturable magnetic assist limits the peak current during this interval to such a low

value that little energy is dissipated. Analyses of experimentally-measured time dependent losses in such circuits indicates a behavior given approximately by

$$R = R_0 \left[1 + \frac{\text{const}}{I_0} \cdot \left(\frac{dI}{dt} \right) \right]$$

This would indicate that to first order the actual device turn-on losses are not adequately described by a model where the conduction area is time dependent but rather by a model in which the whole device requires time to react to changing currents. This suggests that so long as the limiting dI/dt is not exceeded (which might result in excessive voltage drops followed by electrical breakdown), the energy absorbed due to rising conduction currents is most likely distributed throughout the device.

It appears that the diffusion of minority carriers across the junction is the dominant loss mechanism. This means that even after an SCR has been conducting low level current indefinitely, dI/dt losses will still be associated with an increase in current. This mechanism also explains why the reverse recovered charge during turn-off is such a strong function of the dI/dt . Saturable inductors to limit turn-on currents will only help if they reduce the current during the first microsecond or so when the conduction area is still expanding.

It is also easy to explain why the voltage drop across the device increases faster than linearly with dI/dt for pulse lengths approaching the carrier lifetime. Rapid fluctuations in the current cause rapid carrier concentration variations at the junction with very little effect on the concentrations far from the junction. This results in a decrease in the effective diffusion capacitance. For sinusoidal waveforms it can be shown that the effective junction diffusion capacitance defined as $C_d = dQ/dV$ is given by

$$C_d = (1/2)\tau(dI/dV) \quad \omega\tau \ll 1$$

$$C_d = \left(\frac{\tau}{2\omega} \right)^{1/2} (dI/dV) \quad \omega\tau \gg 1$$

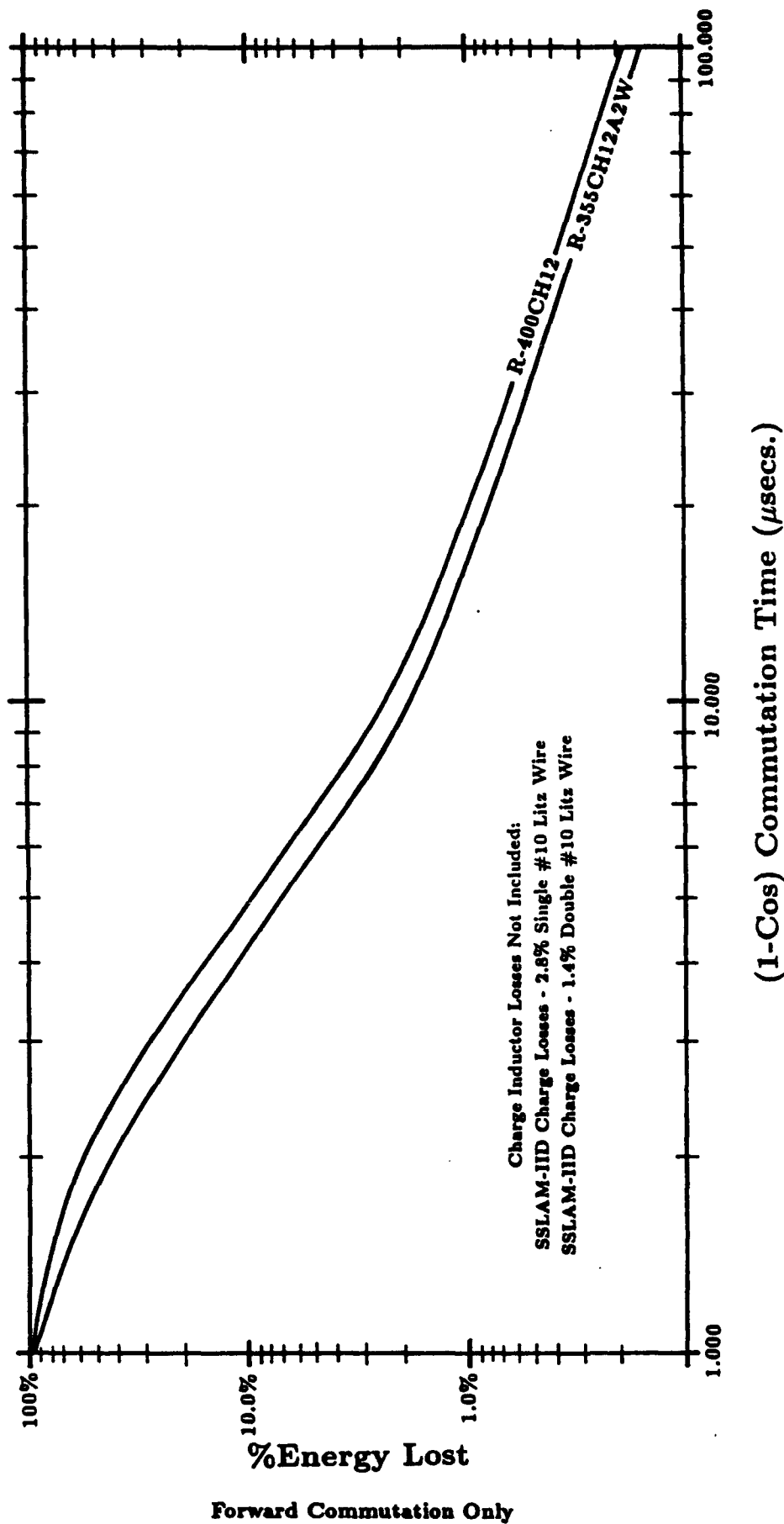
After reviewing the test data accumulated in an intensive effort by Ed Cook at LLNL, it appeared redundant to establish our own SCR test stand. Instead, candidate devices whose performance had been thoroughly documented were installed at different times into the modified SNOMAD-I driver. Performance data was collected under actual operating conditions with SNOMAD-I driving a copper vapor laser at full power. Since devices with different case and wafer sizes were tested, in some cases several devices (≤ 4) were installed in an isolated parallel fashion.

The wide variation in performance indicated in the manufacturers specifications is somewhat deceiving. The maximum RMS current is predominantly determined by the wafer area while the peak operating voltage is determined by the wafer thickness. The recovery times are determined primarily by the carrier lifetime and the junction diffusion capacitance. The recovery times can be decreased by decreasing the carrier lifetime but at the expense of slightly increased conduction losses.

In summary all of the devices are based on silicon, use similar doping levels, and have similar gate interdigitation levels. All the manufacturers listed sell SCRs with similar operating voltages, RMS current levels, and dI/dt capability. Choosing a device with a lower RMS current rating will require the designer to parallel several devices. The selection of an appropriate SCR is straightforward and, for a given operating envelope, if the appropriate device from one manufacturer fails, it is likely that an equivalent device from any of the other manufacturers will be at least stressed very close to its limit in the same socket.

Recently we have converged on two devices supplied by the same manufacturer, WestCode Semiconductor. These are both 1200 volt devices with average current ratings of ≈ 1.0 kiloamperes.

The device designated R-400C will handle slightly more I^2t but is somewhat slower to recover and conversely to turn on than the rival R-355C. This is documented in more detail by Figure 3.1 which graphs energy lost versus commutation time for these devices. These two devices are most certainly not the only devices which could have been chosen but represent a soft optimum point on a curve of cost versus performance.



(8 μ fds/SCR, 1000 Volts, 1.5 μ sec Sat. Assist)

Figure 3.1

APPENDIX 4

CAPACITOR SELECTION

As reliability and performance continues to improve, components which initially could be neglected begin to impact the overall reliability. Capacitors are a good example of this phenomenon. Present requirements for low loss operation at 10 kHz reliably and continuously for years eliminates most energy storage media. Mylar, the most common storage medium for pulsed power applications at low duty factors, must be eliminated because of its high loss tangent. Polycarbonate and reconstituted mica also are unusable for this reason.

Aluminized polypropylene with interleaved aluminum foil conductors fully extended appears to be the best dielectric material for the low voltage front end. Strontium titanate ceramic capacitors demonstrate a similar loss tangent and would be used in the front end of the pulser if fabrication in thin sheets were not so difficult. They are an excellent choice at voltages in excess of 20 kV where they can be fabricated as disks.

Candidate polypropylene capacitors are available from several manufacturers. Rhoderstein, WIMA, ByCap, GE, Sprague, and Maxwell are examples. WIMA presents a product line which extends to 2 kV operating voltage and is suitable for operation at CW repetition rates in excess of 100 kHz. Strontium titanate capacitors are only available from TDK and Murriata-Erie. TDK is the most common supplier and manufactures devices in the range of 20-50 kV. Parameters for the various candidate dielectric materials appear in Table 4.1.

The loss tangent of capacitors is also a strong function of the charge and discharge time. The best choice for a capacitor operating at 1.0 μ sec time scales is not necessarily still the best choice at 10 nanosecond charge or discharge times. In most cases the losses will continue to increase as the charging time is reduced until the loss tangent approaches unity and the capacitor becomes a resistor. This time scale is simply determined by multiplying the ESR (Equivalent Series Resistance) by the capacitance value. The result is an RC time which represents the ultimate high frequency limit of this capacitor. This time scale is usually independent of the size of the individual capacitor and depends primarily on the dielectric media and construction technique. This is further documented in Table 4.2. Here the ESR was measured for an extensive collection of capacitors. It is easily noticeable that the limiting charge time ($ESR \cdot C$) is relatively independent of capacitance and primarily dependent on capacitor type. Taking this into account we have plotted the predicted energy loss for a single charge/discharge cycle for various types of capacitors in Figure 4.1.

Table 4.1: The Essential Characteristics of the Plastic Film Dielectrics Used

Physical characteristics of the film	Polyester	Polycarbonate	Polypropylene	SrTiO ₂	Reconstituted Mica
Dielectric constant 1 kHz/23 °C	3.3 (positive as temp. rises)	2.8 (largely constant over temp. range)	2.2 (negative as temp. rises)	~ 5000	
Dielectric loss factor tan δ/23 °C	1 kHz 10 kHz 100 kHz 1 MHz 5 x 10 ⁻³ 11 x 10 ⁻³ 18 x 10 ⁻³ 20 x 10 ⁻³	1.5 x 10 ⁻³ 5 x 10 ⁻³ 10 x 10 ⁻³ 10 x 10 ⁻³	1 x 10 ⁻⁴ 1 x 10 ⁻⁴ 1 x 10 ⁻⁴ 1 x 10 ⁻³	< 0.1 %	0.5 %
Specific volume resistance Ω x cm/23 °C	10 ¹⁸	2 x 10 ¹⁷	6 x 10 ¹⁸	> 10 ¹²	6 x 10 ¹⁷
Dielectric strength in V/μm at 23 °C	580 V-	535 V-	650 V-	> 10	
Preferred temperature range	-55....+ 100 °C	-55....+ 100 °C	-55....+ 85 °C	-30....+ 85 °C	-65....+ 125 °C
Dielectric absorption ln % at 23 °C	0.20....0.25	0.12....0.25	0.05....0.10	< 0.1 %	0.5 %
Energy Density	12.7 kJ/ m ³	9.5 kJ/ m ³	5.4 kJ/ m ³	15 kJ/ m ³	15 kJ/ m ³

4300000
ver 4.00 010

Table 4.2: Capacitor Performance Specifications

Capacitor Type	ESR
RHOED. 100pf 1600V FKP	150 m Ω
RHOED. 220pf 1600V FKP	60 m Ω
RHOED. 680pf 1600V FKP	35 m Ω
ROYAL MICA .01 μ fd 5000V MKP	54 m Ω
RHOED. .01 μ fd 400V MKP	58.5 m Ω
SPRAG .022 μ fd 1600V MKP	39 m Ω
RHOED .047 μ fd 2000V MKP	47 m Ω
MALLORY .05 μ fd 1600V FKP	31.5 m Ω
RHOED. .1 μ fd 600V MKP	30.5 m Ω
BYCAP .1 μ fd 1000V FKP	17 m Ω
RHOED .1 μ fd 1600V FKP	21 m Ω
WIMA .1 μ fd 1600V FKP	20 m Ω
RHOED .1 μ fd 2000V FKP AXIAL LEAD	24 m Ω
WIMA .1 μ fd 2000V MKP	40 m Ω
ROYAL MICA .125 μ fd 1000V	22.5 m Ω
WIMA .15 μ fd 1250V FKP	15 m Ω
RHOED .22 μ fd 160V MKP	22.5 m Ω
RHOED .22 μ fd 1600V MKP	25 m Ω
RHOED .22 μ fd 1000V FKP AXIAL	22.5 m Ω
WIMA .22 μ fd 1250V MKP	12 m Ω
WIMA .22 μ fd 1000V MKP	28 m Ω
BYCAP .25 μ fd 1000V FKP	14.3 m Ω
BYCAP .5 μ fd 1000V FKP	9.3 m Ω
BYCAP 1.0 μ fd 1000V FKP	8.3 m Ω
STANLEY R.M. 1.0 μ fd 1000V	13 m Ω
WIMA 1.5 μ fd 400V MKP	9 m Ω
SPRAG 2.0 μ fd 200V MKP	26 m Ω
RHOED. 2.2 μ fd 400V MKT	19 m Ω
SPRAG 2.5 μ fd 200V MKP	20.5 m Ω
SPRAG 3.0 μ fd 200V MKP	17.5 m Ω

Table 4.2: Capacitor Performance Specifications (Continued)

Capacitor Type	ESR
BAR. TIT. 50pf 6kV	9300 m Ω
BAR. TIT. 100pf 6kV	7500 m Ω
BAR. TIT. 480pf 6kV	1600 m Ω
COND PROD 200pf 30kV	465 m Ω
TDK 560pf 50kV	820 m Ω
TDK 1000pf 50kV	500 m Ω
TDK 1400pf 20kV	358 m Ω
TDK 1700pf 30kV	311 m Ω
TDK 1700pf 50kV	318 m Ω
TDK 2500pf 20kV	231 m Ω
MUR ER 2700pf 30kV	266 m Ω
KD STRON. TIT. 10,000pf 7.5kV	172 m Ω

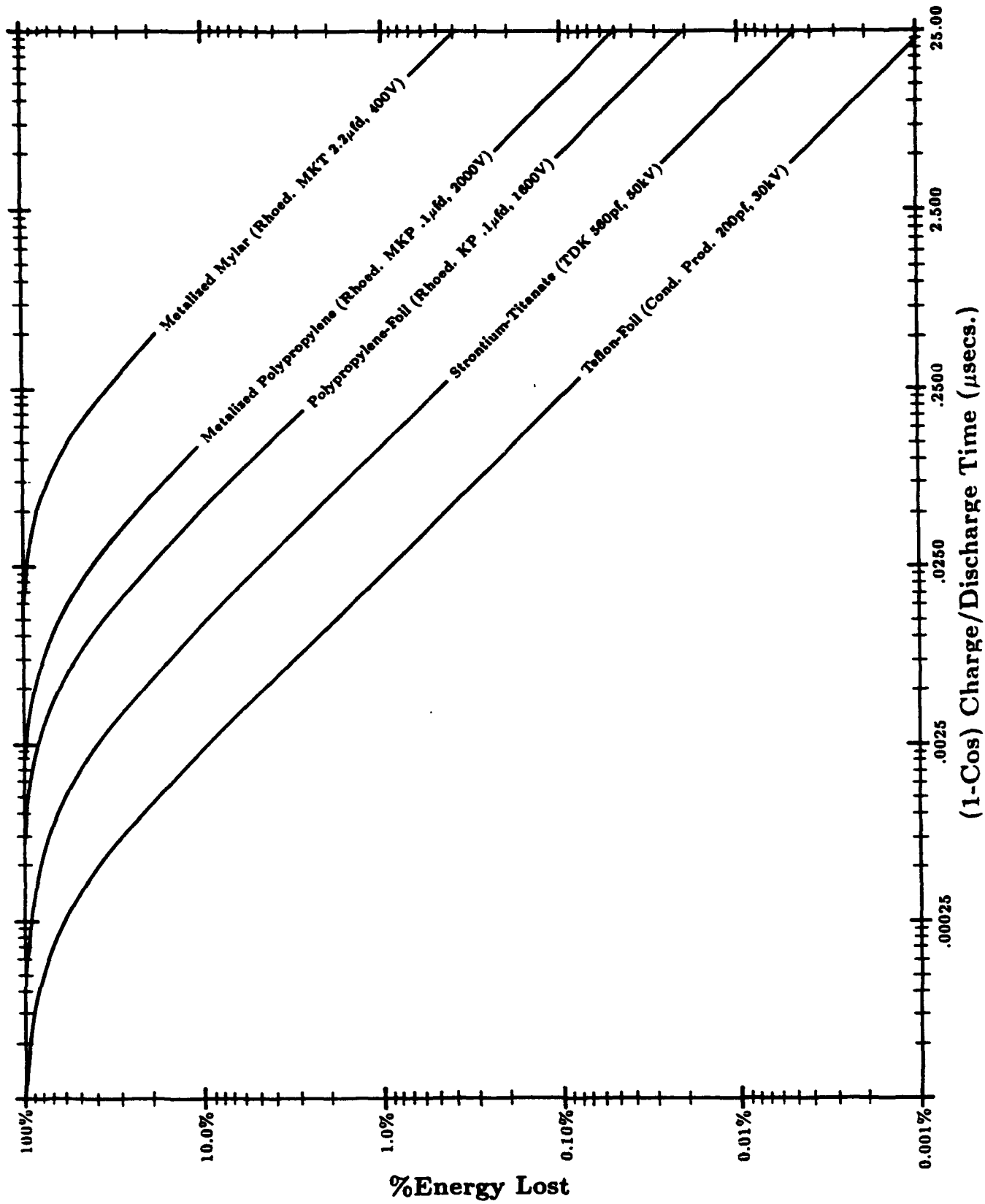


Figure 4.1: Capacitor Losses Versus Discharge Time

APPENDIX 5

TRANSFORMER DESIGN

The high performance transformer design used in all of the nonlinear magnetic pulse compressors is an advanced hybrid transformer developed by SRL. This transformer combines the advantages of conventional multiple turn transformers with the unique properties of an induction accelerator. This makes pulse transformers with extremely low leakage inductance and high step-up ratios a reality.

In conventional magnetic pulse compressor design, transformers are frequently interleaved with compression stages. When the operating impedance becomes difficult to handle, a transformer is used to change the value to an optimum impedance. This avoids compression reactors with thousands of turns or a fractional turn. In high performance magnetic switches which operate on submicrosecond time scales, these transformers must be carefully designed as continuous transmission lines. Great care is taken to both confine the leakage magnetic fields and simultaneously to avoid breakdown level electric fields.

Step-up transformers can be constructed by either using multiple secondary turns, using fractional numbers of primary turns, or any combination thereof. At first, the concept of fractional primary turns may seem somewhat foreign but it is the basis of all induction linacs where forcing the electron beam to make several secondary turns would be very difficult.

An equivalent circuit for a transformer using a fractional turn primary appears in Fig. 5.1. A simplified cross-sectional view appears in Fig. 5.2. Here multiple primary windings are all fed in parallel while the secondary is a single turn formed by the series connection of the same windings. The equivalent circuit for the more conventional multiple secondary turn transformer appears in Fig. 5.3, while a simplified cross-section is shown in Fig. 5.4. Here a single high permeability core is used for isolation and the secondary makes multiple passes around the core adding on the primary voltage with each pass.

In the case of either transformer it is extremely important to understand where currents are flowing and in which regions the magnetic fields are confined. An example is presented in Fig. 5.5. Here the regions occupied by the magnetic fields has been shaded. We will assume that the permeability of the magnetic core is infinite and therefore the shunt inductance is infinite and no net current flows around the core. In order for the currents to exactly cancel, the ratios of the currents in the primary and secondary are equal to the ratio of the number of turns. This can be understood more intuitively by thinking of the primary transmission line as feeding into the secondary transmission lines all in parallel.

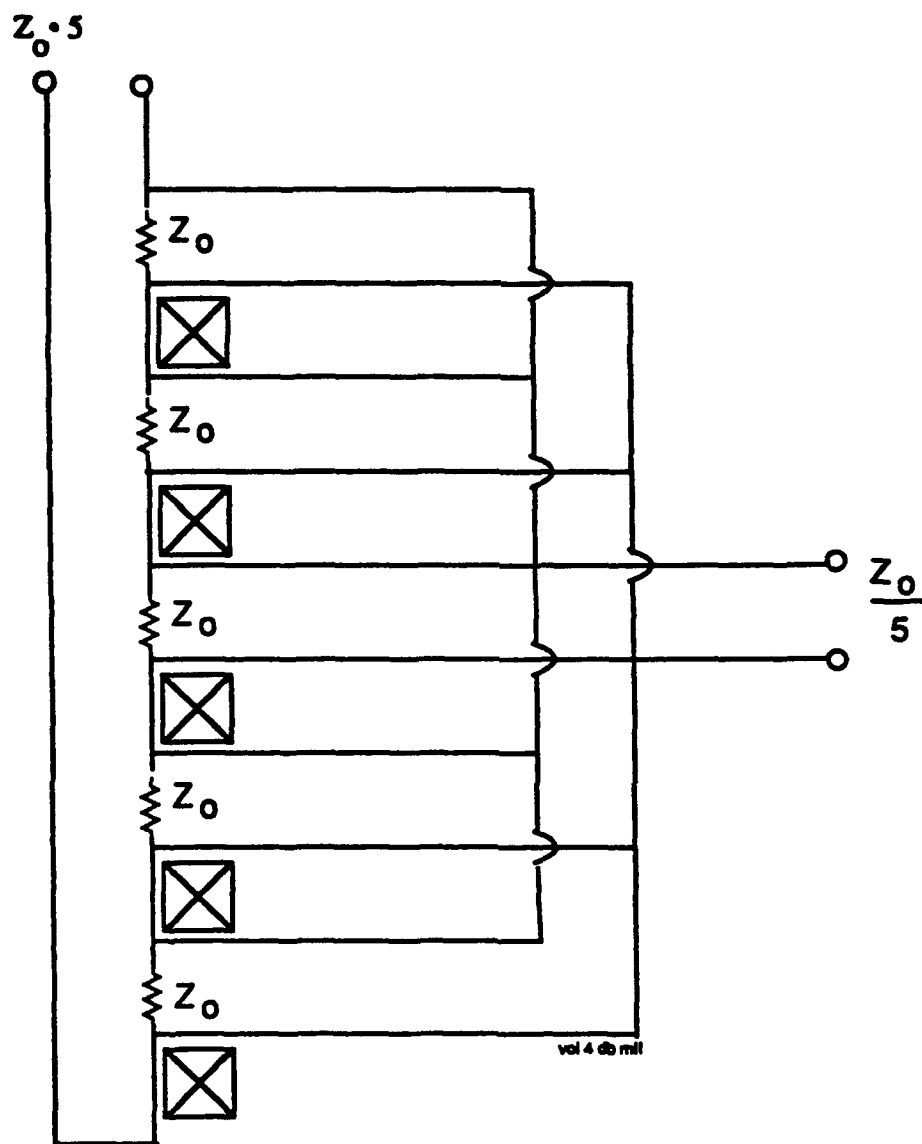


Figure 5.1: Equivalent circuit of induction style transformer

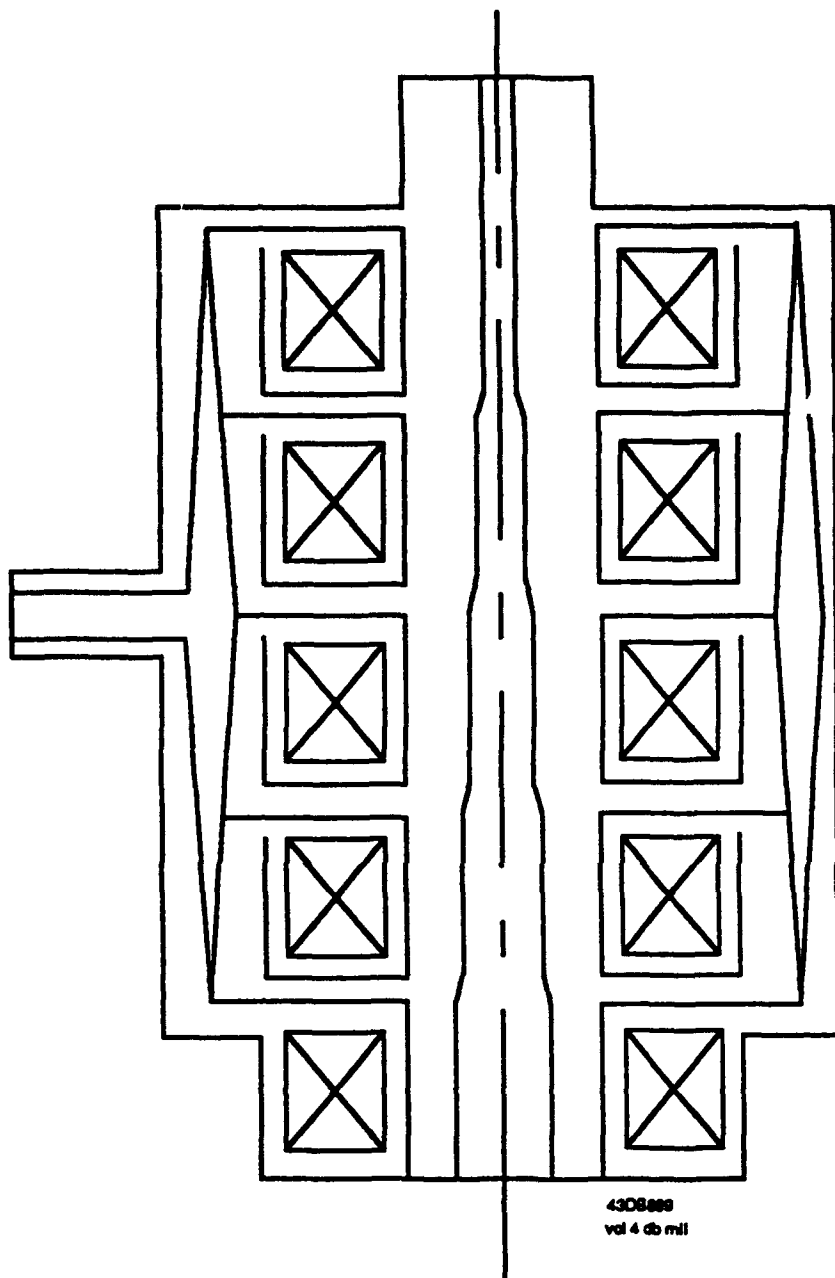


Figure 5.2: Simplified fractional turn primary transformer

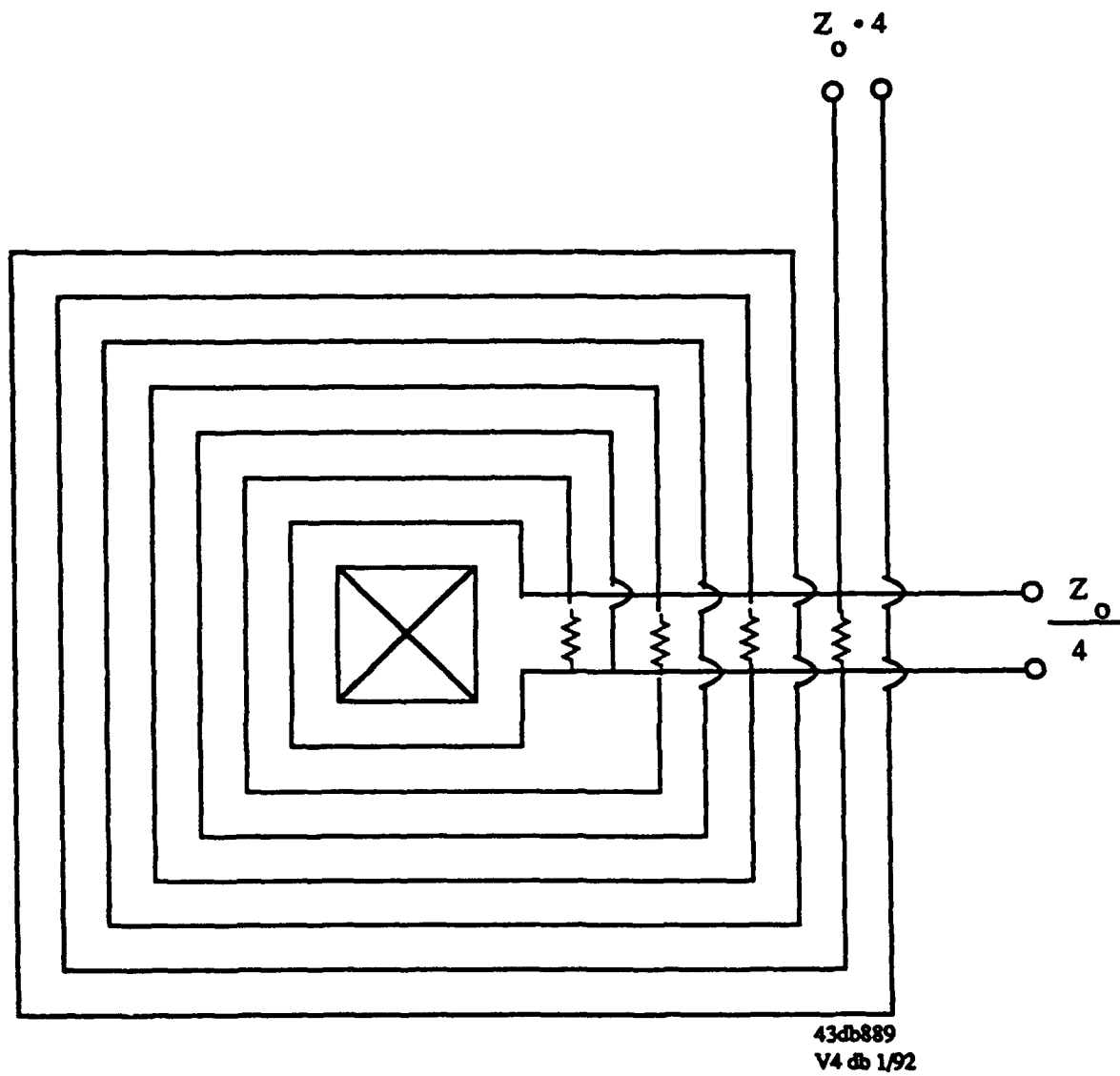


Figure 5.3: Equivalent circuit of multiple turn secondary transformer

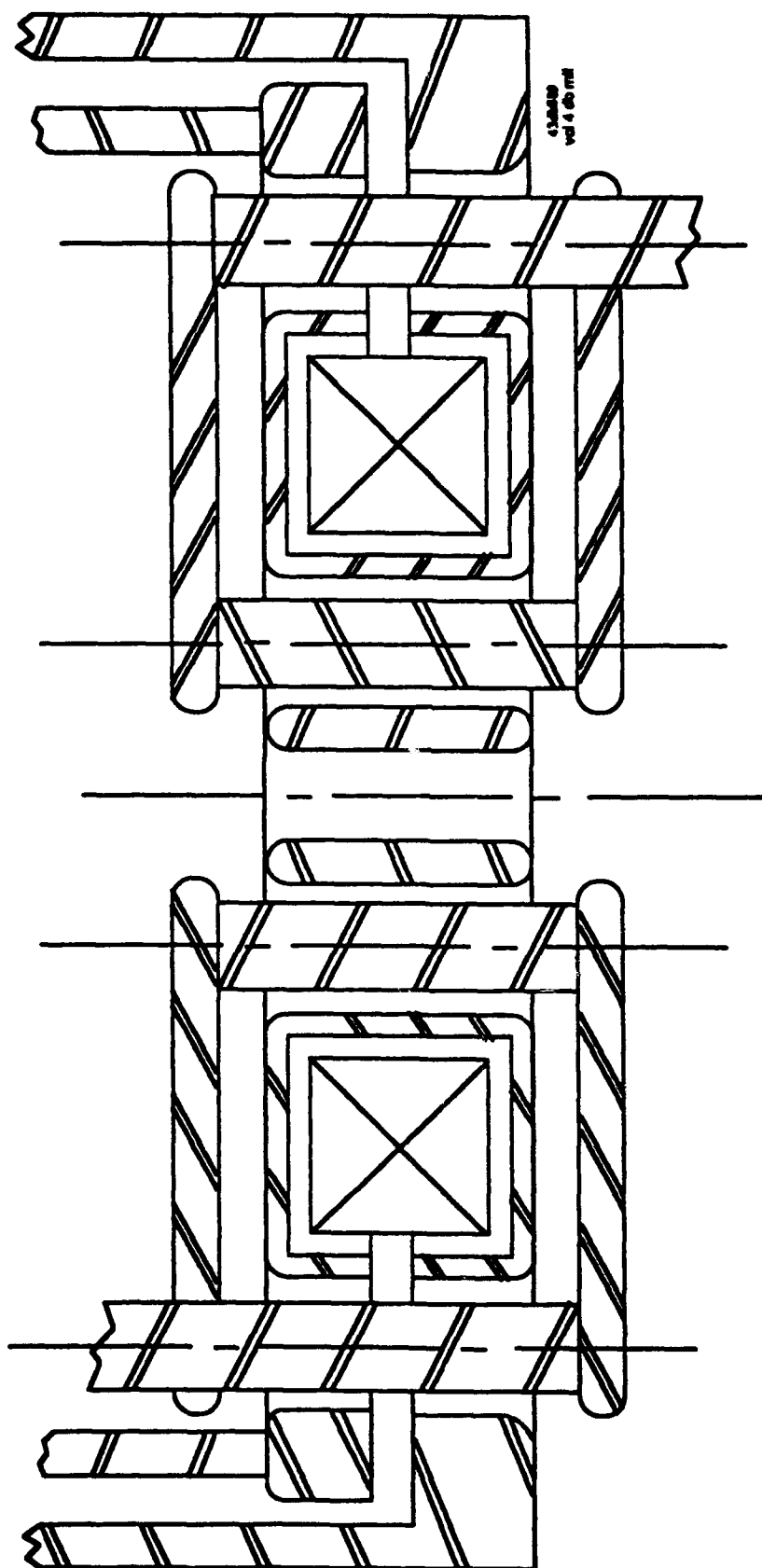


Figure 5.4: Simplified multiple turn secondary transformer

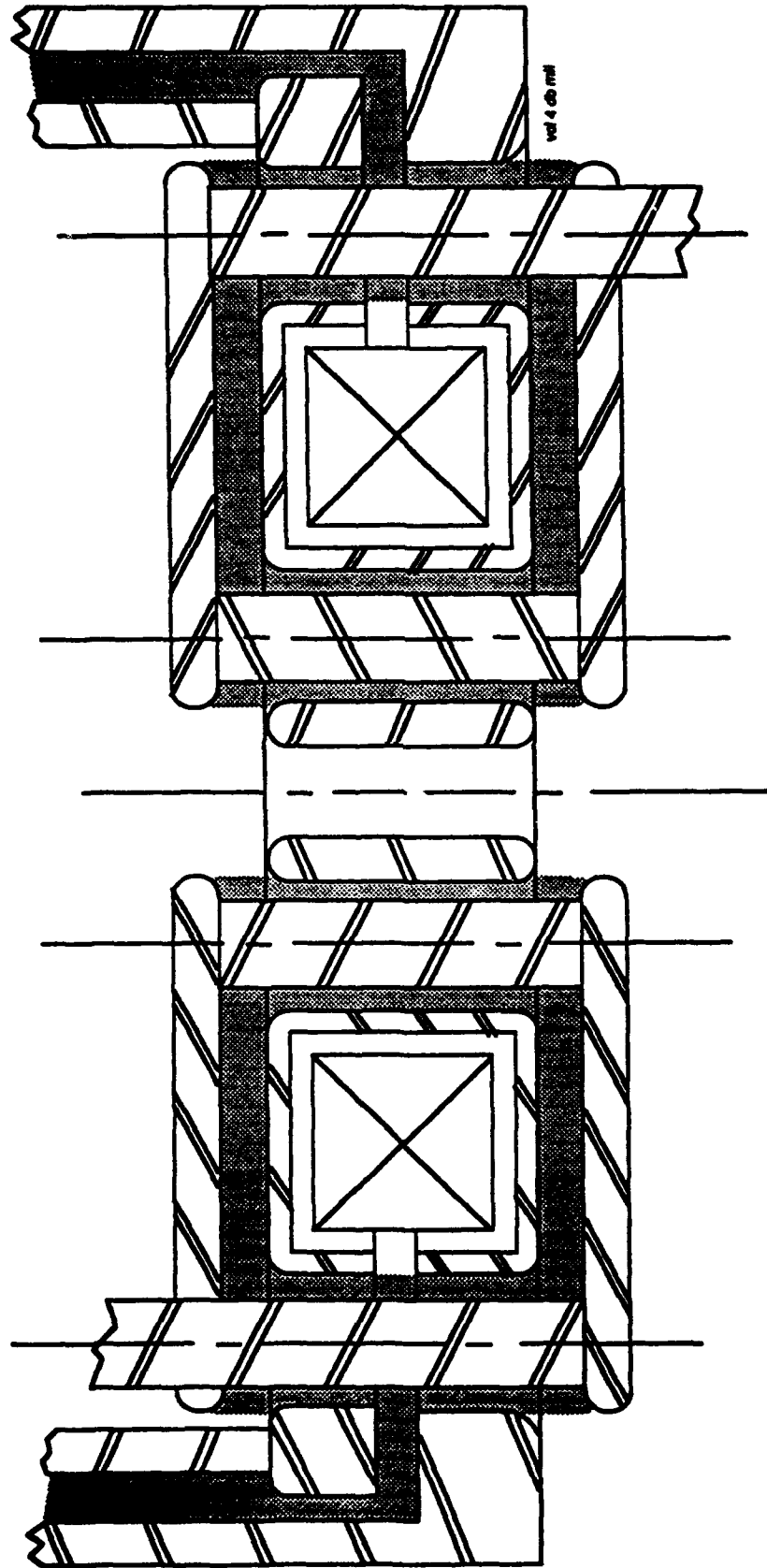


Figure 5.5: Simplified multiple turn secondary transformer with volume occupied by leakage field shown shaded

APPENDIX 6

NONLINEAR MAGNETIC COMPRESSORS

The concept of using saturable reactors as a basis of high power pulse generators is not a new concept and certainly not invented by the authors, but there have been few recent applications of this technology. Perhaps the authors rather than inventing this idea have helped to find it a home.

The use of saturable reactors for high power pulse generation was first described by Melville in 1951. At that time output powers levels as high as a megawatt were being sought for Radar applications. There were no SCRs at the time and thyratrons were rapidly developed to the point where they could deliver these power levels routinely and the idea of nonlinear magnetic pulse compression simply disappeared. The development of induction linear accelerators and discharge lasers requiring gigawatts of input power revived this old technology.

The basic principle underlying nonlinear magnetic driver operation involves using a saturable core as an inductor in a resonant circuit. The circuit is designed to allow the core of the next stage to saturate before a significant fraction of the energy stored in the capacitors of the previous stage is transferred. This nonlinear saturation phenomenon shifts the resonant frequency of this resonant circuit by the square root of the permeability shift as the core saturates. These stages are typically cascaded (Fig. 6.1) and energy is coupled faster and faster from one stage to the next. These circuits are efficient at transferring power in both directions since they act not only to upshift the frequency in the forward direction thereby providing temporal compression, but also downshift the frequency of a voltage pulse as it cascades back up the chain in the reverse direction. The energy which reflects from the mismatched load can be saved and applied to the next pulse.

In the remainder of the section we present a more quantitative description of the compression chain operation. The analyses is based on saturable inductors with toroidal geometries, and for the sake of clarity several simplifying approximations have been introduced. All circuit components will be assumed lossless and all extraneous inductances ignored. Also the expression for saturated inductance will assume that the area enclosed by the turns is simply the core cross-sectional area, while in practice the packing factor must be properly calculated.

Saturation of an inductor occurs when the magnetic field in the inductor core reaches the saturation magnetization. This assumes of course that the core material is ferri- or ferromagnetic material. Saturation is measurable as a large incremental change in the material permeability.

According to Maxwell,

$$\int E \cdot dl = V_L = N \frac{\partial \Phi}{\partial t} = NA \frac{\partial B}{\partial t}$$

$$\int V_L dt = NA \Delta B$$

and if the core has been reset

$$\int_0^{\tau_{sat}} V_L dt = NA(-(-B_r) + B_s) = NA \Delta B_s$$

where N is the number of turns around the core, A is the area of the core, and B_r (B_s) the remanent (saturating) magnetic field.

If we make all of the capacitance values in the compression chain equal to C_0 , then for a capacitor preceded in the chain by L_{n-1} and followed by L_n the time required to charge the next

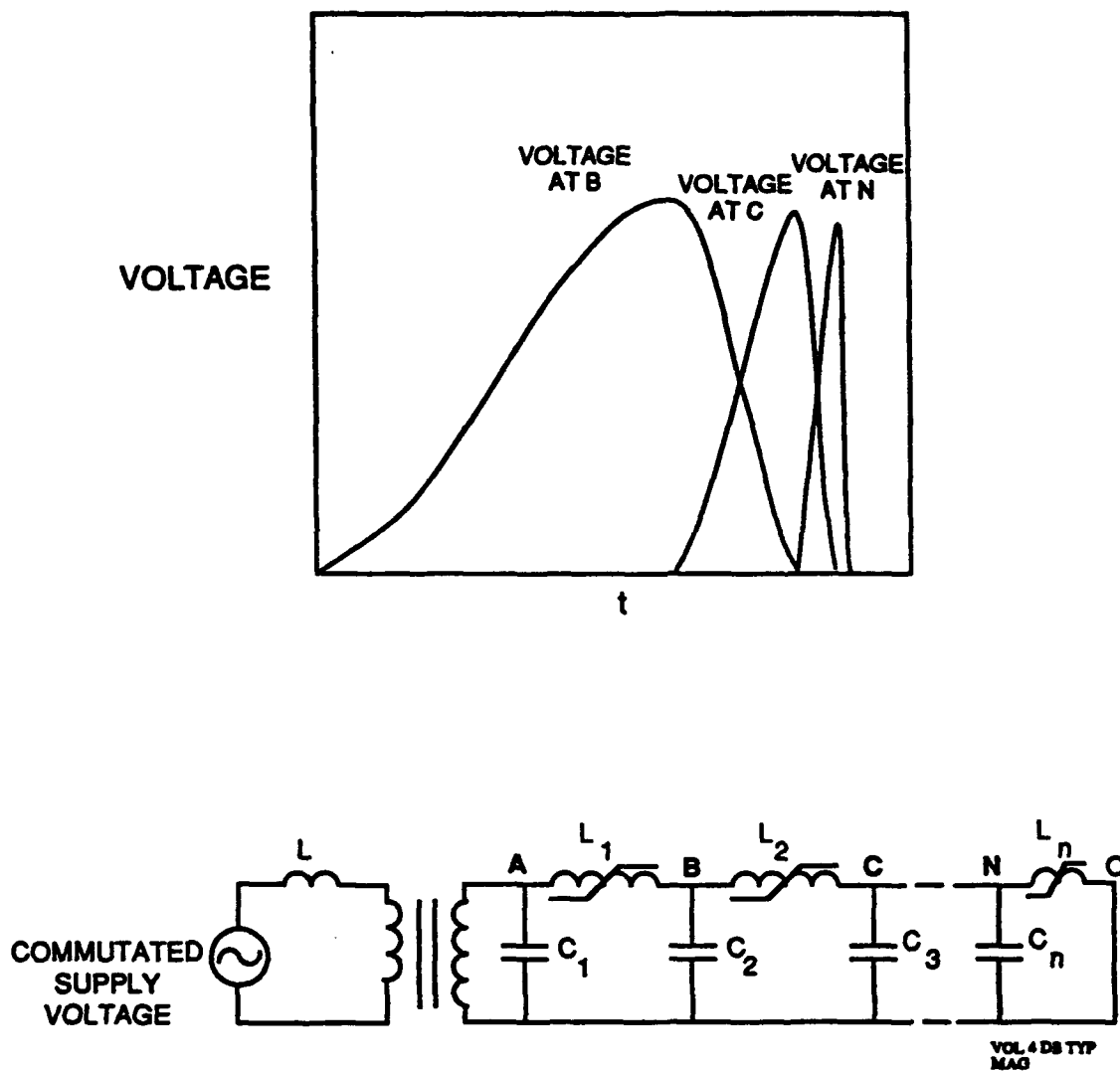


Figure 6.1: Typical magnetic switch operation

capacitor in line after inductor L_{n-1} saturates is given by

$$\tau_{charge}^{C_n} = \tau_{discharge}^{C_{n-1}} = \pi \left(L_{n-1}^{sat} \cdot \frac{C_{n-1} C_n}{C_{n-1} + C_n} \right)^{1/2} = \pi \left(\frac{L_{n-1}^{sat} \cdot C_0}{2} \right)^{1/2}$$

The time required to charge capacitor C_n should be designed to be approximately equal to the time to reach B_{sat} in inductor L_n . Therefore

$$\tau_{sat}^{L_n} \approx \tau_{charge}^{C_n} = \frac{\Delta B_s N_n A_n}{\bar{V}_c}$$

Ideally

$$\bar{V}_c = V_{C_0} \int_0^{\pi/\omega} \frac{(1 - \cos \omega \tau)}{2} dt = \frac{V_{C_0}}{2}$$

therefore

$$\tau_{charge}^{C_n} \approx \frac{2 \Delta B_s}{V_{C_0}} N_n A_n$$

where V_{C_0} is the peak charge voltage of capacitor C_n . After inductor L_n saturates we find:

$$L_n = \frac{\mu_n^{sat}}{2} w_n N_n^2 \ln \left(\frac{R_{0n}}{R_{in}} \right) \approx \frac{\mu_n^{sat} N_n^2 A_n}{2\pi \bar{R}} \approx \frac{\mu_n^{sat} N_n^2 A_n}{\text{volume}}$$

Where w_n is the axial width of the toroid $R_{0n}(R_{in})$ the core outer (inner) radius. It also follows that if the core saturates at the peak of the charging waveform then

$$L_{n-1}^{sat} = \frac{2}{C_0} \left(\frac{2 \Delta B_s N_n A_n}{\pi^2 V_c} \right)^2$$

and

$$\frac{L_n^{sat}}{L_{n-1}^{sat}} \approx \frac{\mu_n^{sat} \pi^2}{\text{volume}_n} \cdot \frac{\left(\frac{C_0 V_c^2}{2} \right)}{4 \Delta B_s^2} \approx \frac{\text{energy}}{\text{volume}_n} \left(\frac{\mu_n^{sat} \pi^2}{4 \Delta B_s^2} \right)$$

since

$$\text{gain} = \frac{\tau_{charge}^{C_n}}{\tau_{charge}^{C_{n+1}}} = \left(\frac{L_n^{sat}}{L_{n+1}^{sat}} \right)^{1/2}$$

The core volume requirement to produce a given temporal compression and corresponding energy gain is given by

$$\text{volume}_n = \text{gain}^2 \text{energy} \left(\frac{\mu_n^{sat} \pi^2}{4 \Delta B_s^2} \right)$$

In practice not all of the fields are confined to the core and if we define the packing factor pf to be the ratio of the inductance calculated by assuming all of the magnetic field energy is stored

in an ideal saturated toroid to the actual measured saturated inductance then our core volume requirement can be rewritten as

$$\text{volume} = \text{gain}^2 \cdot \text{Pulse Energy} \cdot \left(\frac{\mu_0 \cdot \pi^2}{4 \cdot (\Delta B_s \cdot pf)^2} \right)$$

The packing factor is defined as

$$pf = \frac{\int_{V_f} H^2 dv}{\int_{\text{all space}} H^2 dv}$$

where V_f is the actual volume occupied by the ferri- (ferro) magnetic core material excluding all interlaminar insulation and voids. Optimization of this packing factor is crucial in magnetic switch design and is accomplished by enclosing the core in a tightly fitting conducting housing. The multiple turns are formed as coaxial transmission lines which pass through this housing. Circulating currents set up in this housing exclude the magnetic flux and contain it in the desired volumes.

With the saturable material completely enclosed in conducting coaxial housings, the voltage per turn associated with the dB/dt of the core appears across a single narrow gap on the outside diameter of each housing. Connecting the coaxial transmission lines in the inner and outer housings with radial transmission lines across the top and bottom of the core completes the turns. The impedances of these transmission lines are adjusted so that

$$Z_{LINE} \approx \sqrt{\frac{2 \cdot L_{sat}}{C}}$$

while simultaneously every effort is made to minimize $L_{sat} \cdot C$ which is proportional to the square of the pulse length. Here L_{sat} and C refer to the saturated inductance of the reactor and the value of the storage capacitance respectively.

It is important in the design of a compression stage that a minimum of excess core volume is employed as the losses are linearly proportional to the core volume. In a properly designed core μ_n^{sat} is close to μ_0 and a curve is provided in Fig. 6.2 for the purpose of fine tuning a design.

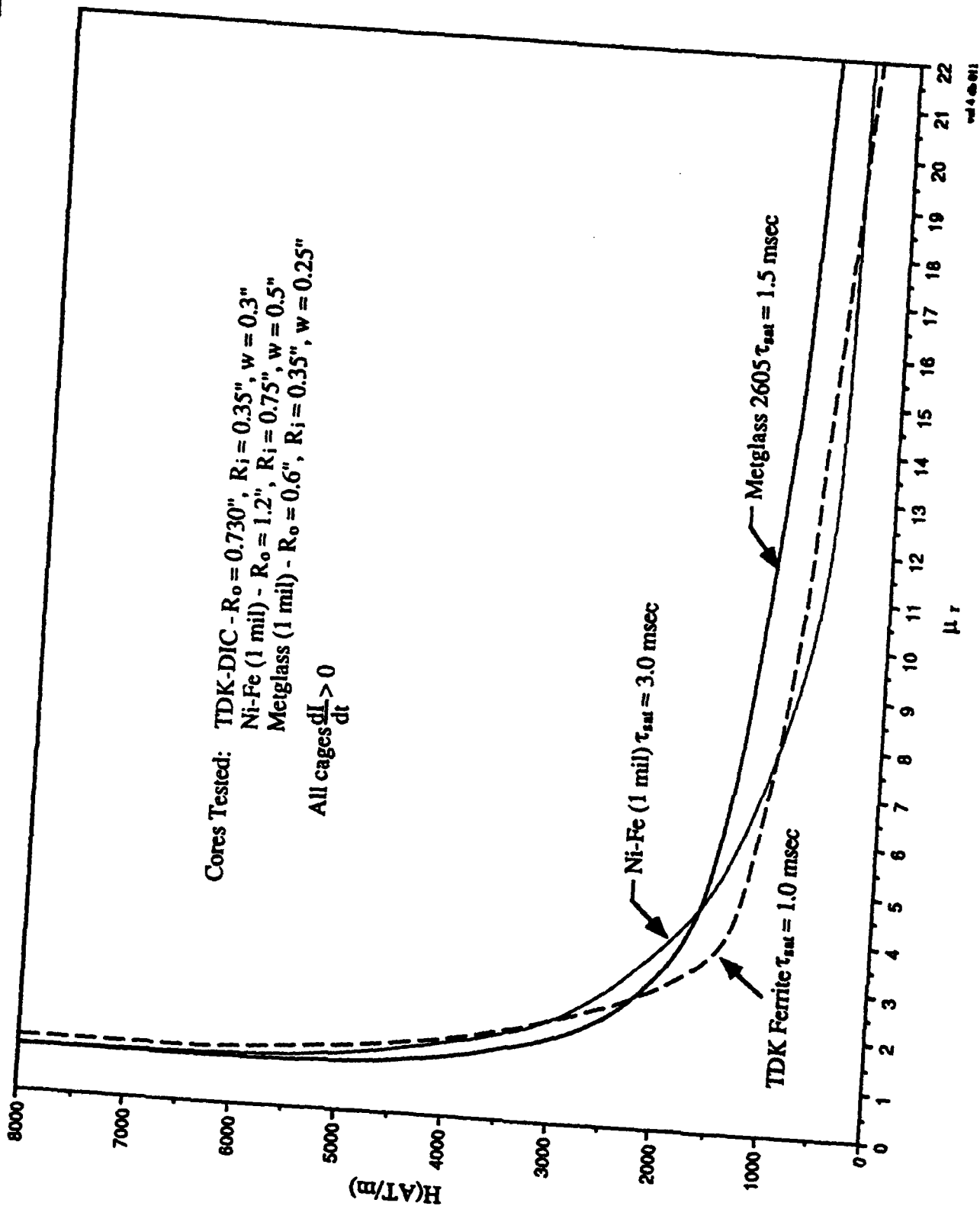


Figure 6.2

APPENDIX 7

Charging and Control Systems

Command Resonant Charge (CRC) systems are a common interface between any repetitive pulse power system and a DC supply. The job of a CRC is to deliver a preset quantity of energy to the intermediate storage units between pulses. The CRC provides a technique for pulse charging without the 50% energy loss associated with resistance charging.

The Charging Module

The charge module bears the responsibility of charging the intermediate storage capacitor in each commutator module to a predetermined voltage between output pulses. It was also acquire the reflected energy from the laser and add it to the energy required for the next pulse immediately following each laser discharge cycle.

The charge module must provide the same voltage on the intermediate storage capacitor for each succeeding pulse independent of power supply variations and changes in the laser reflected power. The charging level is controlled by varying the On-state duration of an IGBT. A photograph of the SSLAM charge module appears in Fig. 7.1. While a simplified schematic is presented in Fig. 7.2.

On a scale of peak-power-handling, IGBTs fit in the region between MOSFETs and SCRs. MOSFETs and IGBTs can operate as opening switches and SCRs cannot. An SCR can only be brought out of conduction by reducing the conducted current to near zero. IGBTs (MOSFETs) can be brought out of conduction even at the full current rating by simply reducing the voltage to zero on the Gate-Emitter (Gate-Source) connections.

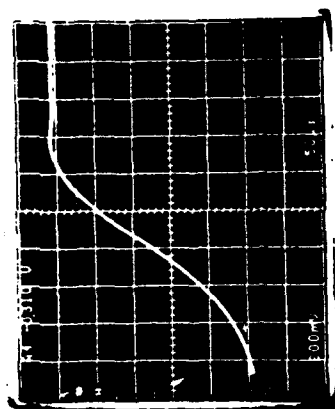
IGBTs differ from MOSFETs in that MOSFETs are a majority carrier device and IGBTs are minority carrier device like all bipolar transistors. Majority carrier devices offer low drive requirements and high switching speeds but high conduction losses and a dangerous positive temperature coefficient of the on-state resistance. That is, as the junction temperature of a majority carrier device rise so does the on-state resistance and therefore the voltage drop increases at a given current as the temperature rises. The hotter the device becomes the more power is dissipated and therefore the hotter it becomes.

IGBTs, like conventional bipolar transistors, are a minority carrier device and exhibit a negative temperature coefficient of on-state resistance. As the junction temperature rises the on-state resistance decreases and therefore the voltage drop decreases at a given current with increasing temperature. The hotter the device becomes the less power is dissipated. Historically, the disadvantage of bipolar transistors has been the enormous drive requirements. IGBTs eliminate the large drive requirement by incorporating a MOSFET driver on the same chip with the bipolar transistor. This MOSFET supplies the drive to the bipolar transistor and we wind up with a device which provides the best of both worlds. The input drive requirements and turn-on characteristics match the superior performance of a MOSFET while the power handling capability models that of a bipolar transistor. Because of this IGBTs are rapidly replacing MOSFET in inverter power supply and many other applications.

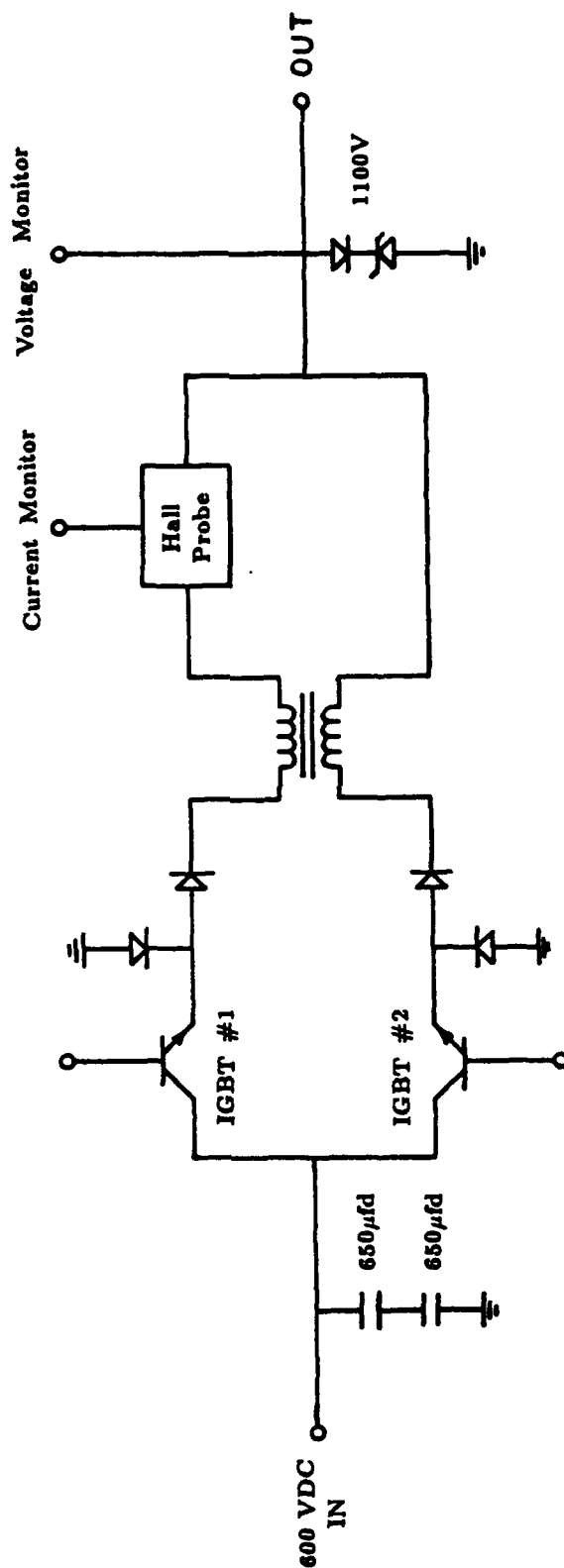
When the IGBT is brought out of conduction the charging cycle can not be immediately terminated. There is energy stored in the charging inductor and that energy must go somewhere. The incorporation of a free wheeling diode to ground allows the energy stored in the charge inductor to be transferred into the intermediate storage capacitor after the IGBT conduction cycle is terminated. The final charge voltage will not be simply determined by the intermediate storage



Figure 7.1: SSLAM Charge Module



Typical Charging Waveform
200 V/d, 50 μ secs/d



Single Bucket, IGBT Based Inverter with PWM

Figure 7.2: SSLAM Charge Module

capacitor voltage level when the IGBT is brought out of conduction but will also hinge on the current level flowing in the charge inductor at that time.

The SSLAM control module must base its decision on two input variables. It must measure the current flowing in the inductor and the voltage appearing on the intermediate storage capacitor. It is simple to show energy conservation the

$$1/2CV_f^2 = 1/2CV_i^2 + 1/2LI^2$$

and the current can easily be determined by applying the rule that

$$I = CdV/dt$$

More recently a Hall probe has been added to the charge module to provide a more accurate indication of the charging current.

The Control Module

The SSLAM control module contains a small analog computer which precisely measures the voltage and its derivative and then makes the determination of the final charge voltage based on the following equation.

$$V_f = \sqrt{V_i^2 + LI^2}$$

The SSLAM control module also compares power supply levels and intermediate storage charging levels to predetermined limits and discontinues the driver operation if these levels fall out of these limits. It also bears responsibility of triggering the SCRs in the SSLAM compression module at the appropriate time.

A simplified schematic of the control circuitry found in the SSLAM control module can be found in Fig. 7.3 while a photograph of the assembled unit appears in Fig. 7.4.

The Control Module contains all of the digital and analog circuitry required to control the operation of the SSLAM laser driver system. It accepts a TTL level input signal from a customer supplied pulse generator as an indication to generate an output pulse. The power level of this output pulse can be adjusted through either the 10 turn potentiometer on the front panel or by supplying an external reference (0-5 volts). The Control Module takes the responsibility of controlling both the charging and discharging the Intermediate Storage capacitors. It controls the IGBT based Charge Module during the charging phase and supplies the SCR triggers which discharge the Intermediate Storage capacitors into the nonlinear magnetic compression chain. During both of these operations it monitors voltage and current levels throughout the system and assures that all components are operating within acceptable limits.

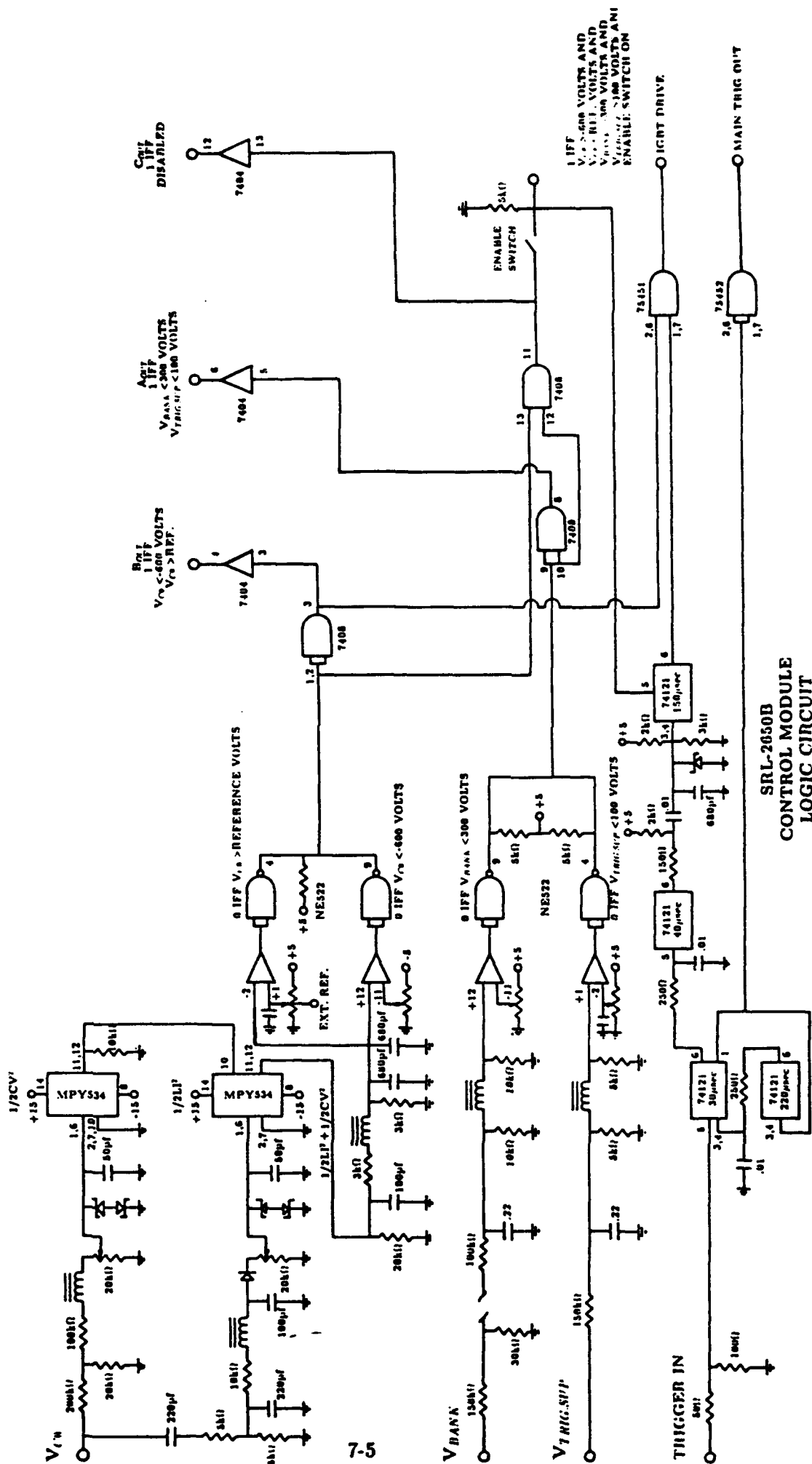


Figure 7.3

Figure 7.4: SSLAM Control Module

